THE DEVELOPMENT AND APPLICATION OF CREEP DAMAGE CONSTITUTIVE EQUATIONS FOR HIGH Cr STEEL OVER A WIDE RANGE OF STRESS

XUMING ZHENG

A thesis submitted to the University of Huddersfield in partial fulfilment of the requirements for the degree of Doctor of Philosophy

School of Computing and Engineering
The University of Huddersfield

April 2021

Copyright Statement

i. The author of this thesis (including any appendices and/or schedules to this thesis) owns any copyright in it (the "Copyright") and s/he has given The University of Huddersfield the right to use such copyright for any administrative, promotional, educational and/or teaching purposes.

ii. Copies of this thesis, either in full or in extracts, may be made only in accordance with the regulations of the University Library. Details of these regulations may be obtained from the Librarian. This page must form part of any such copies made.

iii. The ownership of any patents, designs, trademarks and any and all other intellectual property rights except for the Copyright (the "Intellectual Property Rights") and any reproductions of copyright works, for example graphs and tables ("Reproductions"), which may be described in this thesis, may not be owned by the author and may be owned by third parties. Such Intellectual Property Rights and Reproductions cannot and must not be made available for use without the prior written permission of the owner(s) of the relevant Intellectual Property Rights and/or Reproductions.

Abstract

The increasing thermal efficiency while at the same time keeping safe production are two vital targets that are required to be achieved to high productivity from power plants. The development and application of high creep resistant chromium (Cr) steel is becoming increasingly critical over a wide range of stress at high temperatures for power plant components. Knowledge of creep behaviour processes such as creep strain, creep damage, and rupture time can aid in the design and development of components. During the past three decades, a series of creep damage constitutive equations have been developed and applied to describe the creep behaviour for high Cr steel. The Continuum Damage Mechanics (CDM) model describing tertiary creep damages such as cavitation damage mechanism that is a dominant factor in the process of creep fracture. However, they are phenomenologically based. In addition, the most developed equations have only focused on middle-high stress levels; they were not developed for the low stress level and found invalid when compared with experimental data.

This thesis describes the development of new creep damage constitutive equations for high Cr steel over a wide range of stress conditions. It also reports its additional application to 316H stainless steel. This broadening of application means that the novel equation is suitable for more stress levels than traditional equations, especially under low stress situations.

The research undertaken can be summarised in the following four aspects. Firstly, the previously developed "novel hyperbolic sine law" is applied over a wide range of stress for P91 and P92 steels. Its adaptability has been shown to be better than traditional methods by experimental data under the widest range of stress. Secondly, a novel creep cavitation damage equation is successfully applied and calculated for E911 steel at rupture time which can build a good foundation to apply the equation at different stages of creep lifetime and therefore achieve the predicted lifetime for components. Thirdly, the creep cavitation rupture modelling is developed and applied at 600°C and 650°C for P92 steel. This includes developing and confirming the "novel hyperbolic sine law" to discuss the relationship between the creep rupture time coefficient U' and a wide range of stress, and as a result, accurately predict lifetime for components. Finally, a creep cavitation model for different stages of creep lifetime is developed at 550°C and 675°C for 316H steel. This achieves a further application of the novel creep cavitation equation and confirms that the creep cavitation damage equation is not only applied at creep rupture time but is also suitable for a creep at any time period. This thesis contributes to the creep damage modelling methodology and specific knowledge.

Acknowledgements

I am thankful to my supervisor Dr Qiang Xu and co-supervisor Professor Zhongyu Lu for their interest, support and encouragement that enabled me to undertake this study. Their professional knowledge in creep damage mechanics and creep cavity fracture models gave me useful guidance and continuous encouragement throughout the entire lifespan of my PhD project.

I especially want to thank my supervisor, Dr Qiang Xu, for guiding and teaching me to treat and solve problems with a strict academic attitude and a spirit of never giving up and providing some opportunities to attend interesting international conferences and meetings during my research.

I thank my external adviser Professor Xue Wang who hosted me for my Santander PGR study visits and for his contributions in reviewing draft scientific paper publications.

I also wish to thank my parents and my husband for their encouragement and financial support; without their support and help, I could not have completed my PhD project.

Finally, I am must grateful and appreciative for the award of the Santander Student Mobility Scholarship from Santander in order for the study to be undertaken.

Declaration

The thesis is submitted to the degree of Doctor of Philosophy at the University of Huddersfield. I announce that the work in the paper was carried out by the Regulations of the University of Huddersfield.

The whole research was carried at the University of Huddersfield under the supervision of Dr Qiang Xu and co-supervisors Professor Zhongyu Lu.

The work is original, unless where the previous work is confirmed and referenced. The thesis or any similar paper has not been submitted to the degree, diploma, or other qualification certification at any other university.

List of Publications

Zheng, X.M., Xu, Q., Lu, Z.Y., Wang, X., and Feng, X.Q. (2020) The development of creep damage constitutive equations for high Cr steel. *Materials at High Temperatures*, 37(2), 129-138.

Xu, Q., **Zheng, X.M.,** Okpa, M., Lu, Z.Y., and Vishnyakov, V. (2018). Poster. The development of creep damage constitution equations for high Cr alloys. International Conference on Power Plant Operation & Flexibility, The Institute of Materials, Minerals and Mining (IOM3), July 4–6, 2018, London.

Contribution Statement for above publications:

(1) Xuming Zheng individually carried out the research, producing all the results, drafted the paper, and improved the calculated method for four material parameters in the cavitation damage equation. The final stage of reviewing and publishing the paper was finished together with Dr Qiang Xu.

(2) The poster was based on the results of the research group. Xuming Zheng drafted the poster and reported her results from number one to number three within the results section. Her work is combined with new products and has been published in the (1) paper listed above.

Contents

List of Tables

List of Figures

List of Abbreviations

2D	Two Dimensional
3D	Three Dimensional
CDM	Continuum Damage Mechanics
CTZ	Completely Transformed Zone
EBSD	Electron Backscatter Diffraction
ECCC	European Creep Collaborative Committee
EPRI	Electric Power Research Institute
ETD	European Technology Development Ltd
ESRF	European Synchrotron Radiation Facility
FE	Finite Element
HAZ	Heat Affected Zone
IQ	Image Quality
IPF	Inverse Pole Figure
KRH	Kachanov-Rabotnov-Hayhurst
MARBN	Martensitic Boron–Nitrogen strengthened steel
NIMS	The Japanese National Institute for Materials Science
OPM	Optical Microscopy
OTZ	Over Tempered Zone
PTZ	Partially Transformed Zone
SANS	Small-Angle Neutron Scattering
SEM	Scanning Electron Microscopy
Spring-8	Japan Synchrotron Radiation Research Institute
SZMF	Salzgitter Mannesmann Forschung GmbH
TEM	Transmission Electron Microscopy
UKERC	UK Energy Research Centre
UKNNL	UK National Nuclear Laboratory
UKNPL	UK National Physical Laboratory

List of Nomenclature

A, B, A_1, B_1, A', B'	Material parameters, possibly dependent on temperature
A_1, A_2, α, β, γ	Material parameter may depend on stress
C	Integration constant related to the cavity growth rate
C_1, C_2	Material parameter
$\dot{\varepsilon}$	Creep strain rate
$\dot{\varepsilon}_{min}$	Minimum creep strain rate
$f(R)$	The probability density function of cavity equivalent
σ	Stress
$N(R, t)$	The cavity size distribution function
n	Stress exponent
q	Stress exponent
$\dot{R}$	The growth rate of the cavity radius
R	Cavity radius
t	Time
t_r	Creep rupture time
J	The number density of cavity
J^*	Cavity nucleation rate
U'	Material parameter may depend on stress
w	The cavity area fraction along the grain boundary
w_f	A critical value of the cavity area fraction at the fracture

List of Equations

Minimum creep strain rate:

Power law $\dot{\varepsilon}_{min} = A\sigma^n$…….. Section 5.2.1, Section 5.4

Linear power law $\dot{\varepsilon}_{min} = A\sigma[1 + (B\sigma)^n]$…..... Section 5.2.2, Section 5.4

Hyperbolic sine law $\dot{\varepsilon}_{min} = Asinh(B\sigma)$……. Section 5.2.3, Section 5.4

Novel hyperbolic sine law $\dot{\varepsilon}_{min} = A\sin\mathrm{h}(B\sigma^q)$…… Section 5.3, Section 5.4

Cavitation damage functions:

Cavity size distribution

$N(R,t) = \frac{A_2}{A_1} R^{\beta} t^{\alpha+\gamma} \left(1 - \frac{1-\alpha}{1+\beta} \frac{R^{\beta+1}}{A_1 t^{1-\alpha}}\right)^{(\alpha+\gamma)/(1-\alpha)}$ Section 6.3, Section 8.2, Section 8.3

$N(R,t_f) = \frac{A_2}{A_1} R^{\beta} {t_f}^{1+\gamma} exp\left(-\frac{1+\gamma}{1+\beta} \frac{R^{\beta+1}}{A_1}\right)$…… Section 6.3

$f(R) = C_1 R^{\beta} exp\left(-\frac{C_2 R^{\beta+1}}{1+\beta}\right)$…… Section 6.3

Cavity growth rate $\dot{R} = A_1 R^{-\beta} t^{-\alpha}$. Section 6.3, Section 8.4.3, Section 8.4.4

Cavity growth $\frac{1}{3} R^3 = A_1 lnt + C$……... Section 6.3, Section 8.4.3

Cavity area fraction $w = \int \pi R^2 N(R,t) dR$

$w_f = U' \times t_f^2$ ……..…….... Section 6.4, Section 8.4.1

Cavity nucleation rate $J^* = A_2 t^{\gamma}$…….…… Section 6.5

Cavity nucleation $J = \frac{1}{2} A_2 t^2$…….……...……. Section 6.5, Section 8.4.2

Creep rupture time:

Conventional $t_r = A\sigma^{-n}$……... Section 7.3

Novel hyperbolic sine law $U' = A_1 sinh(B_1 \sigma^q)$…….……..... Section 7.2

$t_f = (W_f/(A_1 sinh(B_1 \sigma^q))^{(\frac{1}{2})}$……..... Section 7.3

Monkman-Grant (M-G) $\dot{\varepsilon}_{min} = (\frac{C_{MGR}}{t_f})^{1/m}$ ……... Section 7.4

Chapter 1 Introduction

1.1 Project background

1.1.1 Increasing electricity generation, production and thermal efficiency and decreasing CO_2 emissions

According to the global energy statistics report (Global Energy Statistical, updated 2020), global power generation production has greatly increased between 1990 and 2019 (Figure 1.1). Electricity generation was produced from mixed fuel sources between 1971 and 2018 as indicated in Figure 1.2. Power generation from fossil fuels such as coal, natural gas, and oil is still dominant by far across the world; especially for coal which was responsible for 38% of the global electricity production in 2018 (World Energy Balances, updated 2020).

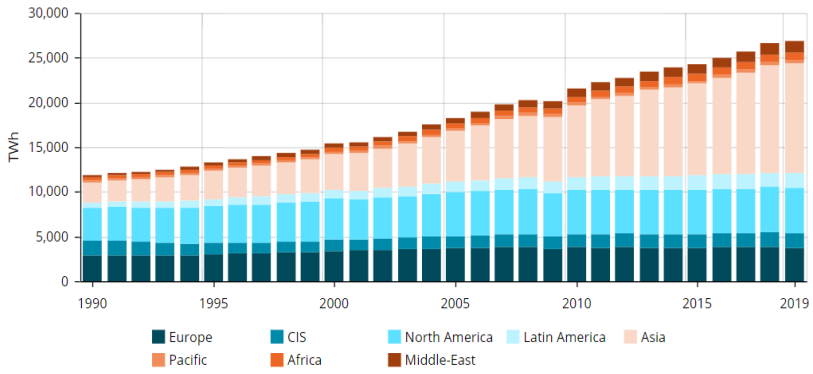

Figure 1.1 The global electricity production from 1990-2019 (Global Energy Statistical by Enerdata, updated 2020).

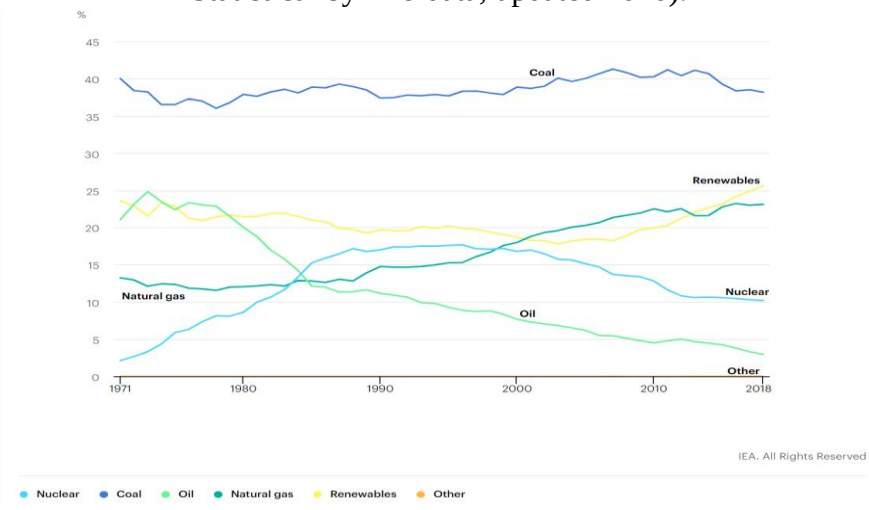

Figure 1.2 World electricity generation mix by fuel from 1971-2018 (World Energy Balances overview by IEA, updated 2020).

Globally people are now paying more attention to achieving environmental protection. Thus, this requires low emissions from fossil fuels and increased efficiency in consumption in power plants during the combustion process. The reduction of carbon dioxide (CO_2) is the primary target in achieving low emissions from fossil fuel burning power plants; an urgent task for the power industries. This includes capture, compression, transport, and storage of CO_2 in the oil and deep saline aquifers (Vangkilde et al., 2009; Panait, 2010a). The method can be achieved and so has almost reached zero emission in some power plants (Rubin et al., 2007). An alternative way, which is more efficient consumption of fuels, requires increasing the steam condition to higher ranges of temperature and stress (Panait, 2010a). This operation needs to choose heat resistant steels and materials with higher creep strength. The amount of CO_2 emission can be also decreased by increasing the operating temperatures of the power plants. Thus, the development of a new heat resistant steel is essential to increase efficiency in power plants. However, this is not the thrust of the current study; here, the current author is only seeking to model creep over a wide range of stress within existing materials.

1.1.2 The development of high Cr steel in a power plant

According to Maruyama et al. (2001), thermal fatigue of the components is a serious problem in a fossil power plant. Ferritic heat resistant steel is currently employed widely in the fossil power station due to the following characteristics; high thermal conductivity, low thermal expansion coefficient and less susceptibility to thermal fatigue. However, it is limited in that the low creep strength of this heat resistant steel is linked to the operating temperature of the power station. Increasing operating temperatures and stresses can impose increasingly tight requirements for materials. Thus, the development of advanced ferritic heat resistant steels is an urgent requirement. People started from Cr-Mo steel and added V, Nb and N into the steel to increase its creep strength and increase the Cr content to have better oxidation resistance, which all requires the power plants to operate at higher temperatures. Development of several advanced ferritic heat resistant steels such as P91/T91 (9Cr–1Mo–VNb) steel, P92/T92 (9Cr–1.8W–0.5Mo–VNb) steel and P122/T122 (11Cr–2W–0.5Mo–CuVNb) steel (Maruyama et al., 2013b) are shown in Figure 1.3.

In regards to recent advances in creep resistant steel for power plant applications, Ennis et al. (2003) summarised how to develop the advanced ferritic heat resistant steel from P9 to P92 steel as is indicated in Figure 1.4. This is based on the 1×10^5h at the temperatures of 600℃ and 650℃.

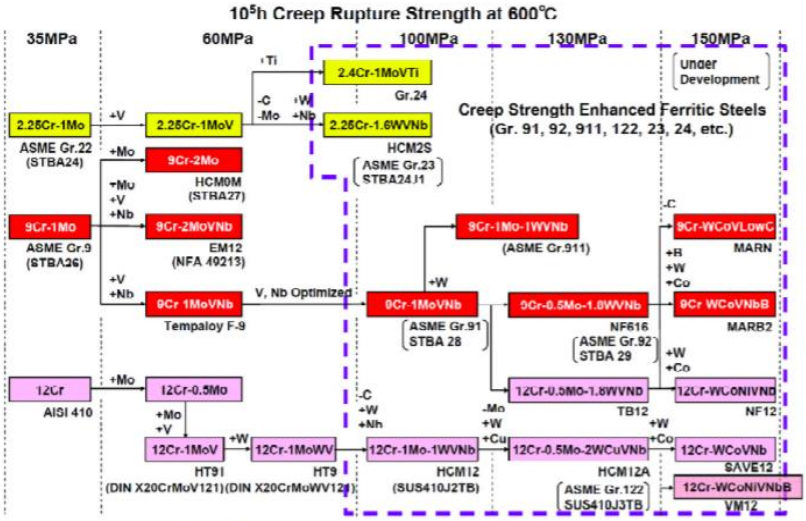

Fig.1. Development progress of boiler steels and CSEF steels.

Figure 1.3 The development of progress for heat resistant steels (Masuyama et al., 2013b).

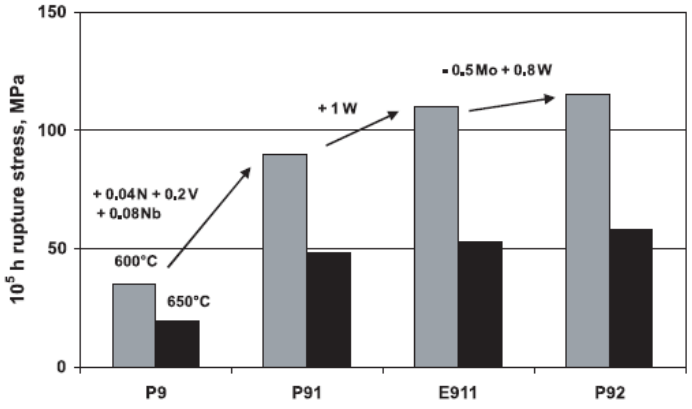

Figure 1.4 The development of 9% high Cr steels (Ennis et al., 2003).

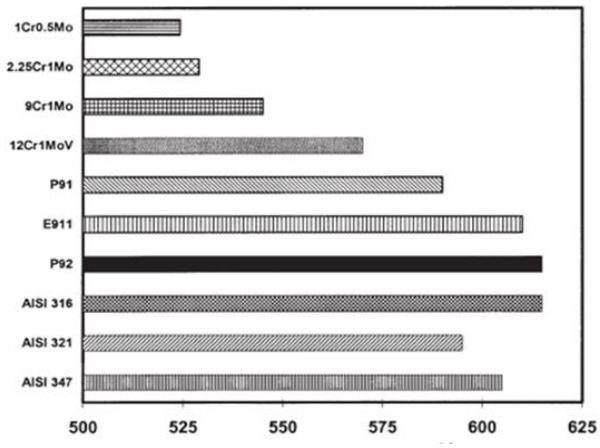

Figure 1.5 Stress rupture strengths applied in power station steels (Ennis et al., 2003).

Ennis et al. (2003) also summarised the maximum operating temperature of different heat resistant steels recently used in the development of new power plant steels, which is based on a 1×10^5h average stress rupture strength of 100MPa. The detailed information is shown in Figure 1.5. The most advanced high Cr steel is used in the modern steam power plant with steam temperatures of 600℃ and stress of 25-30MPa, and the super steam power plants which will have operating temperatures up to 650℃ in the future (Ennis et al., 2003).

1.1.3 The significance of creep cavitation damage in engineering material

In general, creep cavitation damage acts as the critical factor in creep rupture. The creep fracture is related to the cavity nucleation and cavity growth occurring at the grain boundary; their growth and linking with an adjacent cavity form cracks which lead to final rupture. The mechanism of cavity nucleation and cavity growth is independent during the operation, specifically for cavity growth. However, the coalescence of cavities starts sooner or later to happen (Sklenicka et al., 2003). Figure 1.6 outlines that the cavity nucleation and growth are approximately 0.8 times of the creep lifetime. Thus, researching the creep cavitation damage is essential, specifically predicting the creep lifetime of components in the power station.

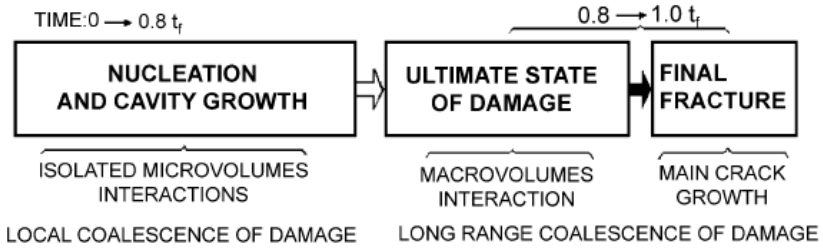

Figure 1.6 The development of the intergranular cavities (Sklenicka et al., 2003).

During recent decades, researchers (Lee et al., 2006; Parker, 2013; Aghajani et al., 2009; Sklenicka et al., 2010; Shinya et al., 2006) have used traditional techniques to observe cavitation damage for the high and low Cr steels, for example, Transmission Electron Microscopy (TEM), Optical Microscopy (OPM) and Scanning Electron Microscopy (SEM). Observing the creep cavities has determined that they mostly occur at the grain boundary, and its characteristic is perpendicular to the direction of stress. However, the resolution and continuity for the cavitation process cannot be caught; hence the creep cavitation is restricted. Some researchers have focused on the investigation of the evolution of creep deformation occurring in the grain, which includes hardening, solute depletion, coarsening, diffusion, and dislocation (Ennis et al., 1997; Hayhurst et al., 2008; Yin et al., 2006). Currently, no research has paid attention to investigating the evolution of the process for the cavitation and its characteristic. Presently, using the

advanced technology of synchrotron X-ray microtomography such as European Synchrotron Radiation Facility (ESRF) (Sket et al., 2010; Renversade et al., 2014) and Japan Synchrotron Radiation Research Institute (JSRRI) (Gupta et al., 2013; Gupta et al., 2015; Schlacher et al., 2012; Schlacher et al., 2015) researchers can catch the high resolution and continuity of the process for the cavitation. And the 3D visualisation can observe the process of increasing creep cavity with time. This experimental data can provide a better survey and foundation to investigate the characteristic of the cavity nucleation and cavity growth, and then lead to the exact development of creep cavitation equations for predicting the creep lifetime of components in the power plant.

1.1.4 The existing developed creep damage constitutive equations

Creep deformation and damage are important factors when investigating the evolution of damage and predicting the lifetime for components in the power station at high stress and temperature. The experimental creep data is limited due to the long time and high cost in acquiring this data. Thus, using the conventional empirical method cannot correctly predict the lifetime of components. Some research institutes have based their work on experimental techniques or creep damage constitutive equations to investigate the creep damage behaviour in the structural components, for example, European Technology Development Ltd (ETD), European Creep Collaborative Committee (ECCC), Electric Power Research Institute (EPRI), UK Energy Research Centre (UKERC), UK National Physical Laboratory (UKNPL), UK National Nuclear Laboratory (UKNNL) UK University of Manchester, UK Imperial College London, UK The Open University, and The Japanese National Institute for Material Science (NIMS). However, there still existed deficiencies and limitations for the equations, which can be listed as follows:

(1) Some developed creep damage constitutive equations are only based on the experimental data under high stress. These equations are challenging for direct application in a wide range of stress. This method is not satisfactory because the creep damage mechanism has changed under different stress levels (Abe et al., 2008; Evans et al., 1984; Xu, 2016).

(2) The standard equation of the minimum creep strain rate cannot fit very well with its experimental data in a wide range of stress for high Cr steel, such as power law, linear power law and hyperbolic sine law (Xu et al., 2017a; Yang, 2018; Zheng et al., 2020).

(3) The most developed equations were just based on the creep deformation occurring at the grain and were considered the effects of cavitation damage arising at the grain boundary in the process of creep fracture (Xu et al., 2019).

(4) The development of a creep damage constitutive equation for low Cr steel was compiled by Xu (2016). She successfully applied the minimum strain rate

equation under a wide range of stress for low Cr steel. However, the creep cavitation damage adopted the typical equation that was proposed at high stress levels because of the lack of experimental data under low stress levels for low Cr steel (Xu, 2016; Yang, 2018).

(5) Another creep damage constitutive equation for P91 steel was developed by Yang (2018). He successfully modified and applied the minimum strain rate equation under a wide range of stress for P91 steel and developed and applied a novel creep cavitation damage equation for P91 steel. However, compared with the current author, the most significant difference is between using the material and developmental approach.

1.2 Aim and objectives of the study

This research project aimed to develop and apply novel creep damage constitutive equations for high Cr steel over a wide range of stress. The wide stress range signifies that the novel equation is suitable for more stress levels than that in traditional equations, especially under low stresses. These constitutive equations are based on the mechanisms of creep cavitation damage and suitable for the calibration of the creep cavitation model at a different stage at rupture time. To achieve this aim, the following objectives were compiled:

(1) To review the existing creep damage constitutive equations for high Cr steel and analyse their advantages and disadvantages. The detailed information is outlined in section 2.6 of Chapter 2.

(2) To collect and analyse the existing and published experimental data for high Cr steel. The detailed information is outlined in Chapter 4.

(3) To apply and calculate the minimum creep strain rate over a wide range of stress for P92 steel based on the "novel hyperbolic sine law" and the published data. The methodology is detailed in section 3.2.1 of Chapter 3, and the results are displayed in Chapter 5.

(4) To apply and calculate a novel creep cavitation damage equation for high Cr steels based on cavity nucleation and cavity growth model, based on the published observation data. The methodology is detailed in section 3.2.2 of Chapter 3, and the results are displayed in Chapter 6.

(5) To develop and apply a creep cavitation rupture modelling for P92 steel based on the relationship between coefficient U', stress, minimum strain rate, and rupture time. The methodology is detailed in section 3.2.3 of Chapter 3, and the results are displayed in Chapter 7.

(6) To develop and calibrate a creep cavitation model at different stages of creep lifetime for a 316H steel is based on the cavity nucleation and growth model, and their experimental data is based on the published observation data. The methodology is detailed in section 3.2.4 of Chapter 3, and the results are displayed in Chapter 8.

(7) To validate the novel creep damage constitutive equations by comparing the modelling results with their experimental data and the classical modelling results for high Cr steel. The results are shown in sections 5.3-5.4 of Chapter 5, section 6.3 of Chapter 6, sections 7.2-7.5 of Chapter 7, and sections 8.2-8.3 of Chapter 8.

1.3 Structure of the thesis

This thesis consists of nine chapters:

Chapter 1 introduces the background information in the research area, including describing the criticalness of cavitation damage and the importance of developing constitutive equations within the industry, and lists the aim and objectives of the research project. It also outlines the structure of the whole thesis.

Chapter 2 introduces the creep deformation and creep cavitation damage mechanisms, and the stress breakdown phenomenon. This chapter reviews the advantages and disadvantages of the existing predicting model, and presents the existing novel creep damage constitutive equation and reviews the current state of experimental data.

Chapter 3 introduces the research methodology for the development and application of creep damage constitutive equations in the project.

Chapter 4 collects and analyses the experimental data for high Cr steel, which includes the NIMS creep data sheet and the observation of experimental data. It also details which of the following chapters utilise the experimental data.

Chapter 5 presents the applied and calculated novel minimum creep strain rate for high Cr steel over a wide range of stress. It also introduces the deficiencies of the classical constitutive equations through comparing its modelling results.

Chapter 6 introduces the application and calculation of the creep cavitation damage equation for high Cr steel. Including the theory of cavity area fraction along the grain boundary, the calibration of cavity growth rate and nucleation rate models according to the determination of model constant. It also displays the relationship between the cavity nucleation coefficient and stress under different temperatures.

Chapter 7 presents the development and application of creep cavitation rupture

modelling for P92 steel and accordingly discusses the relationship between coefficient *U'*, stress, rupture time and minimum creep strain rate and determines the material constants and describes the characteristics of the developed derived equation.

Chapter 8 develops and calibrates a creep cavitation model at different stages of creep lifetime for 316H steel based on the two sets of creep testing experimental data under different temperature and stress. It also describes the characteristics of creep cavitation damage, including the process of *W*, *J*, *R* and *R* rate with time.

Chapter 9 concludes and lists the main significant contributions of this project and outlines potential further work to be undertaken.

Chapter 2 Literature review

2.1 Introduction

This chapter reviews and analyses the related literature in the area of development and application of creep damage constitutive equations for high Cr steel. The first step is to discuss the creep deformation mechanisms and creep rupture to summarise the advantages and disadvantages of the existing predicting models. Then by gaining an understanding of the cavitation damage, which is essential and dominant in the creep behaviour, gives the existing novel equations and the current state of experimental data for developed creep damage constitution equations in the end. The following lists the main outline of this chapter:

(1) Understanding the general creep mechanisms, such as diffusion and dislocation.

(2) According to the shapes of creep curves, understanding the creep behaviour for high Cr steel under different conditions, and its influence factors.

(3) Based on the several different functions to introduce the relationship between the minimum creep strain rate and applied stress in creep damage constitutive equation, including the “novel hyperbolic sine law”.

(4) According to the study on the relationship between rupture time and stress, understanding the stress breakdown phenomena for high Cr steel.

(5) According to the information by traditional 2D technology observing the fracture surfaces for high Cr steel, understanding the creep fracture mechanism.

(6) Based on the types and equation of cavity nucleation and growth, understanding the creep cavitation damage for high Cr steel.

(7) Understanding the importance and dominated cavitation damage mechanisms in creep damage.

(8) Reviewing the existing creep damage constitutive equations and analysing their advantages and disadvantages.

(9) Summarise the current state of experimental data for developing creep damage constitution equations.

2.2 Creep mechanisms in steels

Creep of materials is associated with time-dependent, non-reversible deformation, when steel is under stresses. Stresses can be lower than that within its yield stress over

a long time. This can occur at any temperature above absolute zero (-273.15°C). However, what can happen at high temperatures is much more important from a practical view (Evans and Wilshire, 1985; Nikbin, 2009; Saber, 2011; Kassner, 2015). Creep is a multiplex process in steel, which involves a few mechanisms, including diffusional flow, dislocation slip and climb. Not only the mechanism or behaviour may independently operate with each other, but also more than one mechanism can occur at the same time in the creep condition.

2.2.1 Diffusion

Diffusion is a process of atom movement between places in the steel and occurs through the grain and along the grain boundary. This process is dominant at low stress and high temperature. Three types, including vacancy diffusion, interstitial diffusion and diffusion at the grain boundary, are shown in Figure 2.1. The first type often occurs when the atom moves from its position to a space that may be the same size as the atom itself. The second type happens when the small atom moves into space between two or more large atoms. The last type occurs at the grain boundary, which is quicker compared with that in the grain.

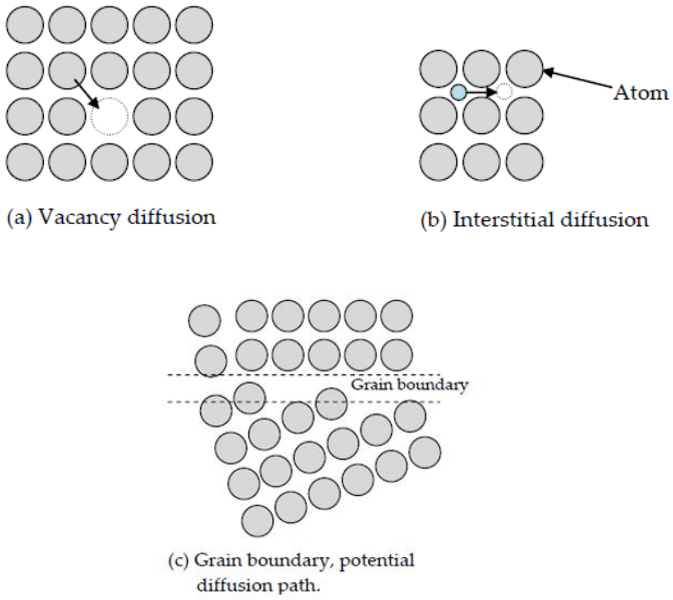

Figure 2.1 General diffusion (Saber, 2011).

2.2.2 Dislocation

The dislocation is dominant in the creep mechanism at high stress and low temperature, which is also called power law creep. Dislocation can move through gliding in a slide plane or climbing with the assistance of diffusion. The detailed move type is given below in Figure 2.2.

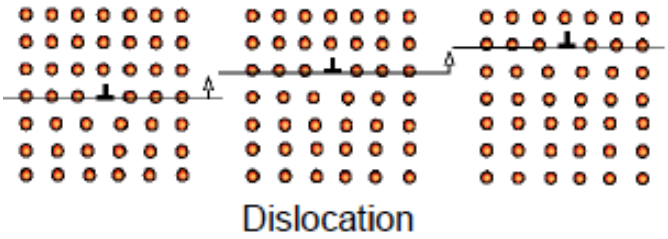

Figure 2.2 General dislocation (Alang, 2018).

2.3 Creep deformation in steel

The different zones of creep may be conveniently represented on a deformation mechanism map (Figure 2.3). G is the shear modulus for the material, and T_M is the absolute melting temperature (Cole, 2000). Each zone indicates a main physical mechanism for controlling flow, although it will be more than one mechanism near the edge of each area. The creep deformation is divided into two major creep zones: dislocation creep and diffusion creep. At a high temperature and stress range, the dislocation creep (including bulk diffusion and core diffusion) dominates the creep deformation mechanism. At a low temperature and stress range, the diffusion creep (including bulk diffusion and boundary diffusion) controls the creep deformation mechanism.

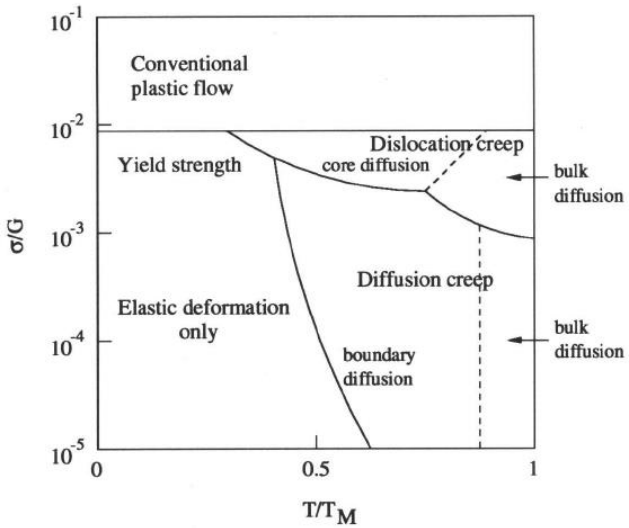

Figure 2.3 Creep deformation map (Cole, 2000).

2.3.1 Creep curve

Generally, using a creep curve reflects the creep behaviour during creep testing. The creep curve describes the relationship between the creep strain and over time under

constant temperature and stress. The creep curve mainly includes three distinct regions: primary stage, secondary stage, and tertiary stage (Figure 2.4). The primary stage is to make up elastic and plastic of initial strain, and the creep strain rate decreases with time until its creep strain rate becomes a constant. During this stage, the process of hardening work dominates and causes dislocation movements to be limited. In the secondary location, the creep strain rate keeps a constant value with time before that the rate begins to increase. This process is also called the steady state stage, which usually accounts for the longest time of the creep process. Thus, the creep rate in the steady state is significant for creep behaviour. During this stage, the specimen can be observed as isolated cavities and oriented cavities; the operations exist of observation and fixed inspection intervals. In the final stage, the quickly increasing creep strain rate leads to the component occurring rupture and failure. In this case, the specimen can occur microcracks, macrocracks and fractures, at which service is limited and needs to be immediately repaired in point D (Figure 2.4). The creep curve and corresponding service operations at a constant temperature and stress is displayed in Figure 2.4.

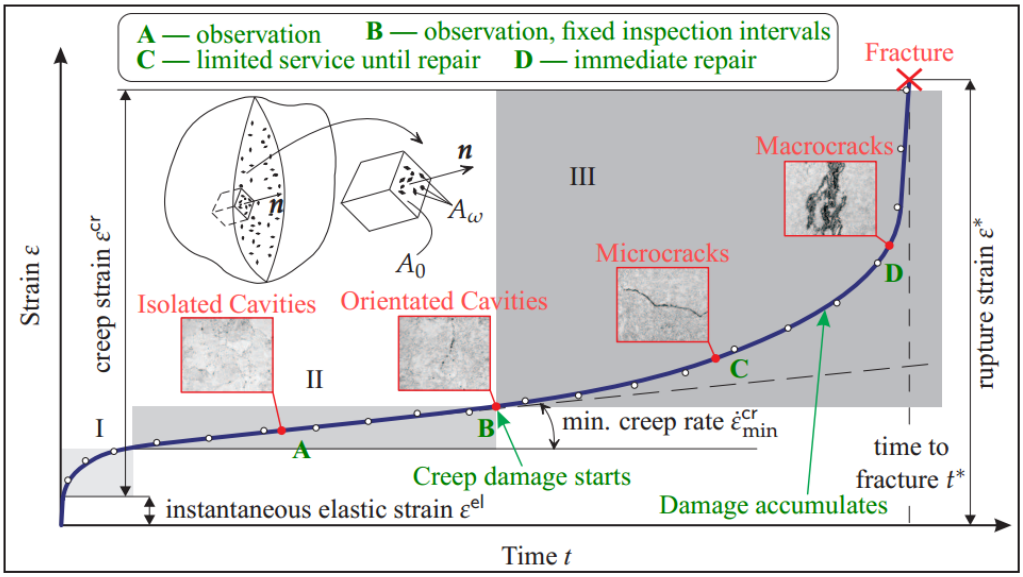

Figure 2.4 A typical creep curve and corresponding service operations at a constant temperature and stress (Gorash, 2008).

According to Saber (2011) and shown in Figure 2.5: a) the three creep regions existed at the same time for cracked bodies. Only a small area of the uncracked ligament, which is nearing the crack tip, goes through obvious creep deformation in the small scale creep; b) the creep zone occurs in transition creep. Creep deformation dominates in the elastic and plastic areas but cannot be called to dominate the whole uncracked ligament; c) the creep zone happens in extensive creep when the whole uncracked ligament experiences creep deformation. Compared with the crack size and uncracked ligament size, the size of the area controlled by creep deformation is significant.

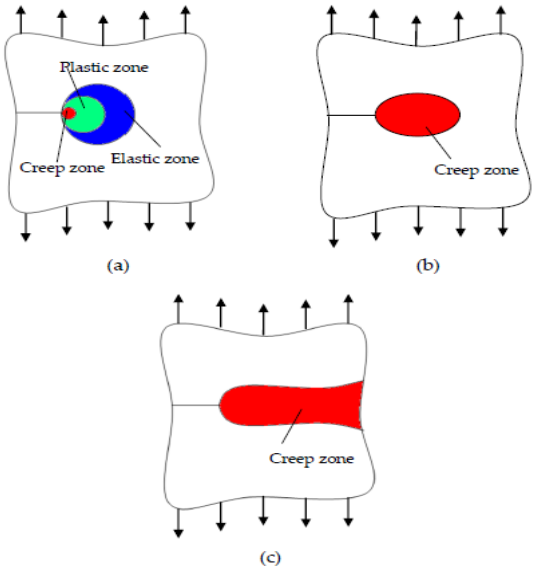

Figure 2.5 The creep deformation in an element: a) small scale creep; b) transition creep; c) extensive creep (Saber, 2011; Landes et al., 2004).

2.3.2 Influence factors

Temperature and stress act as two critical factors in creep strain and affects creep behaviour, which is shown in Figure 2.6. Creep strain increases with temperature increasing under constant stress, and creep strain increases with pressure increasing at a constant temperature. However, the creep rupture time and steady state stage both decrease with temperature and stress increasing.

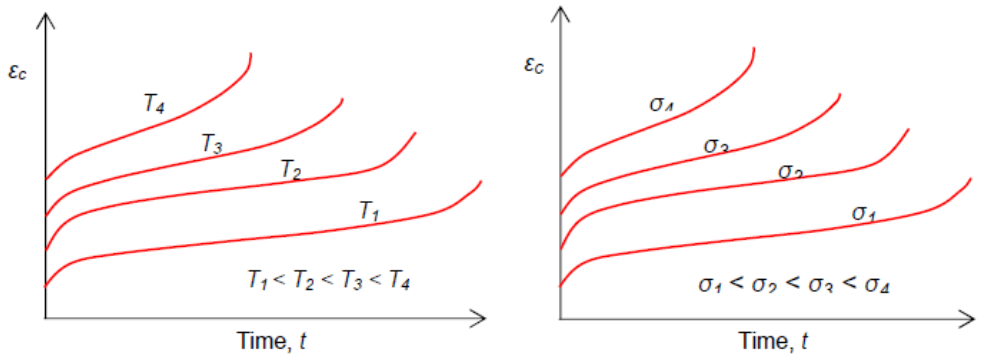

Figure 2.6 The effect of temperature and stress in creep strain (Alang, 2018).

Work by Sakthivel et al. (2015) showed that the primary creep areas of creep strain to be at 600°C, 650°C and 700°C for P92 steel (Figure 2.7). In this stage, the initial creep strain decreases with the temperature increasing; creep strain increases more quickly at this period. However, under a lower range of stress at 700°C, the apparent primary creep region cannot be observed (Sakthivel et al., 2015).

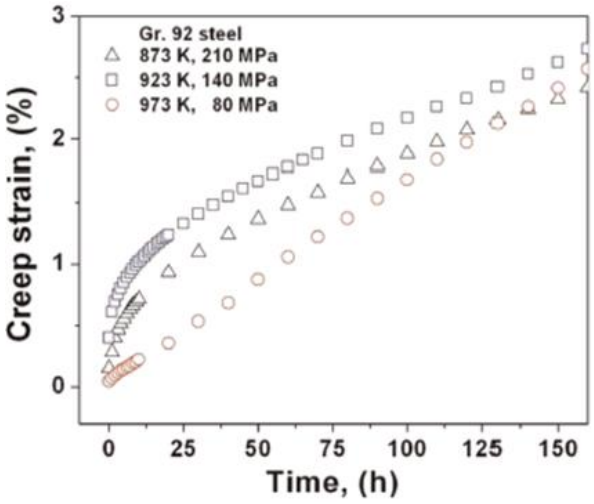

Figure 2.7 Primary creep region at three different temperatures for P92 steel (Sakthivel et al., 2015).

The curves of creep strain with time under different stress from 110MPa to 170MPa at a constant temperature for P92 steel is displayed in Figure 2.8. The rupture time decreases with the stress increasing. The creep strain exhibits instant strain on loading, different primary creep, narrow secondary creep zone and dragging final creep region. Under lower stress levels at 600°C, more extended secondary creep areas can be observed in the material, which may be due to increasing solution strengthening in the solid (Sakthivel et al., 2015). Thus, discussing the minimum creep strain rate and rupture time under a wide range of stress is necessary for the development of creep damage constitutive equations. The relationship between the minimum creep strain rate and stress is located in the secondary creep region of the creep curve.

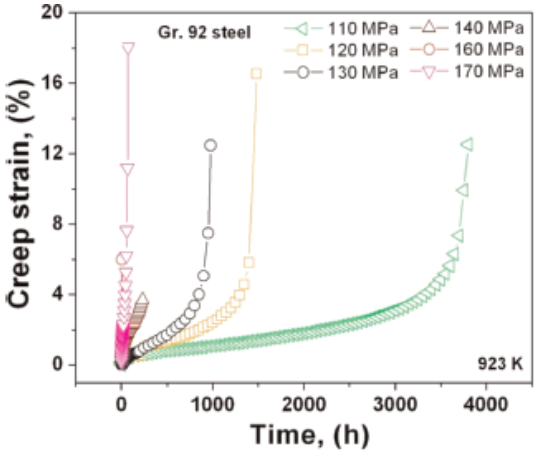

Figure 2.8 Creep strain with time under different stress at 600°C for P92 steel (Sakthivel et al., 2015).

2.3.3 Stress dependence of minimum creep strain rate

Several functions concerning minimum creep strain rate with different stress have been proposed and applied to predict the lifetime for the components within the power station. These include power law, linear power law, hyperbolic sine law and "novel hyperbolic sine law". All investigation is forced on the secondary stage of creep strain.

2.3.3.1 Power law

The typical power law is displayed as Equation 2.1 (Norton, 1929).

$$\dot{\varepsilon}_{min} = A\sigma^n \tag{2.1}$$

where $\dot{\varepsilon}_{min}$ is the minimum creep strain rate, σ is stress, A is creep constant, and n is stress exponent.

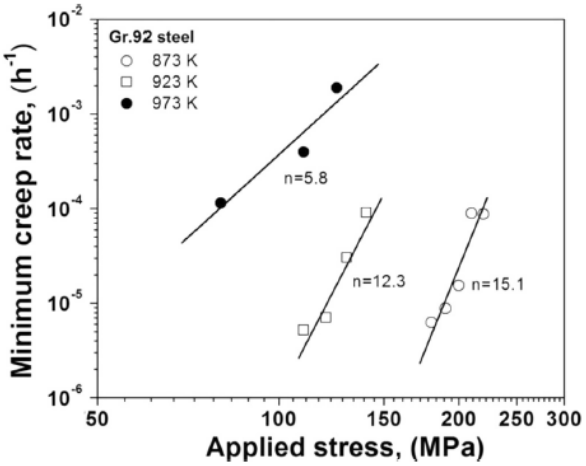

Figure 2.9 The minimum creep strain rate with stress under three different temperatures for P92 steel (Sakthivel et al., 2015).

The minimum creep strain rate with stress under three different temperatures for P92 steel was researched by Sakthivel et al. (2015), which was based on the above power law function. The result is shown in Figure 2.9. According to Sakthivel et al. (2015), the value of A increases approximately 2.2×10^{24} times with the increasing temperature from 600°C to 700°C, while the value of n decreases around 2.6 times for P92 steel. That is based on a narrow range of stress of experimental data. However, some steels need to operate under a wide range of stress, such as in Figure 2.10 at 650°C for P92 steel. The value of stress exponent n is changed from 10.2 to 4.4 (Samuel et al., 2013). This method needs to be divided into two stages to achieve the investigation of the minimum creep strain rate under a wide range of stress.

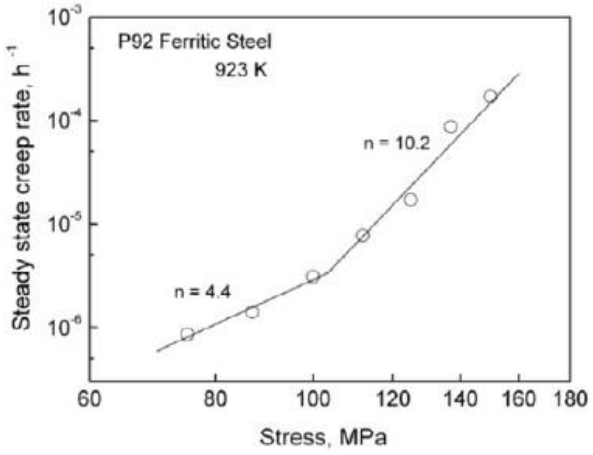

Figure 2.10 The minimum creep strain rate with stress at 650°C for P92 steel (Samuel et al., 2013).

Khayatzadeh et al. (2017a) used the power law equation. They divided three regions to complete the investigation of the relationship between the minimum creep strain rate and a wide range of stress, especially in lower stress levels (Figure 2.11).

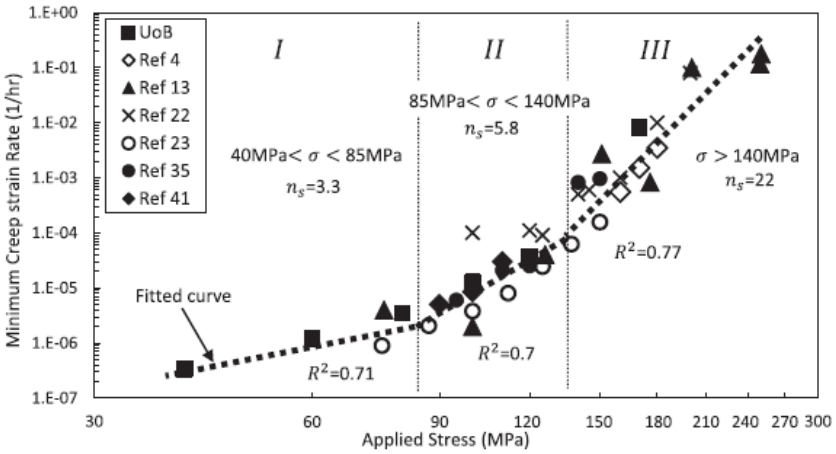

Figure 2.11 The minimum creep strain rate with applied stress at 650°C for P92 steel (Khayatzadeh et al., 2017a).

2.3.3.2 Linear power law

The typical linear power law is shown in Equation 2.2 (Naumenko et al., 2007; Naumenko et al., 2009a).

$$\dot{\varepsilon}_{min} = A\sigma[1 + (B\sigma)^n] \quad (2.2)$$

where $\dot{\varepsilon}_{min}$ is minimum creep strain rate, σ is stress, n is stress exponent, A and B are creep constants.

The linear power law is only suitable to describe the linear creep range in order to get a well fitted curve in high and low stress ranges. However, it cannot be used over or

within transition stress ranges.

2.3.3.3 Hyperbolic sine law

Dyson et al. (1997, 2000) proposed using hyperbolic sine law to discuss the relationship between minimum creep strain rate and stress. The relationship is given in Equation 2.3.

$$\dot{\varepsilon}_{min} = A sinh(B\sigma) \tag{2.3}$$

where $\dot{\varepsilon}_{min}$ is minimum creep strain rate, σ is stress, A and B are creep constants.

The hyperbolic sine law can be used to solve the problem for the limitation of the power law, also suitable on the wide stress levels. However, the hyperbolic sine law cannot be suited in the over stress ranges, especially for the low stresses. The specific limitation is shown in Chapter 5 and combined with the relative case.

2.3.3.4 Novel hyperbolic sine law

In order to overcome the limitation of the above three laws and achieve the minimum creep strain rate under a wide range of stress, the detailed information is indicated in sections 5.2-5.3. The current author's supervisor Dr Qiang Xu proposed the "novel hyperbolic sine law" equation that was successfully applied in a wide range of stress for low Cr steel by Xu (2016) and was used under a wide range of stress for P91 steel by Yang (2018). The function exhibits in the below Equation 2.4.

$$\dot{\varepsilon}_{min} = A \sin h(B\sigma^q) \tag{2.4}$$

where A and B are material parameters, σ is stress, and q is stress exponent.

The results of the above four equations will be compared with their experimental data for high Cr steel and discussed in Chapter 5.

Currently, a variety of creep model equations can be used to represent the deformation behaviour of engineering material at high temperatures. Table 2.1 lists and summarises constitutive equations by Abe et al. (2008). The table is not exhaustive, but it represents the range of creep deformation models currently adopted by the European power generation industry that was recently reviewed by the European Creep Collaboration Committee (ECCC). Many of the involved composition is derived from a small number of classical representations of a primary, secondary, and tertiary creep deformation. Abe et al. (2008) also summarised the classical creep model equations at three creep stages and which is shown in Table 2.2.

Table 2.1 The review of creep constitutive equations used in European Creep Collaborative Committee (ECCC) assessment intercomparisons (Abe et al., 2008; Zhou, 2011).

Model reference	Creep equation
Norton, (Norton, 1929)	$\dot{\varepsilon}_{f,min} = d_1 \exp(-Q/RT)\sigma^n$
Modified Norton	$\dot{\varepsilon}_{f,min} = b_1 \exp(-Q_B/RT)\sigma^n + c_1 \exp(Q_C/RT)\sigma^n$
Norton–Bailey	$\varepsilon_f = d_1\sigma^n t^p$
Bartsch	$\varepsilon_f = e_1 \exp(-Q_1/RT)\sigma \exp(-b_1\sigma)t^p$
(Bartsch, 1995)	$+ e_2 \exp(-Q_2/RT)\sigma \exp(b_2\sigma)t$
Garofalo, (Garofalo, 1965)	$\varepsilon_f = \varepsilon_t[1 - \exp(-b_1 t)] + \dot{\varepsilon}_{f,min} t$
Modified Garofalo	$\varepsilon_f = \varepsilon_{f1}[1 - \exp(-g_1(t/t_{12})^u)$
(Granacher, *et al.*, 2001)	$+ \dot{\varepsilon}_{f,min} t + c_{23}(t/t_{23})f]$
BJF	$\varepsilon_f = n_1[1 - \exp(-t)]^\beta + n_2 t$
(Jones and Bagley, 1996)	where $t = (\sigma/A_1)^n \exp(-Q/RT)$
Li–Akulov model	$\varepsilon_f = \frac{\dot{\varepsilon}_{f,min}}{k} \ln\left(1 + \frac{\dot{\varepsilon}_i - \dot{\varepsilon}_{f,min}}{\dot{\varepsilon}_{f,min}}(1 - \exp(-kt))\right) + \dot{\varepsilon}_s t$
(Li, 1963; Akulov, 1964)	$+ \varepsilon_T(\exp(t/t_t) - 1)$
Theta	$\varepsilon_f = \theta_1[1 - \exp(-\theta_2 t)] + \theta_3[\exp(\theta_4 t) - 1]$
(Evans and Wilshire, 1985)	where $\log(\theta_i) = a_i + b_i T + c_i\sigma + d_i\sigma T$
Modified Theta	$\varepsilon_f = \theta_1[1 - \exp(-\theta_2 t)] + \theta_m t + \theta_3[\exp(\theta_4 t) - 1]$
	where $\theta_m = A\sigma^n \exp(-Q/RT)$
Graham–Walles	$\varepsilon_f = at^{1/3} + dt + ft^3$
(Graham and Walles 1955)	
Modified Graham–Walles	$\dot{\varepsilon}_f = e^{(Q_1/T)} 10^{A_1} \left(\frac{\sigma(1+\varepsilon)}{1+\omega}\right)^{n_1} \varepsilon^{m_1}$
	$+ e^{(Q_2/T)} 10^{A_2} \left(\frac{\sigma(1+\varepsilon)}{1+\omega}\right)^{n_2}$
	where $\dot{\omega} = e^{(-QD/T)} 10^{AD} (\sigma(1+\varepsilon))^{nD} \varepsilon^{mD}$
Rabotnov–Kachanov	$\dot{\varepsilon} = \frac{h_1\sigma^n}{(1-\omega)} \dot{\omega} = \frac{k_1\sigma^v}{(1-\omega)^\zeta}$
(Kachanov, 1986)	
Dyson and McClean,	$\dot{\varepsilon}_f = \varepsilon_0'(1 + D_d)\exp(-Q/RT)\sinh\left(\frac{\sigma(1-H)}{\sigma_0(1-D_p)(1-\omega)}\right)$
(Dyson and McClean, 1998)	
Baker–Cane model	$\varepsilon_f = At^m + \varepsilon_p + \phi\varepsilon_s + \varepsilon_s(\lambda - \phi)\left[1 - \frac{t/t_u - \phi}{1 - \phi}\right]^{\frac{1-\phi}{\lambda-\phi}}$
(Baker and O'Donnell, 2003)	where $I = \varepsilon_u/\varepsilon_s$, $\varepsilon_s = \dot{\varepsilon}_m t_u$ and $\phi = t_p/t_u$
Mech. E (CSWP, 1983)	$R_{u/t/T} = (a_1 + b_1/\varepsilon - c_1\varepsilon^2)R_{E/t/T} + d_1 + e_1/\varepsilon + f_1/\varepsilon^2 - g_1\varepsilon^2$
Characteristic strain	$\varepsilon_f(\sigma) = \varepsilon(R_{u/t/T}/R_{E/t/T} - 1)/(R_{u/t/T}/\sigma - 1)$
model (Bolton, 2005a)	
MHG model, (Grounes, 1969)	$t_\varepsilon = \exp(TF(\varepsilon, \sigma) + C)$ where the $F(\varepsilon,\sigma)$ function is
(Holmström and	freely selected from multilinear combinations of σ
Auerkari, 2004)	and ε with an optimised value of C
Omega, (Prager, 1995)	$\dot{\varepsilon}_f = \dot{\varepsilon}_{f,min}/(1 - \dot{\varepsilon}_{f,min}\Omega t)$
Modified Omega	$\varepsilon_f = \left(\frac{1}{\Omega} - \frac{1}{2C_{tr}}\right)(-\ln(t_u - t) + \ln(t_u))$
(Merckling, 2002)	$+ C_{tr}(1 - \exp(m_{tr}t))$

Table 2.2 The classical creep model equations at three creep stages (Abe et al., 2008).

Model equation	Source reference
Primary creep	
Logarithmic: $\varepsilon_f = a \log(1 + bt)$	Phillips (1905)
Power: $\varepsilon_f = at^b$	Graham and Walles (1955)
Exponential: $\varepsilon_f = a(1 - \exp(-bt))$	McVetty (1933)
Sinh: $\varepsilon_f = a \sinh(bt^c)$	Conway and Mullikin (1962)
Secondary creep	
Power: $\dot{\varepsilon}_{f,min} = d\sigma^n$	Norton (1929)
Exponential: $\dot{\varepsilon}_{f,min} = d \exp(e\sigma)$	
Sinh: $\dot{\varepsilon}_{f,min} = d \sinh(e\sigma)$	Nadai (1938)
Tertiary creep	
Power: $\varepsilon_f = ft^g$	Graham and Walles (1955)
Exponential: $\varepsilon_f = f(\exp(-gt)-1)$	McHenry (1943)
$\dot{\varepsilon}_f = \frac{a\sigma^n}{(1-\omega)^q}$ where $\dot{\omega} = \frac{c\sigma^k}{(1-\omega)^r}$	Kachanov (1958)
	Rabotnov (1969)
Omega: $\dot{\varepsilon}_f = \dot{\varepsilon}_0 \exp(\Omega\varepsilon)$	Prager (1995)

2.3.4 Stress dependence of rupture time

The function of creep rupture time with stress obeying power law is given as the below Equation 2.5 (Samuel et al., 2013; Sakthivel et al., 2015).

$$t_r = A\sigma^{-n} \tag{2.5}$$

where t_r is the creep rupture time, σ is stress, A is creep constant, and n is stress exponent.

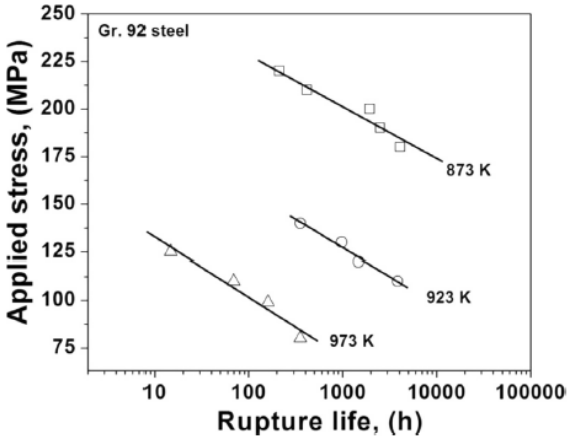

Figure 2.12 The creep rupture time with stress under three different temperatures for P92 steel (Sakthivel et al., 2015).

The creep rupture time under different stress was applied by Sakthivel et al. (2015) to investigate the creep rupture time with stress under three different temperatures for P92 steel (Figure 2.12). Sakthivel et al. (2015) researched and reported, that the value of A decreases approximately 2.68×10^{22} times with the increasing temperature from 600°C

to 700°C, while the value of *n* also decreases from 15.3 to 6.9 around 2.22 times for P92 steel. That is based on a narrow range of stress of experimental data. However, some steels need to operate in a wide range of stress, such as that shown in Figure 2.13 at 650°C for P92 steel. The value of stress exponent *n'*=*n* is changed from 9.7 to 3.9. This method needs to divide two stages to achieve the investigation of the creep rupture time under a wide range of stress. This result is called a breakdown phenomenon of creep strength for P92 steel.

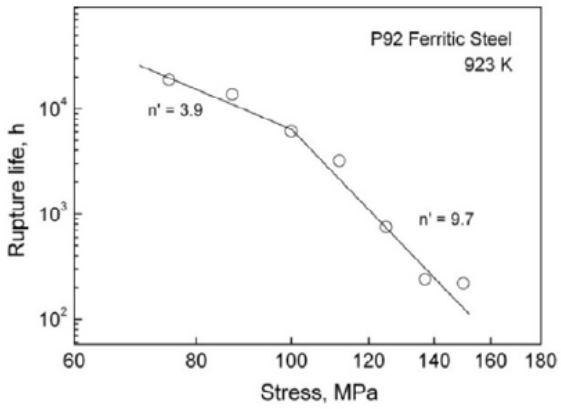

Figure 2.13 The creep lifetime with stress at 650°C for P92 steel (Samuel et al., 2013).

An increasing amount of experimental data concerning the creep rupture time under different stress and temperature has been published, such as that shown in Figure 2.14 which displays a common existing breakdown phenomenon under different temperatures for P92 steel.

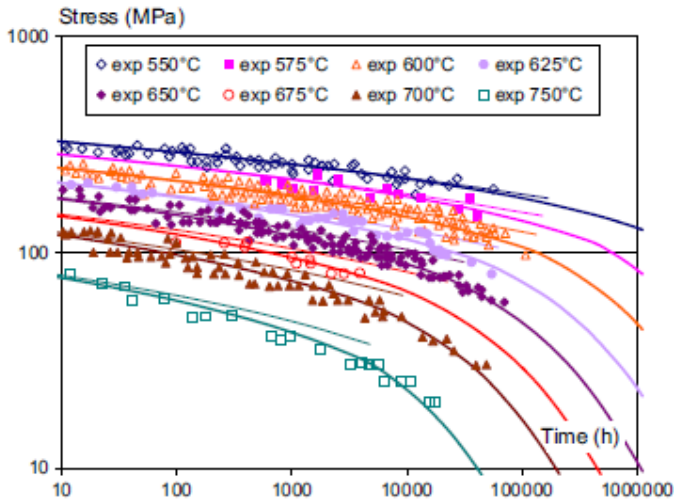

Figure 2.14 The creep rupture time with stress under different temperatures for P92 steel (Petry et al., 2009).

2.4 Creep fracture in steel

The creep rupture map has been summarised by Rediel (1987) for material at different stress and temperature, and it is shown in Figure 2.15. According to the stress level, the fracture can be divided into two mechanisms. The creep fracture can be described as a trans-granular fracture mechanism at high temperature under high stress levels, otherwise, it can be called an inter-granular fracture mechanism at high temperature under low stress levels.

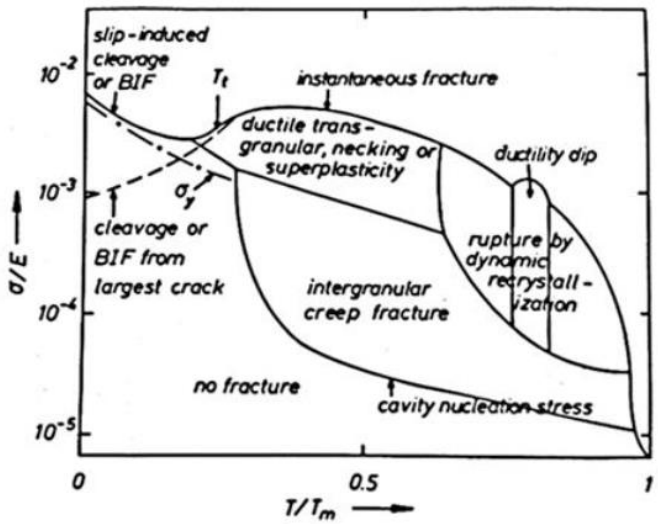

Figure 2.15 Creep fracture map (Riedel, 1987).

Over the past decades, traditional 2D technology has been used to investigate the microstructure and analysis of the creep fracture mechanism for high Cr steel. For example, Transmission Electron Microscopy (TEM), Optical Microscopy (OPM), Scanning Electron Microscopy (SEM), and Electron Backscatter Diffraction (EBSD). Optical Microscopy (OPM) and Scanning Electron Microscopy (SEM) are mainly needed in microstructure examination. Electron Backscatter Diffraction (EBSD) is performed in the visualization of the substructure. Transmission Electron Microscopy (TEM) is not used to observe fracture surfaces, because it is difficult to observe cavitation from fracture surfaces. This technology's experimental results are displayed in Figures 2.16-2.18. The creep cavitation damage is a dominant factor in the design and prediction of a lifetime for components in power plants.

Lee et al. (2006) used Scanning Electron Microscopy (SEM) to research and observe the fracture surface at 550°C-650°C for P92 steel. Figure 2.16 indicates: a) the trans-granular fracture mechanism appeared with dimple model under high stress; b) inter-granular fracture mechanism appeared without a dimple model under low pressure. Lee et al. (2006) also reported the creep cavities are nucleated in coarse precipitates of laves phase along grain boundaries.

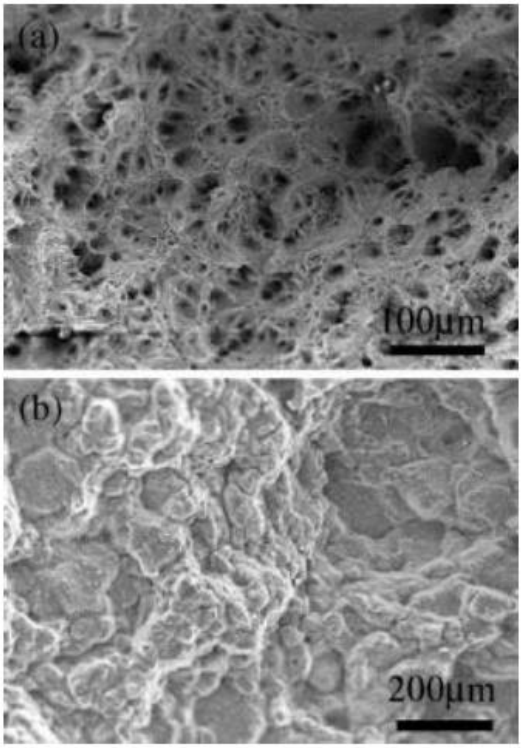

Figure 2.16 SEM images show fracture surfaces for P92 steel: a) 150.2h under 270MPa at 550°C; b) 26,783h under 80 MPa at 650°C (Lee et al., 2006).

Parker's (2013) work was based on traditional Optical Microscopy (OPM) to observe the fracture surfaces for P92 steel. Here, the inter-granular fracture mechanism appeared, and the result of creep cavities is displayed as high density in Figure 2.17.

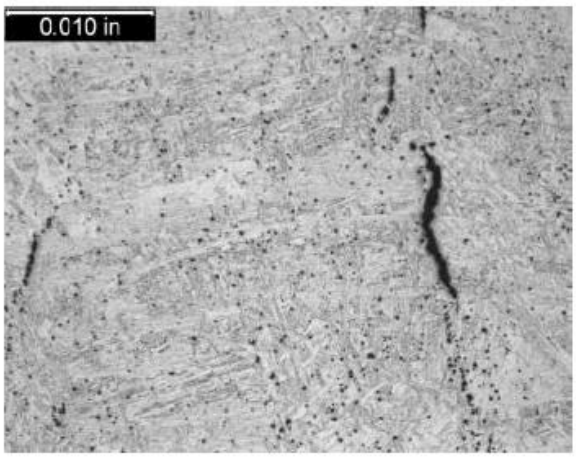

Figure 2.17 OPM image shows fracture surfaces for P92 steel (Parker, 2013).

Aghajani et al. (2009) adopted Scanning Electron Microscopy (SEM) to research and observe the rupture surface under 120MPa at 550°C for high Cr steel (German Grade

X20). Figure 2.18 shows creep cavities occurring on the grain boundary perpendicular to the direction of the applied stress.

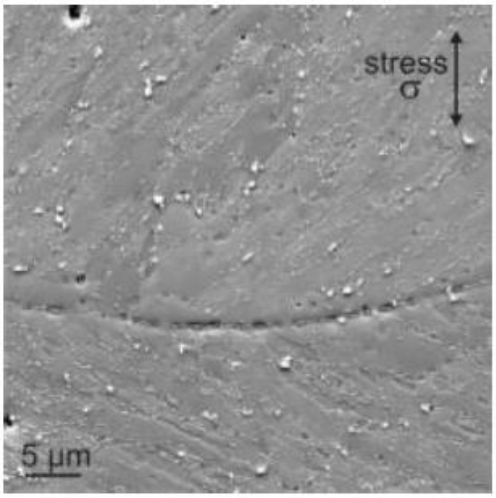

Figure 2.18 SEM image shows fracture surfaces for 12% Cr steel, creep cavities on grain boundary perpendicular to the direction of the applied stress (Aghajani et al., 2009).

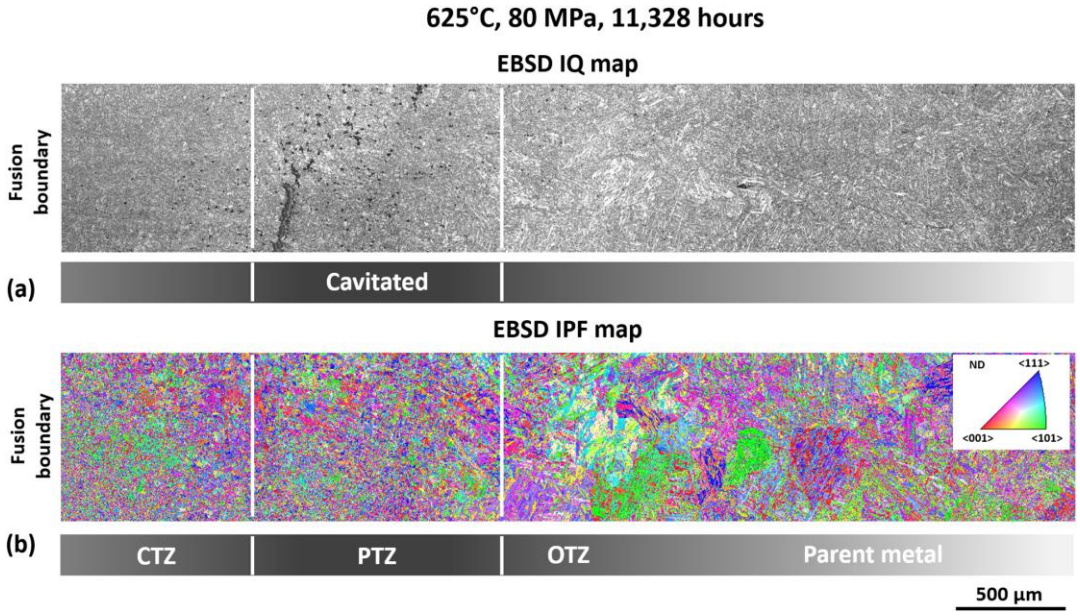

Figure 2.19 EBSD images show fracture model for 9% Cr tempered martensitic steel: a) IQ map at the location of primary creep damage; b) IPF map showing an overview of microstructure in the identical region from the HAZ (Xu et al., 2020).

Xu et al. (2020) reported that using Electron Backscatter Diffraction (EBSD) mapping analysis documents the microstructure in the Heat Affected Zone (HAZ) and the parent metal under 80MPa at 625°C for 9% Cr tempered martensitic steel. The HAZ includes Completely Transformed Zone (CTZ), Partially Transformed Zone (PTZ), and Over

Tempered Zone (OTZ). Figure 2.19 indicates: a) the EBSD Image Quality (IQ) map at the general location of primary creep damage caused by cavitation between ~1000 and ~1400μm from the fusion boundary after 11,328h of creep exposure; b) the EBSD Inverse Pole Figure (IPF) map showing the martensitic microstructure in the same region, and the location of peak damage was determined in the Partially Transformed Zone (PTZ).

According to the above experimental results about rupture surfaces for high Cr steel, the creep cavitation damage is a kinetic phenomenon at the grain boundary, which also affects its creep deformation. The cavity nucleation rate and cavity growth rate affect the main factor for fracture model under different stresses.

2.5 Creep cavitation damage in steel

Generally, it is recognized that cavity nucleation, growth, and coalescence cause the material to fail during creep testing (Gupta et al., 2013). Sklenicka (2003) reported that cavity nucleation and growth are approximately 0.8 times the creep lifetime. Lin et al. (2005) reported the damage is like a cavity at low stress, and the voids may be linked to form a crack at the grain boundary under high stress. This material damage also is divided into microscopic and macroscopic points. From the microscopic point, material rupture is the process of microcavities and microcrack nucleation. For the macroscopic point, the material fracture is caused by cavity coalescence due to the crack's extension. The following section introduces the traditional creep cavitation damage.

2.5.1 Cavity nucleation

According to Lin et al. (2005), cavity nucleation often occurs at grain boundaries at low stress and high temperature, and its creep rate is very low. The schematic is displayed in Figure 2.20.

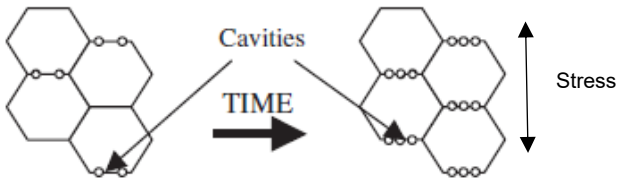

Figure 2.20 The schematic display of cavity nucleation (Lin et al., 2005).

There are three methods for the theories of cavity nucleation, including grain boundary sliding, vacancy condensation at a high stress area and dislocation accumulation. The detail mechanisms of each cavity nucleation are shown in Figure 2.21: a) indicates that grain boundary sliding causes cavitation in the ledges, and formation of the void is located at the top of the boundary or through the tensile grain boundary ledges; b) displays vacancy condensation leads to cavity nucleation at high stress field; c) shows

that dislocation accumulates cavity nucleation; d) describes a particle-obstacle in conjunction with the mechanisms of grain boundary sliding, vacancy condensation and dislocation accumulation.

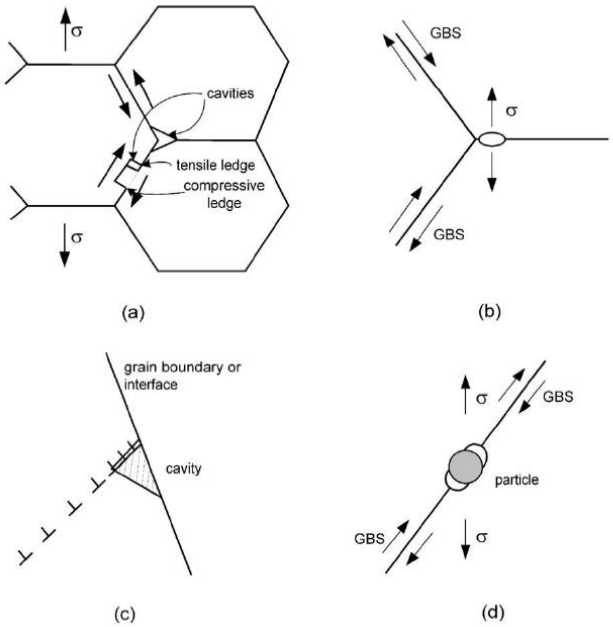

Figure 2.21 Cavity nucleation mechanism: a) sliding at the grain boundary; b) vacancy condensation at a high stress area; c) dislocation accumulated; d) a particle-obstacle in conjunction with the mechanisms described in (a–c) (Kassner et al., 2003).

There are three cavity nucleation rate equations. They are summarised by Riedel (1987) and shown in Equations 2.6, 2.7, and 2.8, respectively.

According to Riedel (1987), Raj and Ashby (1975) proposed Equation 2.6 that is based on the vacancy condensation:

$$\dot{J} = \dot{\beta} N_0^* \tag{2.6}$$

where, $\dot{J}$ is the cavity nucleation rate, N_0^* is the field density of critical clusters, $\dot{\beta}$ is the rate (per unit time) that the critical group absorbs a single vacancy.

According to Kassner et al. (2003), Dyson (1983) proposed Equation 2.7 that is dependent on the strain rate and independent of the time:

$$\dot{J} = \alpha' \dot{\varepsilon} \tag{2.7}$$

where, $\dot{J}$ is the cavity nucleation rate per unit grain boundary, α' is an empirical factor of proportionality (m^{-2}), $\dot{\varepsilon}$ is strain rate.

Riedel (1987) proposed that Equation 2.8 is based on the cavity size function, and the form belongs to the power law:

$$\dot{J} = A_2 t^{\gamma} \tag{2.8}$$

where, $\dot{J}$ is the cavity nucleation rate, A_2 and γ may depend on stress and strain rate, t is time.

2.5.2 Cavity growth

Generally, cavity growth can occur at the grain boundary, and is often controlled by grain boundary diffusion. The creep rate is relatively high. A schematic is displayed in Figure 2.22.

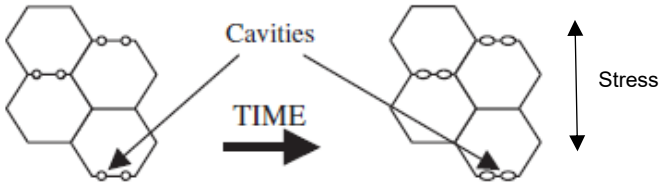

Figure 2.22 The schematic display of cavity growth (Lin et al., 2005).

There are two main ways of cavity growth, including unconstrained diffusion and constrained diffusion. Unconstrained diffusion describes a growth mechanism of an isolated cavity under external stress. The cavity growth theory was originally proposed by Hull and Rimmer (1959). The cavity growth rate is derived below:

$$J_{gb} = -\frac{D_{gb}}{\Omega k T} \nabla f \tag{2.9}$$

$$\nabla f \sim \frac{\Omega}{\lambda_s} (\sigma - \frac{2\gamma_m}{a}) \tag{2.10}$$

where, J_{gb} is the flux, Ω is the atomic volume, k is a Boltzmann constant, T is temperature, $f = -\sigma_{loc}\,\Omega$, σ_{loc} is the local normal stress on the grain boundary, D_{gb} is a diffusion coefficient at the grain boundary, σ is the remote or the applied stress to the grain boundary, λ_s is the cavity separation, γ_m is surface energy terms of metal, a is the cavity radius (Kassner et al., 2003).

By inputting a sintering stress $\sigma_0 = \frac{2\gamma_m}{a}$ into the above Equations 2.9 and 2.10, the cavity growth rate is:

$$\frac{da}{dt} \cong \frac{\Omega \delta D_{gb} (\sigma - \frac{2\gamma_m}{a})}{2kT\lambda_s\, a} \tag{2.11}$$

where, δ is the grain boundary width.

By integrating between the critical radius and $a = \frac{\lambda_s}{2}$, the relationship between stress

and rupture time for cavity growth is as follows:

$$t_r \cong \frac{kT{\lambda_s}^3}{4\Omega\delta D_{gb}(\sigma-\frac{2\gamma_m}{a})} \tag{2.12}$$

Riedel (1987) proposed to improve the relationship between the cavity growth rate and stress with modifications including the diffusion lengths, stress redistribution, cavity geometry and the "jacking" effect (atoms deposited on the grain boundary cause displacement of grains (Kassner et al., 2003)). An improved equation therefore for the unconstrained cavity growth rate of widely spaced voids is, approximately (Riedel, 1987):

$$\frac{da}{dt} = \frac{\Omega\delta D_{gb}()}{1.22kTln\left(\frac{\lambda_s}{4.24a}\right)a^2} \tag{2.13}$$

The diffusion across the cavity surface and by the grain boundaries form cavity growth because of the stress gradient. This is shown in Figure 2.23.

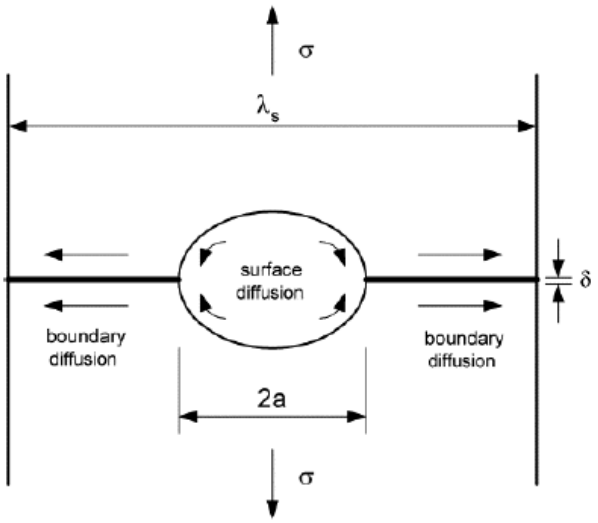

Figure 2.23 Unconstrained diffusion control cavity growth (Kassner et al., 2003).

The other way is constrained diffusion. The theory of constrained cavity growth was originally proposed by Dyson (1976, 1979). Riedel (1987) explained that the deformation rate can control cavity growth rate in the material surround. The cavity growth equation is derived below:

$$\dot{V}_f = \frac{2\pi^2 d^2 \Omega\delta D_b[\sigma_b-(1-\omega)\sigma_0]}{kT{\lambda}^2 q(\omega)} \tag{2.14}$$

where, $\dot{V}_f$ is the total growth rate of the whole facet, σ_0 is sintering stress of an isolated cavity, $\sigma_0 = \frac{2\gamma_s sin\psi}{R}$, ω is the area fraction of cavitated grain boundary, $\omega = (\frac{2R}{\lambda})^2$,

$q(\omega) = -2\,ln\,\omega - (3-\omega)(1-\omega)$, d is the grain size, Ω is the atomic volume, k is a Boltzmann constant, T is temperature, δ is the grain boundary width, D_b is a diffusion coefficient at the grain boundary, σ_b approximates to the sintering stress σ_0, λ is the cavity separation.

By creep deformation of the matrix:

$$\dot{V}_f = \frac{\dot{\varepsilon}_e^{\infty} d^3 \left(1+\frac{3}{n}\right)^{-\frac{1}{2}} (\sigma_I^{\infty} - \sigma_b)}{\sigma_e^{\infty}} \tag{2.15}$$

where, σ_I is the initial stress, σ_b is the back stress, σ_e is the effective stress, $\dot{\varepsilon}_e^{\infty} = B(\sigma_e^{\infty})^n$, $\sigma_e^{\infty} = |\sigma_I^{\infty} - \sigma_T^{\infty}|$.

According to Equations 2.14 and 2.15, the back stress is:

$$\sigma_b = (1-\omega)\sigma_0 + \frac{\sigma_I^{\infty} - (1-\omega)\sigma_0}{1+\frac{2\Omega\delta D_b q' \sigma_e^{\infty}}{[kTq(\omega)\dot{\varepsilon}_e^{\infty}\lambda^2 d]}} \tag{2.16}$$

where, $q' = \pi^2(1+\frac{3}{n})^{\frac{1}{2}}$.

The linear cavity growth rate is:

$$\dot{R} = \frac{2\Omega\delta D_b[\sigma_b - (1-\omega)\sigma_0]}{kTh(\psi)R^2 q(\omega)} \tag{2.17}$$

By replacing Equation 2.16 with Equation 2.17, the constrained cavity growth rate is:

$$\dot{R} = \frac{\sigma_I^{\infty} - (1-\omega)\sigma_0}{h(\psi)R^2\{\frac{q(\omega)kT}{2\Omega\delta D_b} + \frac{q'\sigma_e^{\infty}}{\dot{\varepsilon}_e^{\infty}\lambda^2 d}\}} \tag{2.18}$$

where, $h(\psi)$ is the cavity volume divided by the volume of a sphere with radius R, $h(\psi)=0.61$ with $q'=12.5$, σ_e^{∞} is the applied equivalent stress for axisymmetric loading, $\dot{\varepsilon}_e^{\infty}$ is the equivalent strain rate.

Riedel (1987) reported the cavity growth rate equation and as shown in Equation 2.19, was based on the cavity size function, and the form belongs to the power law:

$$\dot{R} = A_1 R^{-\beta} t^{-\alpha} \tag{2.19}$$

where, $\dot{R}$ is cavity radius growth rate, A_1, α and β may depend on stress and strain rate, R is cavity radius.

2.6 The model of predicting creep lifetime

This part reviews the methods of existing classical creep rupture time models for predicting the creep lifetime concerning components in the power station, and consider

their advantages and disadvantages.

The classical predicting of the creep rupture time models can be divided into two main sets, which includes the empirical model and Continuum Damage Mechanics (CDM) models. The Monkman-Grant (M-G) equation, Omega method and Larson-Miller method belong to the empirical creep model. These models are dependent on the stress and temperature to predate creep lifetime. Other models are based on the relationship between minimum creep strain rate and rupture time (Alang, 2018), such as Kachanov and Robotnov equation, Dyson equation, Hayhurst equation, Yin equation, and Xu equation.

2.6.1 Empirical model

Generally, long term creep rupture testing is required to be carried out to predict the creep rupture time for components in the power plant. The results can show the truthful condition of the components. However, long term creep rupture testing is costly and time consuming. Some research has been based on the short term creep testing data to replace predicting long term creep behaviour accurately.

2.6.1.1 Monkman-Grant equation

The Monkman-Grant (M-G) equation belongs to the empirical model and cannot depend on the applied stress and temperature. It is based on the relationship between minimum strain rate and rupture time. It gives the following Equation 2.20 (Monkman et al., 1956; Sakthivel et al., 2015; Panait, 2010; Sundararajan, 1989; Kvapilova et al., 2013):

$$\dot{\varepsilon}_{min} = (\frac{C_{MGR}}{t_f})^{1/m} \tag{2.20}$$

where, $\dot{\varepsilon}_{min}$ is the minimum creep rate, t_f is the rupture time, m is the constant and close to unity, C_{MGR} the is Monkman-Grant (M-G) constant. The constant of m and C_{MGR} are independent of the test temperature and applied stress.

The advantage of this equation is that once the minimum creep strain rate is known, the long term rupture time of the component can be calculated.

2.6.1.2 Omega method

The omega method is assumed that the whole creep lifetime occurs in the tertiary stage. It conflicts traditional creep deformation mechanism, but it can be used in some component. It is shown in the following Equation 2.21 (Prager, 1995; Alang, 2018).

$$t_r = (\frac{1}{\dot{\varepsilon}_0 \Omega}) \tag{2.21}$$

$$\dot{\varepsilon}_0 = \bar{A}\sigma^{n_0} exp(-\frac{Q_0}{R'T})$$

$$\Omega = A_\Omega \sigma^{n_\Omega} exp(-\frac{Q_\Omega}{R'T})$$

where, $\dot{\varepsilon}_0$ is the initial strain rate, Ω is a parameter for describing the evolution of creep strain, Ā, A_Ω, Q_0, Q_Ω, and n are stress coefficients, R' is the ideal gas constant, T is temperature, t_r is creep rupture time.

The disadvantage of this method is that the primary and secondary creep stages are ignored when originating the model; this leads to predicting not being accurate.

2.6.1.3 Larson-Miller method

The Larson-Miller method was based on the relationship between the applied stress and temperature. It is shown in Equation 2.22 (Larson et al., 1952; Alang, 2018):

$$LMP = T(\hat{C} + logt_r) \tag{2.22}$$

where LMP is the Larson-Miller parameter and dependent stress, T is temperature, t_r is creep rupture time, $\hat{C}$ is a constant.

The disadvantage of this method is that the extrapolation can overestimate the creep rupture time over the long term because the existing degradation phenomenon occurs as a precocious fracture in the material.

2.6.2 Continuum Damage Mechanics (CDM) model

Based on the Continuum Damage Mechanics (CDM) model to develop creep damage constitutive equations have been widely used to describe the creep behaviour and to describe the tertiary creep damage in steel. This is a branch of continuum mechanics and is used to describe the damage and rupture process from the microcavities to the macrocracks in materials (Meng et al., 2019). The method introduced some internal variables to display the macroscopic behaviour and through an average or smeared out style to incorporate cavitation (Xu et al., 2019). In the last two decades, the Continuum Damage Mechanics (CDM) has been widely used in conjunction with the Finite Element (FE) method to predict the creep crack growth of pipes (Meng et al., 2019). The following equations and their advantages and disadvantages are reviewed.

2.6.2.1 Kachanov and Robotnov equation

Kachanov first suggested the Kachanov and Robotnov equation in 1958, and then it was modified and developed by Robotnov in 1969 to describe the creep behaviour in steel. The method was based on the internal state variable to quantify the strain rate for the response to stress. It is displayed in Equation 2.23:

$$\dot{\varepsilon} = \dot{\varepsilon}_0 \left[\frac{\sigma}{\sigma_0(1-D)}\right]^n \tag{2.23}$$

$$\dot{D} = \dot{D}_0 \left[\frac{\sigma}{\sigma_0(1-D)}\right]^v$$

where, $\dot{\varepsilon}$ is creep strain rate, $\dot{D}$ is creep damage rate, $\dot{\varepsilon}_0$ is initial creep strain rate, $\dot{D}_0$ is initial creep damage rate, σ is stress, σ_0 is initial stress, n and v are stress exponents.

The advantage is that the foundation of Continuum Damage Mechanics (CDM) can be built and developed into a creep damage constitutive equation. The simplified material parameter has an obvious benefit for computation, which can be easily put into the finite element program.

The disadvantage is that the material parameter is too simple in that it ignores the impact of more than one potential damage mechanism, such as hardening and particle coarsening.

2.6.2.2 Dyson equation

Dyson (2000) summarised several different creep damage mechanisms for describing the creep behaviour in steel. These are shown in Table 2.3.

Table 2.3 Creep damage categories, mechanisms, and equations (Dyson, 2000).

Categories	Mechanisms	parameter	rate	Strain rate
Strain-induced	Cavity nucleation-Controlled	$D_n = \frac{\pi d^2 N}{4}$	$\dot{D}_n = \frac{K_N}{\varepsilon_{fu}}\dot{\varepsilon}$	$\dot{\varepsilon} = \dot{\varepsilon}_0 sinh\left[\frac{\sigma(1-H)}{\sigma_0(1-D_n)}\right]$
	Cavity growth-controlled	$D_g = (\frac{r}{l})^2$	$\dot{D}_g = \frac{d}{2lD_g}\dot{\varepsilon}$	$\dot{\varepsilon} = \dot{\varepsilon}_0 sinh\left[\frac{\sigma(1-H)}{\sigma_0(1-D_g)}\right]$
	Multiplication of mobile dislocation	$D_d = 1 - \frac{\rho_i}{\rho}$	$\dot{D}_d = C(1-D_d)^2\dot{\varepsilon}$	$\dot{\varepsilon} = \frac{\dot{\varepsilon}_0}{(1-D_d)} sinh\left[\frac{\sigma(1-H)}{\sigma_0}\right]$
Thermally-induced	Particle-coarsening	$D_p = 1 - \frac{P_i}{P}$	$\dot{D}_p = \frac{K_p}{3}(1-D_p)^4$	$\dot{\varepsilon} = \dot{\varepsilon}_0 sinh\left[\frac{\sigma(1-H)}{\sigma_0(1-D_p)}\right]$
	Depletion of solid-solution	$D_s = 1 - \frac{\bar{c}_t}{c_0}$	$\dot{D}_s = K_s {D_s}^{1/3}(1-D_s)$	$\dot{\varepsilon} = \frac{\dot{\varepsilon}_0}{(1-D_s)} sinh\left[\frac{\sigma(1-H)}{\sigma_0}\right]$

To reflect the evolution of creep strain with time, a group of physical creep damage equations was adopted. These equations considered the several mechanisms, including primary strain hardening H, mobile dislocations D_d, particle coarsening D_p and creep cavitation damage D_n, which is displayed below as group Equation 2.24:

$$\dot{\varepsilon} = \frac{\dot{\varepsilon}_0}{(1-D_d)} sinh\left[\frac{\sigma(1-H)}{\sigma_0(1-D_p)(1-D_n)}\right] \quad (2.24)$$

$$\dot{H} = \frac{h'}{\sigma}(1 - \frac{H}{H^*})\dot{\varepsilon}$$

$$\dot{D}_d = C(1 - D_d)^2\dot{\varepsilon}$$

$$\dot{D}_p = \frac{K_p}{3}(1 - D_p)^4$$

$$\dot{D}_n = \frac{K_N}{\varepsilon_{fu}}\dot{\varepsilon}$$

where, $\dot{\varepsilon}$ is creep strain rate, $\dot{\varepsilon}_0$ is initial creep strain rate, σ is stress, σ_0 is initial stress, D_d is mobile dislocation, H is primary strain hardening, D_p is particle coarsening, D_N is cavity nucleation parameter, h', H^*, C, and K_p are material constants, K_N is cavitation constant and up to equal to 1/3, ε_{fu} is uniaxial creep strain at rupture.

The advantage here is that the creep strain rate equations are based on the above four mechanisms. These equations should be more accurate for predicting creep rupture time than the Kachanov and Robotnov equation. What is more, the hyperbolic sine equation can be more suitable for a wide range of stress and temperature than the power law function.

The disadvantage is that the cavitation equation just indicates cavity nucleation. Specifically, it operates the cavity growth rate for zero at the starting of the creep process; these are not satisfying the cavitation damage mechanism.

2.6.2.3 Kachanov-Robotnov-Hayhurst (KRH) equation

These equations have been developed by Hayhurst in 1996, which was based on the Kachanov-Robotnov equation, and included uniaxial and multiaxial versions of creep damage constitutive equations. The uniaxial version is shown in Equation 2.25:

$$\dot{\varepsilon} = Asinh\left[\frac{B\sigma(1-H)}{(1-\varphi)(1-\omega)}\right] \quad (2.25)$$

$$\dot{H} = \frac{h'}{\sigma}(1 - \frac{H}{H^*})\dot{\varepsilon}$$

$$\dot{\varphi} = \frac{K_c}{3}(1 - \varphi)^4$$

$$\dot{\omega} = C\dot{\varepsilon}$$

The multiaxial version is given in Equation 2.26:

$$\dot{\varepsilon}_{ij} = \frac{3S_{ij}}{2\sigma_e} Asinh\left[\frac{B\sigma_e(1-H)}{(1-\varphi)(1-\omega)}\right] \quad (2.26)$$

$$\dot{H} = \frac{h'}{\sigma_e}(1 - \frac{H}{H^*})\dot{\varepsilon}_e$$

$$\dot{\varphi} = \frac{K_c}{3}(1-\varphi)^4$$

$$\dot{\omega} = CN(\frac{\sigma_1}{\sigma_e})^v \dot{\varepsilon}_e$$

where, A, B, C, h', H^* and K_c are material constants in the uniaxial state, H means the primary creep strain hardening, φ is the coarsening of precipitates, ω is the cavitation damage, and up to equal to 1/3 in the uniaxial state, σ_e is effective stress, $\dot{\varepsilon}_e$ is effective creep strain rate, σ_1 is maximum principal stress ($\sigma_1 > 0$, $H=1$; $\sigma_1 < 0$, $N=0$), v is multiaxial stress state index.

The advantage is that two groups of the creep strain rate equation are individually based on the above three mechanisms; these equations should be more accurate for predicting creep rupture time than the Kachanov and Robotnov equation. These are successfully applied to describe the creep behaviour for low Cr steel. What is more, the multiaxial version is suitable for the multiaxial stress state of complex geometry components such as the notched bar.

The disadvantage is that the above method can only be used to predicate creep lifetime but cannot be considered for the consistency of creep deformation; this is reported by Xu et al. (2001, 2004). What is more, the above equations ignore the stress breakdown phenomenon.

2.6.2.4 Xu equation

Dr Qiang Xu's equation was based on the multi-axial Kachanov-Robotnov-Hayhurst (KRH) equation combined with the cavity growth theory to propose a new group of multiaxial creep damage constitutive equations in 2001. It is given below in Equation 2.27 (Xu, 2001):

$$\dot{\varepsilon}_{ij} = \frac{3S_{ij}}{2\sigma_e} A sinh\left[\frac{B\sigma_e(1-H)}{(1-\varphi)(1-\omega_d)}\right] \tag{2.27}$$

$$\dot{H} = \frac{h'}{\sigma_e}(1-\frac{H}{H^*})\dot{\varepsilon}_e$$

$$\dot{\varphi} = \frac{K_c}{3}(1-\varphi)^4$$

$$\dot{\omega} = CNf_2\dot{\varepsilon}_e$$

$$\dot{\omega}_d = \dot{\omega}f_1$$

$$f_1 = (2\sigma_e/3S_1)^{\alpha}\exp\{b\left[\frac{3\sigma_m}{S_s}-1\right]\}$$

$$f_2 = (\exp\{p\left[1-\frac{\sigma_1}{\sigma_e}\right]+q(\frac{1}{2}-\frac{3\sigma_m}{2\sigma_e}]\})^{-1}$$

where, A, B, C, h', H^* and K_c are material constants in the uniaxial state, H means the primary creep strain hardening, φ is the coarsening of precipitates, ω is the cavitation damage, σ_e is effective stress, σ_1 is maximum principal stress, $\dot{\varepsilon}_e$ is effective creep strain rate, σ_1 is maximum principal stress ($\sigma_1 > 0$, $H=1$; $\sigma_1 < 0$, $N=0$), v is multiaxial

stress state index. f_1 and f_2 are functions of stress states, $S_s = \sqrt{{\sigma_1}^2 + {\sigma_2}^2 + {\sigma_3}^2}$, $\sigma_m = 1/3(\sigma_1 + \sigma_2 + \sigma_3)$, and $S_1 = \sigma_1 - \sigma_m$.

The advantage is that the modelling results can fit very well with the experimental data for low Cr steel. From the phenomenological aspect, the results can unite the tertiary stage of creep deformation and creep damage. The model can be more accurate to predicate the creep deformation and rupture time.

The disadvantage of these equations is that they lack consideration for the stress breakdown phenomenon.

2.6.2.5 Yin equation

Yin et al. (2006) explored Dyson's equation to propose a new creep damage constitutive equation by adding an exponent for creep rate. It is shown in Equation 2.28:

$$\dot{\varepsilon} = \frac{\dot{\varepsilon}_0}{(1-D_d)(1-D_s)} sinh\left[\frac{\sigma(1-H)}{\sigma_0(1-D_p)(1-D_n)}\right] \tag{2.28}$$

$$\dot{H} = \frac{h'}{\sigma}(1 - \frac{H}{H^*})\dot{\varepsilon}$$

$$\dot{D}_d = C(1 - D_d)^2\dot{\varepsilon}$$

$$\dot{D}_p = \frac{K_p}{3}(1 - D_p)^4$$

$$\dot{D}_s = K_s {D_s}^{1/3}(1 - D_s)$$

$$\dot{D}_n = A'\varepsilon^{B'}\dot{\varepsilon}$$

where, A', B', C, h', H^*, K_s and K_p are material constants, $\dot{\varepsilon}$ is creep strain rate, $\dot{\varepsilon}_0$ is initial creep strain rate, σ is stress, σ_0 is initial stress, D_d is mobile dislocation, H is primary strain hardening, D_p is particle coarsening, D_s is solute depletion, D_N is cavity nucleation parameter.

The advantage of the above is that the creep strain rate equation is based on the above five mechanisms; the equation should be accurate for predicting creep rupture time. The new equation can accept that the creep cavitation damage can be quickly increased with increasing the creep strain because of adding the exponent of creep strain.

The disadvantage is that the cavitation damage model has not been further validated by experimental data for the cavity evolution. The material constant A depends on the stress as well as the temperature.

Yadav et al. (2016) adopted and modified Yin's cavitation damage equation into Orowan's equations to investigate the cavitation damage mechanism and creep deformation mechanism for P92 steel, the modified constitutive equation is displayed in Equation 2.29:

$$\dot{\varepsilon} = \frac{bp_m v_g}{M(1-D_p)(1-D_n)} \tag{2.29}$$

$$\dot{D_p} = \frac{K_p}{3}(1 - D_p)^4$$

$$\dot{D_n} = A\varepsilon\dot{\varepsilon}$$

Based on the above Equation 2.29, the model results at different temperature and applied stress for P92 steel are shown in Figure 2.24, which considers the influence of particle coarsening mechanism and cavitation mechanism. The simulated result almost fitted well with their experimental data especially at the tertiary stage of the creep program. As a result, they can verify that the particle coarsening mechanism and cavitation mechanism act as essential factors in creep damage for high Cr steel.

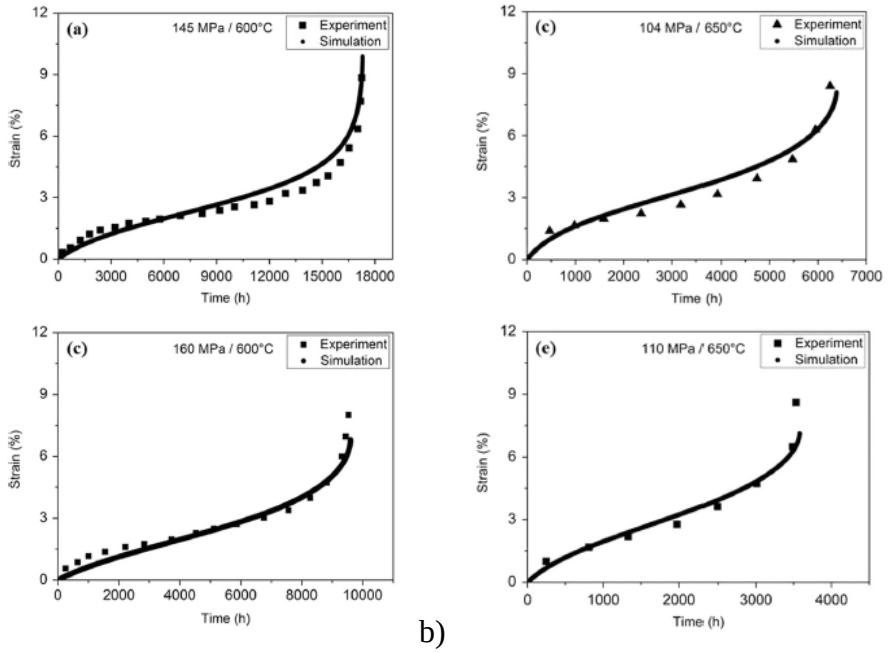

a) b)

Figure 2.24 Model results compared against experimental data at different temperature and applied stress for P92 steel (Yadav et al., 2016).

Yadav et al. (2016) also reported that the applied stress and temperature could affect the value of material constant *A* in the creep cavitation damage equation. The values of material constant *A* steel under different stress and temperature for P92 are given in Table 2.4 and shown graphically in Figure 2.25 (Zheng et al., 2020).

Table 2.4 The values of material constant A (s^{-1}) under different stress and temperature for P92 steel (Yadav et al., 2016).

Stress (MPa)	600 °C	650 °C
92		2.19×10^{2}
104		2.92×10^{2}
110		3.81×10^{2}
145	1.93×10^{2}	
160	4.25×10^{2}	

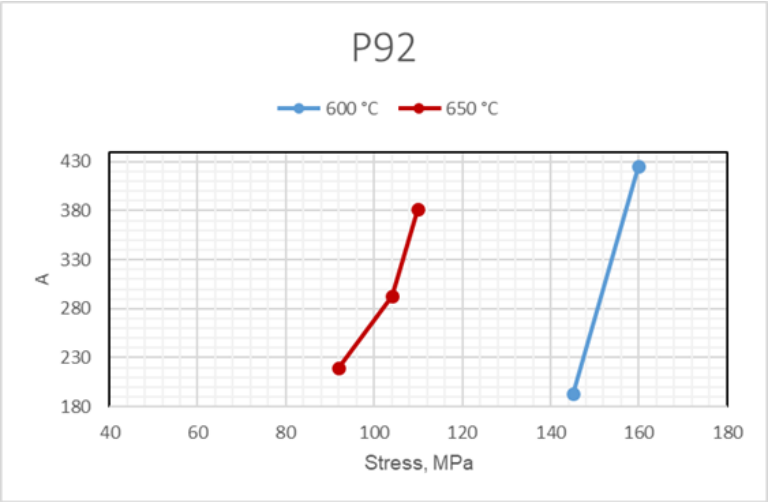

Figure 2.25 The values of material constant A under different stress and temperature for P92 steel (Zheng et al., 2020).

It is difficult to use the constitutive equation modelling for an accurate prediction as the life. This is because the trend of parameter A is based on three, and two experimental points at 600°C and 650°C in Figure 2.25, respectively.

2.7 The current state of experimental data for high Cr steel

The current state of experimental data for high Cr steel is summarised and listed below:

(1) European Creep Collaborative Committee (ECCC) and National Institute for Materials Science (NIMS) principally publish the creep data sheet. They have been evaluated and published for high Cr steels, including P/T91, P/T92, CB8 and E911.

(2) Using the traditional 2D technology observe the fracture surfaces for high Cr steel, such as Optical Microscopy (OPM) and Scanning Electron Microscopy

(SEM). The experimental observation indicates the cavitation damage mechanism dominate creep damage in some material.

(3) Using the advanced 3D X-ray microtomography technology can catch the high resolution and continuity of the process for the cavitation and observe the process of increasing creep cavity with time. For example, the European Synchrotron Radiation Facility (ESRF) and the Japan Synchrotron Radiation Research Institute (JSRRI) have this technology. These experimental data can be provided with a better survey and foundation to investigate the characteristic of the cavity nucleation and cavity growth, which exactly develop creep cavitation equations for achievement the predicting the creep lifetime of components in the power plant.

2.8 The existing new method for developed creep damage constitutive equation

The existing new method for developed creep damage constitutive equation is summarised and listed below:

(1) The "novel hyperbolic sine law" is the newest equation for describing the minimum creep strain rate over a wide range of stress. It has the best adaptability because the development is based on the published experimental data under the widest range of stress at present. The equation was originally proposed by Dr Qiang Xu and is successfully applied for low Cr steels by Xu (2016), such as 2.25Cr-1Mo and 0.5Cr-0.5Mo-0.25V steel under a wide range of stress levels from 10MPa to 300MPa. In addition, the "novel hyperbolic sine law" for P91 steel at 600℃ and 625℃ was successfully applied by Yang (2018) under a wide range of stress.

(2) The novel creep cavitation damage equation is the latest method to predict lifetime for components because the methodology is based on the cavity nucleation and cavity growth model and it has adopted the advanced 3D x-ray microtomography technology to produce the cavitation data. The theory is based on Riedel's function of cavity size distribution at the grain boundary. The equation was successfully developed and applied for P91 steel by Yang (2018). The traditional creep damage equation is based on the creep strain to predict lifetime for components; this is not accurate.

(3) The relationship between *U'* and stress for P91 steel was firstly suggested and reported a trend curve by Xu (2018a) and Xu et al. (2019). It was proposed that there exists a relation between *U'* and stress for P91 steel (Xu., 2018a; Xu et al., 2019).

2.9 Summary

This chapter summarises and reviews the related literature in the field. This includes the creep deformation and fracture mechanisms, the advantages and disadvantages of the existing predicting model, the existing novel creep damage constitution equation, and the current state of experimental data for developed creep damage constitution equations. Some critical comments, given such as the conventional method, need to be divided into two or three stages to achieve the investigation of the relationship of minimum creep strain rate under a wide range of stress. The CDM models include the cavitation damage mechanism that dominates the factor in the process of creep fracture occurring at grain, but they are not discussing the condition of the cavitation damage mechanism that happened in the grain boundary. The most developed equations are proposed which, based on the high stress levels when extended to the low stress levels, the model results which are not the same as experimental data, create a stress breakdown phenomenon. This chapter describes the related information in this area that can help the author to build a strong foundation and quickly and accurately develop creep damage constitutive equations.

Chapter 3 Methodology

3.1 Introduction

This chapter displays the process and method of development and application of creep damage constitutive equations for high Cr steels based on the mechanisms of cavitation damage. The process includes: 1) to apply and calculate a “novel hyperbolic sine law” for minimum creep strain rate under a wide range of stress, the new development achieves the “novel hyperbolic sine law” equation over a wide range of stress for P92 steel; 2) to apply a new cavitation damage equation for a new high Cr steel, the new achievement forces on the application of this method for E911 steel; 3) to involve creating a creep cavitation rupture modelling, the new achievement develops and applies the modelling under a wide range of stress for P92 steel; 4) to calibrate a creep cavitation model at different stages of creep lifetime, that the application achieves the model can be used at any stages of creep lifetime for 316H steel, not just suitable at rupture time. Each process of this research method is shown in Figure 3.1 (Ghauri et al., 2005).

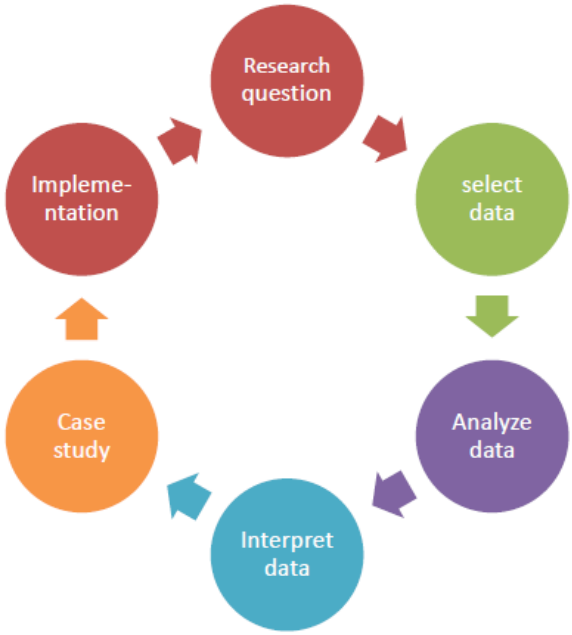

Figure 3.1 Flowchart of the research method in each process (Ghauri et al., 2005).

Ghauri et al. (2005) suggested the above flowchart idea, after which Sheridan (2010) also reported them. An (2015) also repeated the same view in her work.

3.2 The process of this research method

The process of this research method includes four parts and its connection in the research framework is shown in Figure 3.2.

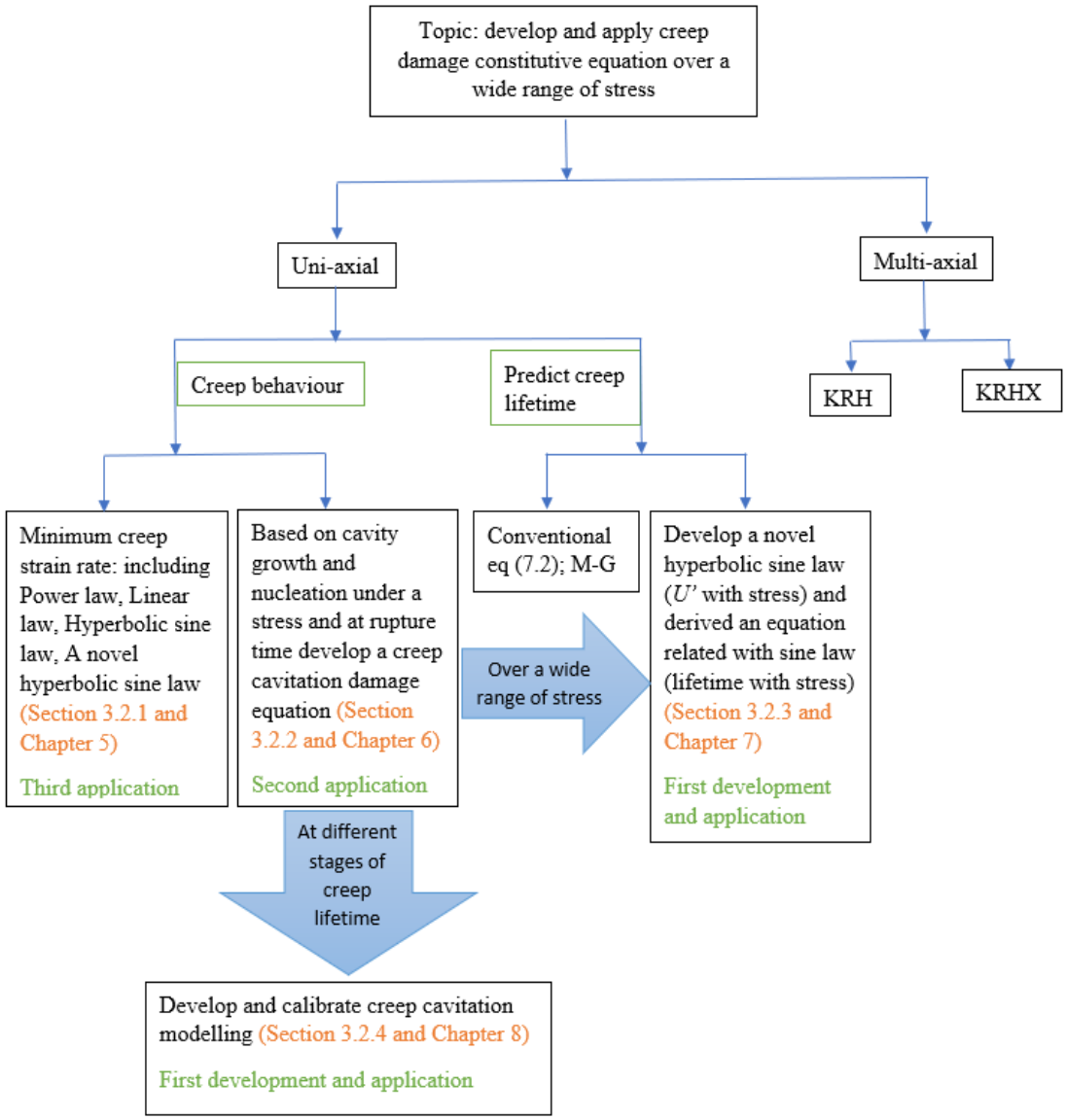

Figure 3.2 The connection of the objectives in the research framework.

3.2.1 The operation of the application and calculation for a novel minimum creep strain rate equation under a wide range of stress

The methodology for applying and calculating a novel minimum creep strain rate under a wide range of stress is:

(1) Selecting experimental data for describing the relationship between the minimum creep strain rate and stress under a wide range of stress such as stress range from 70MPa to 200MPa at 600℃ for P91 and stress range from 120MPa to 250MPa at 600℃ for P92 steel. The corresponding details are given in section 4.2.1 and section 4.3.5.

(2) Analysing and coupling the above experimental data with the classical constitutive equations such as power law, linear power law and hyperbolic sine law. The corresponding results are displayed in section 5.2.

(3) Studying a case to understand the method that according to the content of a published article by Xu et al. (2017a), and independently to modify and apply the novel minimum creep strain rate equation under a wide range of stress for P91 steel. The operational process is to continuously adjust the values of material parameters A and B in Equation 5.1 to achieve the curve results that can fit very well with the overall experimental points. This step is a review and study process, and the relevant detailed results are shown in section 5.3.

(4) Implementing a case based on the above method to apply the novel minimum creep strain rate equation under a wide range of stress for P92 steel at different high temperatures. The operational process is to continuously adjust the values of material parameters A and B in Equation 5.1 to achieve the curve results that can fit very well with the overall experimental points. The relevant results are given in section 5.3.

(5) Comparing and discussing the results produced by the "novel hyperbolic sine law" with its works by traditional constitution equations and experimental data. The corresponding results are shown in section 5.4.

3.2.2 The operation of the application and calculation for new cavitation damage equation

The methodology for applying and calculating a new cavitation damage equation is:

(1) Selecting the x-ray microtomography cavitation data. This data should include the relationship between the number of cavity and radius, and also publish the rupture time such as for P91 and E911 steels. The corresponding details are in section 4.3.1.

(2) Studying a case to know the operational way according to the content of a published article by Xu et al. (2017a), and independently to apply and calculate the new cavitation damage equation for P91 steel. The working process is to determine five material constants A_1, A_2, α, β, and γ in Equation 6.1, which

depend on stress, and continuously repairing the values of A_1, A_2 to achieve the curve results can fit almost experimental points. And to summarise the existing approach and to develop a new way to accomplish the determination for five material constants. This step is a review and study process, and the relevant detailed information is shown in section 6.2 and section 6.3.1.

(3) Implementing a case based on the above develop a new method to apply and calculate the new cavitation damage equation for E911 steel. The working process is determinate five material constants A_1, A_2, α, β, and γ in Equation 6.1, and continuously repairing the values of A_1, A_2 to achieve the curve results can fit almost experimental points. The relevant detail information is displayed in section 6.2 and section 6.3.2.

(4) Comparing and discussing the result of the new cavitation damage equation with its experimental data. The corresponding results are shown in section 6.3.2.

3.2.3 The process to develop and apply a creep cavitation rupture modelling for P92 steel

The methodology for developing and applying a creep cavitation rupture modelling is:

(1) Selecting experimental data for describing the relationship between the creep rupture time and stress such as P91and P92 steels at different temperatures. The corresponding details are in section 4.2.2.

(2) Analysing the above experimental data and couples with Equation 6.12 to calculate the values of coefficient U' under different stresses for P91 and P92 steels. This calculation for P91 steel is the reviewing and studying process. The relevant detailed results are displayed in section 6.3.

(3) Developing a new function for describing the relationship between coefficient U' and stress that data based on the above values for P92 steel. The operational process is to adjust the material constants to achieve the curve results continuously can fit very well with the overall experimental data. The relevant results are given in section 7.2.

(4) Rewriting a new equation for describing the relationship between stress and rupture time are based on the developed new function and material constants in the above step (3) to couple with Equation 6.12. The relevant results are indicated in section 7.3.

(5) Adopting the M-G equation to research the relationship between minimum strain rate with rupture time. The working process is to continuously adjust the

material parameters M and C to achieve the curve results, which can fit well with the overall experimental points. The corresponding results are shown in section 7.4.

(6) Rewriting a new equation for describing the relationship between coefficient U' and minimum strain rate is based on the M-G equation and material parameters in the above step (5) to couple with Equation 6.12. The relevant results are shown in section 7.5.

(7) Comparing and discussing the results of a creep cavitation rupture modelling for P92 steel with their experimental data. The corresponding results are in sections 7.2-7.5.

3.2.4 The process to develop and calibrate a creep cavitation model at different stages of creep lifetime for 316H steel

The methodology for developing and calibrating a creep cavitation model at different stages of creep lifetime for 316H steel is:

(1) Selecting experimental cavitation data for describing the relationship between the number of cavity and radius at different stages of a lifetime for 316H steel. The corresponding details are in section 4.4.4.

(2) Experimental data is analysed and combined with the theory of section 6.2 and the method of section 6.3.2 to apply novel cavitation damage equations at different stages of creep lifetime for 316H steel. The working process is to determine five material constants at various stages of creep lifetime respectively, and continuously repair the values of A_1, A_2 to achieve the curve results can fit almost every stage's experimental points. The relevant detailed information displays in section 8.2 and section 8.3.

(3) Comparing and discussing the results is produced by a creep cavitation model at different stages of creep lifetime for 316H with their experimental data. The corresponding results are in sections 8.2-8.3.

(4) The characteristics of the creep cavitation damage for 316H is based on the values of material constants of A_1, A_2 at rupture time, including the process of W, J, R and R rate with time, are discussed. The relevant information and results are displayed in section 8.4.

3.3 Summary

This chapter summarises the process of the research method, lists each process of four parts, respectively, and points out where they have been introduced in detail in the following chapters. This chapter also can help the reader more quickly and efficiently to understand the contents in the subsequent chapters. The new developments for the method in this chapter are as follows: 1) achieving the third application of the “novel hyperbolic sine law” equation over a wide range of stress for P92 steel; 2) achieving the second application of cavitation damage method for E911 steel; 3) achieving the first development and application of a creep cavitation rupture modelling under a wide range of stress for P92 steel; 4) achieving the creep cavitation model can be used at any stages of creep lifetime for 316H steel, not just suitable at rupture time. This current study is the first attempt at the development and use of this method.

Chapter 4 Collection and analysis of the experimental data for high Cr steel

4.1 Introduction

To achieve the development of creep damage constitutive equations for high Cr steel over a wide range of stress, the collection and analysis of the experimental data for high Cr steel should be solved first. The following four aspects should be satisfied with the collection of experimental data:

(1) For applying and calculating a novel minimum creep strain rate equation under a wide range of stress, the detailed experimental data of the minimum creep strain rate under a wide range of stress needs to be available, which include more detailed data under low stress levels (the related method is shown in section 3.3.1 and related results are included in Chapter 5).

(2) For applying and calculating a new cavitation damage equation, the experimental data is based on the x-ray microtomography cavitation data which includes the relationship between the number of cavity and radium, and also the published rupture time (the related method is shown in section 3.3.2 and related results are included in Chapter 6).

(3) For developing and applying a creep cavitation rupture modelling, the experimental data of the creep rupture time is available under a wide range of stress (the related method is shown in section 3.3.3 and related results are included in Chapter 7).

(4) For developing and calibrating a creep cavitation model at different stages of creep lifetime, the experimental data of the cavity size distribution with growth time is included (the related method is shown in section 3.3.4 and related results are included in Chapter 8).

The x-ray microtomography cavitation data used in this research project is based on a synchrotron radiation experiment. The data was carried out on the beamline of the Spring-8, the synchrotron radiation facility in Japan. Due to the linear absorption coefficient of aluminium and steel, the x-ray energy was set at 20 keV (Kobayashia et al., 2014). The synchrotron radiation facility is displayed in Figure 4.1.

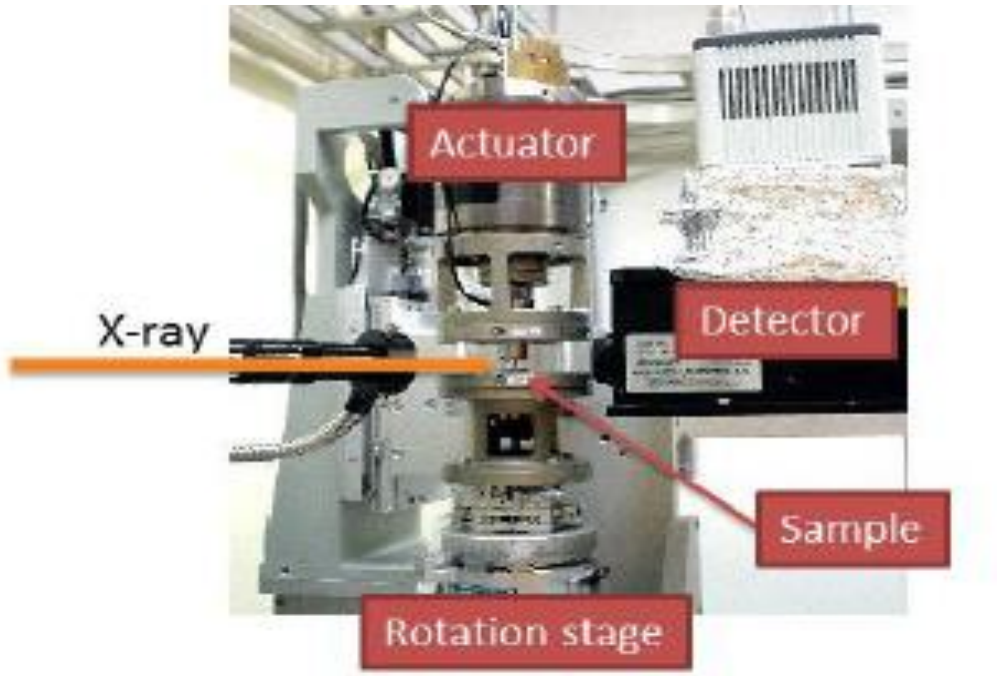

Figure 4.1 Synchrotron radiation facility (Kobayashia et al., 2014).

4.2 The experimental data of creep test for high Cr steel based on the NIMS data sheet

4.2.1 Minimum creep strain rate under different stress at 600℃ and 650℃ for P91 and P92 steels

The experimental data of minimum creep strain rate under different applied stresses were adopted from NIMS creep data sheet. The reason for choosing this data is that the minimum creep strain rate is under a wide range of stress which includes more detailed data under low stress levels. Another reason is that the NIMS data sheet is also published and includes the related experimental data of the creep rupture times under different stress (section 4.2.2); that part will be investigated in Chapter 7. Thus, the characteristics of this choosing of experimental data are the wide stress levels and simultaneously include specific data such as minimum creep strain rate, stress, and rupture time. The modelling method is shown in section 3.3.1. The results of the power law, linear power law, conventional hyperbolic sine law and "novel hyperbolic sine law" will be compared with their experimental data, with detailed information outlined in Chapter 5. This part, including experimental data of two materials at two temperatures, is summarised and shown in the Appendix (Tables 1-3).

4.2.2 Creep rupture times under different stress at 600℃, 625℃ and 650℃ for P91 and P92 steels

The experimental data of creep rupture times under different applied stresses were taken from NIMS creep data sheet to develop creep cavitation modelling. The reason for choosing this data is that the creep rupture times are under a wide range of stress, the NIMS data sheet, including the related experimental data of the minimum creep strain rate under different applied stresses (section 4.2.1). This will also be investigated in Chapter 5. Thus, the characteristics of this choosing of experimental data are the wide stress levels which simultaneously include specific data such as minimum creep strain rate, stress, and rupture time. The modelling method is shown in section 3.3.3. The detailed modelling results will be shown in section 6.4 and Chapter 7. This part, also including experimental data of two materials at two temperatures, which were summarised are shown in the Appendix (Tables 4-8).

The sample and type separately for the tube and MJT at 600℃ for P92 steel are shown in Figure 4.2.

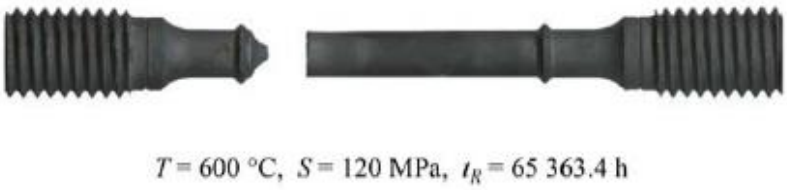

1)

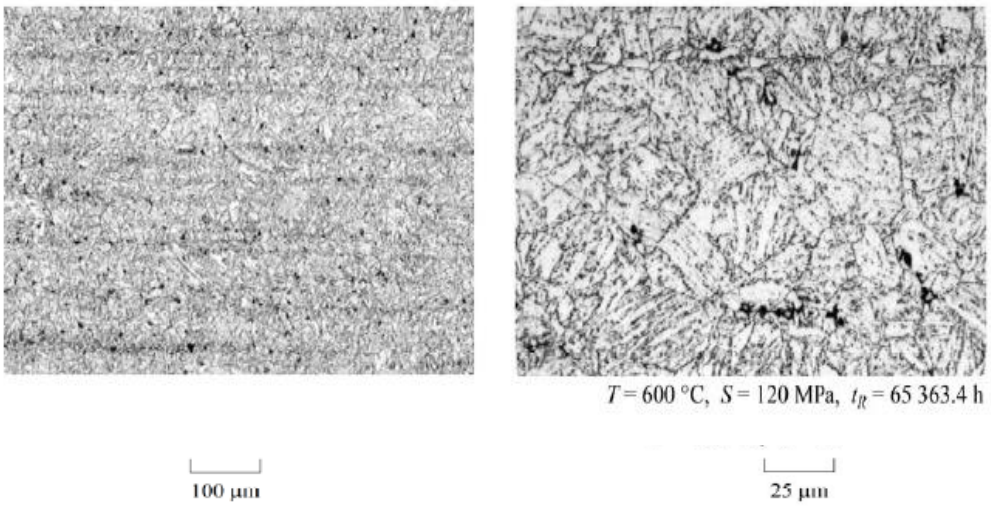

2)

Figure 4.2 Specimen ruptured at 600℃ for P92 (9Cr–1.8W–0.5Mo–V-Nb) steel tube, MJT: 1) Profiles; 2) Microstructures (NIMS, 2018).

The sample and type separately for the pipe and MJP at 650℃ for P92 steel are shown

in Figure 4.3.

1)

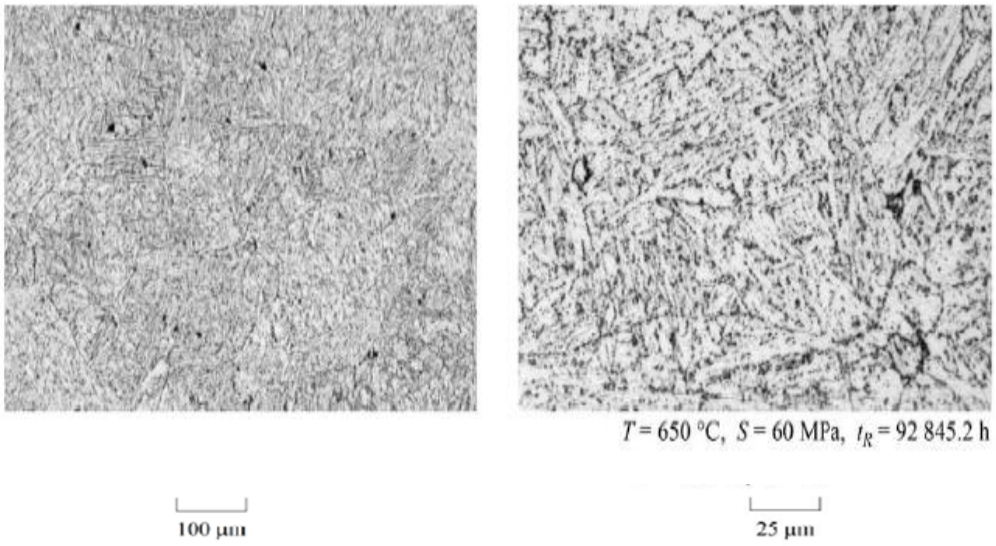

2)

Figure 4.3 Specimen ruptured at 650℃ for P92 (9Cr–1.8W–0.5Mo–V-Nb) steel pipe, MJP: 1) Profiles; 2) Microstructures (NIMS, 2018).

4.3 The experimental observation of cavitation damage in high Cr steel

This section outlines the collected experimental observation with cavitation characterisation to apply the novel cavitation damage equation and to predict creep rupture time.

4.3.1 The observation of cavitation damage for P91 and E911 steels

The conditions of creep testing are shown in Table 4.1 for P91 (9-1%CrMoVNb) and E911 (9-11%CrMoWVNb) (Sket et al., 2010; Renversade et al., 2014). The tomographic reconstruction of damage and its microstructures are shown in Figures 4.4 and 4.5, respectively. The reason for choosing this data is that there is a known relationship between the number of cavity and radium, and also there is published rupture time. This data is available and the necessary condition to apply and calculate a new cavitation damage equation is outlined in section 6.3. The applied method is outlined in section 3.3.2. However, the NIMS data sheet (section 4.2.1 and section 4.2.2)

cannot be produced and published for the relative experimental data.

Table 4.1 Creep testing conditions summary (Sket et al., 2010; Renversade et al., 2014).

Material	Temperature (°C)	Axial Stress (MPa)	Internal Pressure (MPa)	Rupture time (h)
E911	575	61.8	17.5	26000
	600	48.9	17.7	37800
P91	575	52.6	23.6	10200

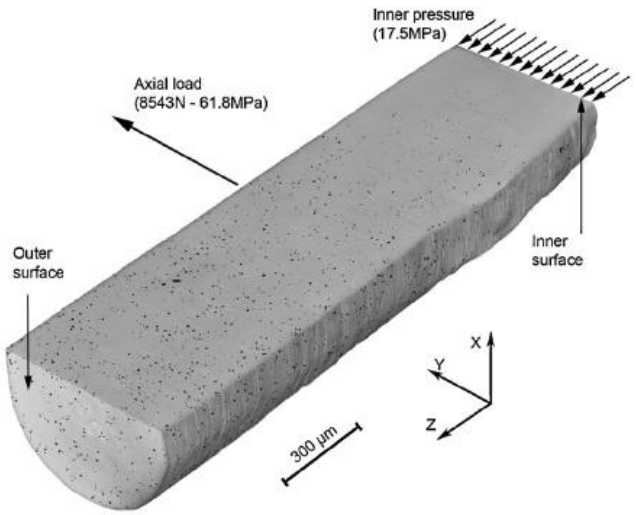

1)

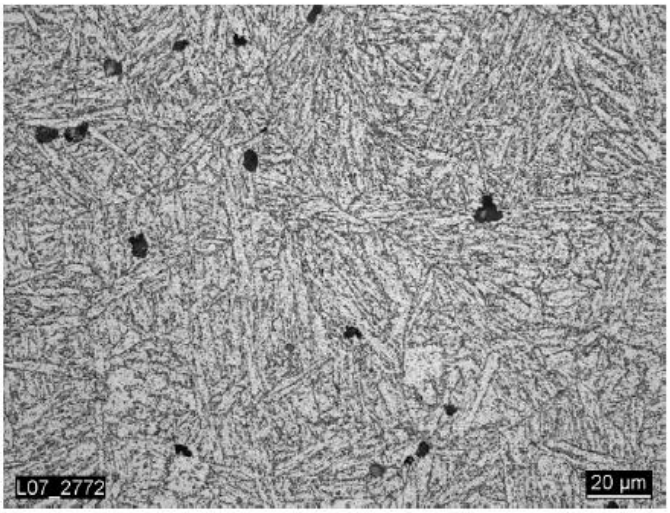

2)

Figure 4.4 The E911 steel after 26000h: 1) Tomographic reconstruction of void spatial distribution; 2) Microstructures (Sket et al., 2010).

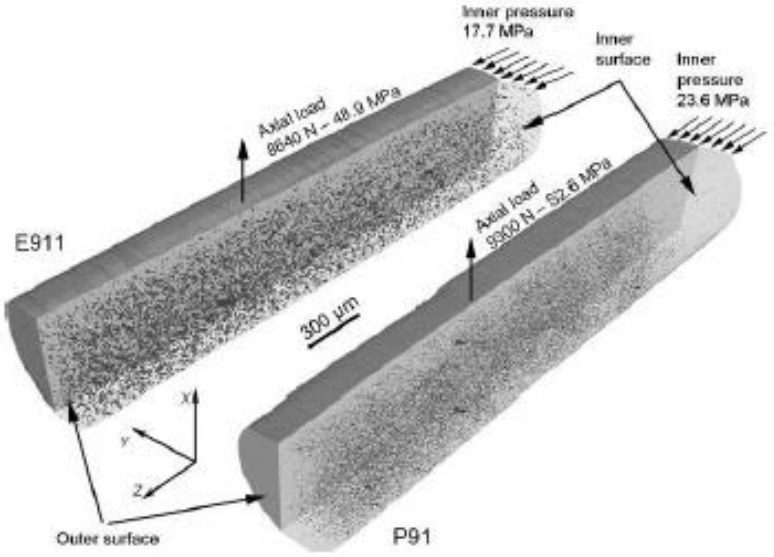

1)

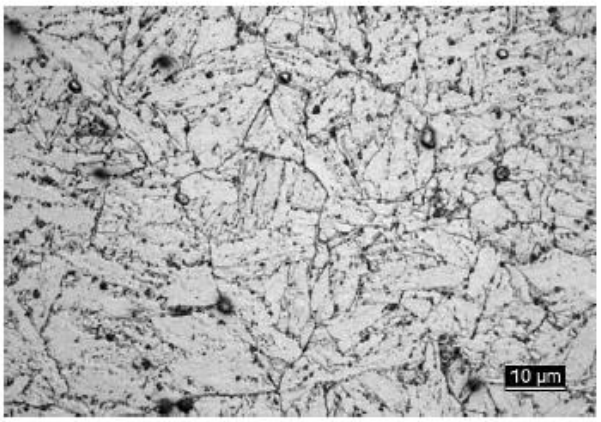

2) (a)

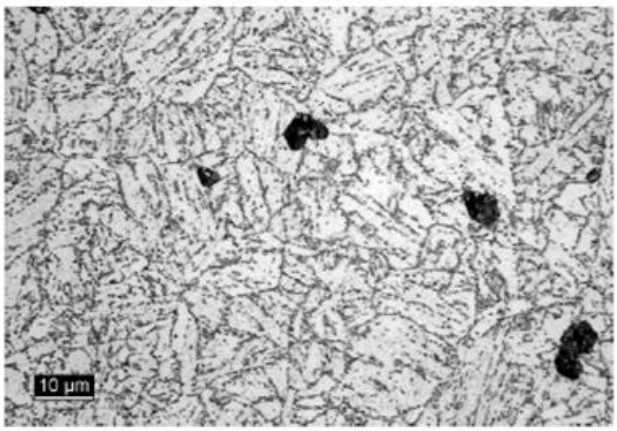

(b)

Figure 4.5 The P91 steel after 10200h and the E911 steel after 37800h: 1) Tomographic reconstruction of void spatial distribution; 2) Microstructures (a) P91, (b) E911 (Renversade et al., 2014; Gupta et al., 2015).

The size distribution of non-coalesced voids for P91 and E911 are shown in Figures 4.6 and 4.7, respectively.

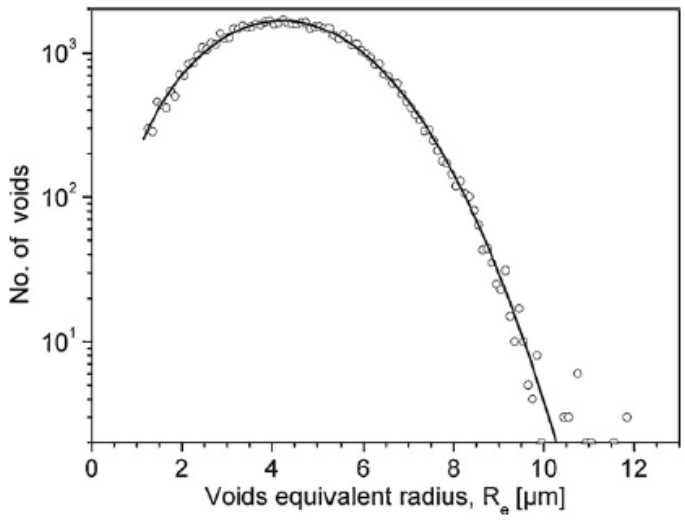

Figure 4.6 The size distribution of non-coalesced voids at 575°C for E911(Sket et al., 2010).

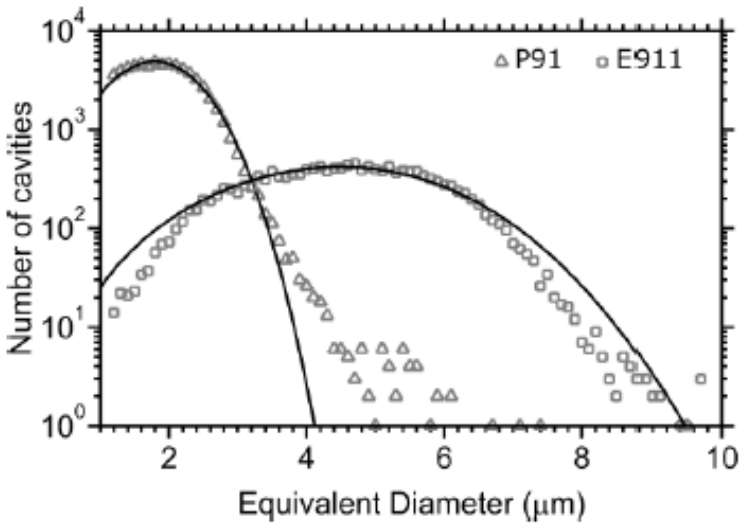

Figure 4.7 The size distribution of non-coalesced voids for P91 and E911 steels (Renversade et al., 2014; Gupta et al., 2015).

4.3.2 The observation of cavitation damage for CB8 steel

A set of 3D cavity data for CB8 (10.86% Cr) at rupture under different stresses of 120-180MPa are available, as experimental data produced by X-ray microtomography. Gupta et al. (2013, 2015) reported the synchrotron microtomography could realise this with steels with high absorption to X-ray. The special SR-μCT can make imaging in

3D of cavities directly. A scanned sample of CB8 steel is shown in Figure 4.8. The variation of overall number density, volume fraction and void size with different stresses are shown in Figure 4.9. The reason for choosing this data is that there has been shown to be a relationship between the density and number of rupture times under different stresses. This data is available and the necessary conditions to display the trend of cavity nucleation rate coefficient A_2 under different stresses is outlined in section 6.5. However, the above experimental data for P91 and E911 steels (section 4.3.1) is just published under an individual stress, not under several different stresses; this therefore for not satisfy the research in section 6.5.

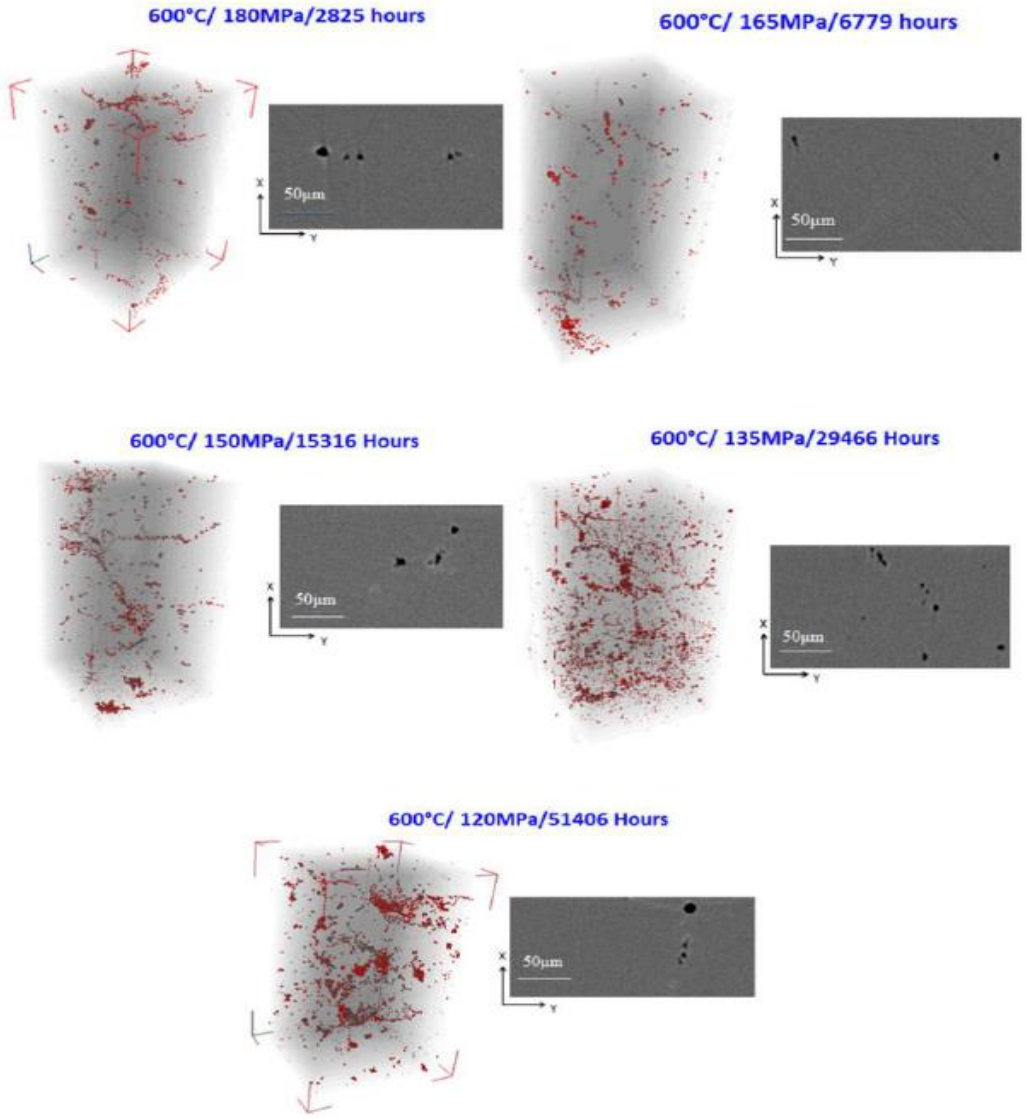

Figure 4.8 3D visualisation plots of microtomography data sets extracted from samples CB8 at 600°C in different stress range 120–180MPa, each data set extracted via a 2D slice (Gupta et al., 2015).

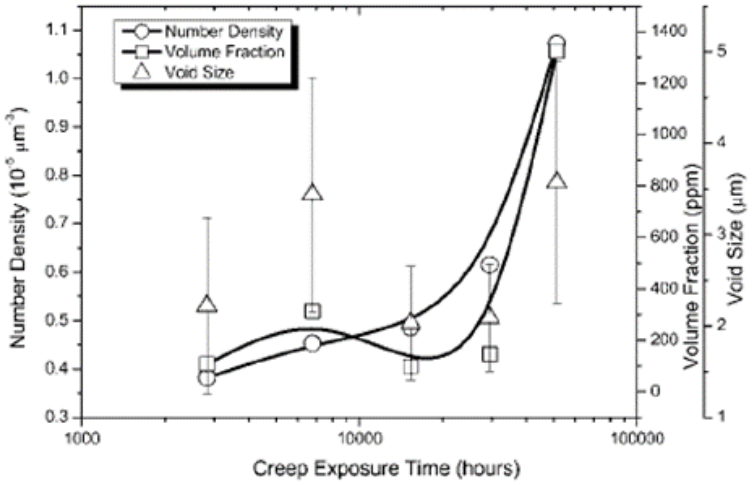

Figure 4.9 The variation of overall number density, volume fraction and void size with over stress levels from 120MPa to 180MPa at 600°C for CB8 steel (Gupta et al., 2013, 2015).

4.3.3 The observation of cavitation damage for MARBN steel

A set of 3D cavity data for MARBN-heat 1 cross welds (Martensitic Boron–Nitrogen strengthened steel) under different stress from 70 MPa to 130MPa are available. The cavity data used was obtained via synchrotron X-ray microtomography and Electron Backscatter Diffraction (EBSD) method. The creep tested samples, and 3D micro-CT image of creep tested cross welds are shown in Figure 4.10, and their density number is summarised in Table 4.2. The reason for choosing this data is that it is another data set that shows the relationship between the density and number of rupture times under different stresses. This data is available and the necessary conditions for it to display the trend of cavity nucleation rate coefficient A_2 under different stresses is outlined in section 6.5. The reason it has been chosen is the same as that above in section 4.3.2, but the above set data of CB8 steel is a study method case; this data set of MARBN steel is an application case.

Table 4.2 The density of cavities under different stress for MARBN (Schlacher et al., 2015)

Stress (MPa)	The density of cavities (10^{-5}um^{-3})
70	3.03
80	6.95
100	7.33
130	2.95

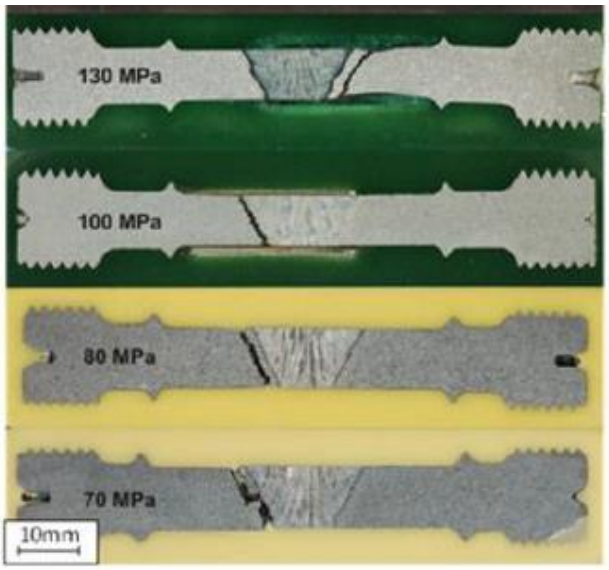

1)

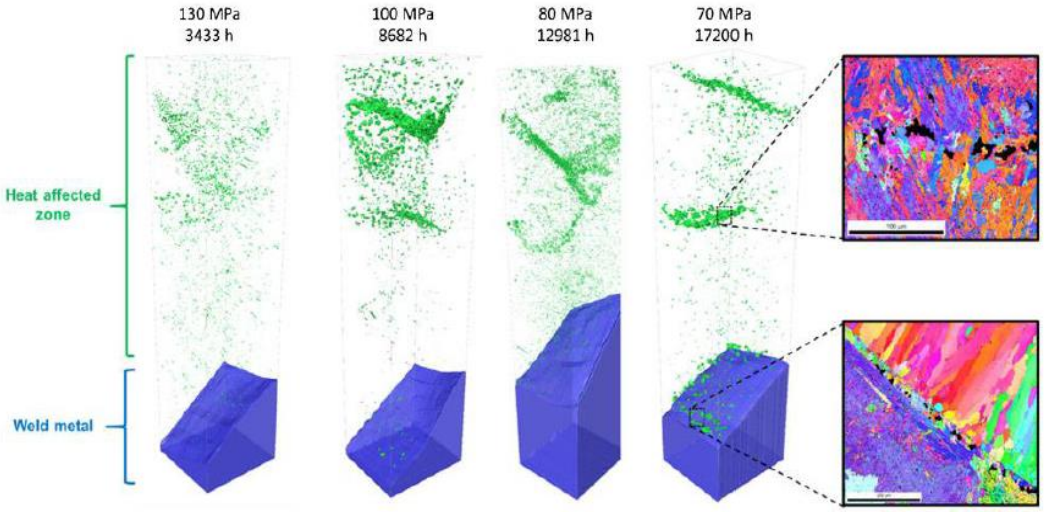

2)

Figure 4.10 1) samples; 2) 3D visualisation volume of microtomography data sets extracted from MARBN creep tested cross weld specimen in different stress ranges of 70–130MPa. EBSD maps of local regions (Schlacher et al., 2015; Gupta et al., 2015).

4.3.4 The observation of cavitation damage for 316H steel

There are two sets of creep test data for type-316H austenitic stainless steel, which experimental data is used by Small-Angle Neutron Scattering (SANS) techniques. A plastic 8% pre-strain controlled set of specimens, along with another group of samples that were not subjected to the pre-strain were collected under different stresses and temperatures. According to Jazaeri et al. (2019), the above two separate processes aimed to examine the effects of pre-strain on the creep damage formation and represent its current and future operation in the power plant. The creep test specimen is shown in Table 4.3, and each set of creep curves for creep test conditions and cavity size distribution are shown in Figure 4.11 and Figure 4.12. The reason for choosing this data

is that there has been shown to be a relationship between the number of cavity and radium, and also the data on time at different stages of creep lifetime, not only in the rupture time, has been published. This data is available and significant in the development and calibration of a creep cavitation model at different stages of creep lifetime and is outlined in Chapter 8. The applicated method is detailed in section 3.3.4. However, Sket et al. (2010) and Renversade et al. (2014) (section 4.3.1) did not produce and publish this relative experimental data, they just published data occurring at rupture time.

Table 4.3 The specimen ID number and creep strain under different conditions (Jazaeri et al., 2019).

Condition	Temperature (°C)	Stress (MPa)	ID number	Creep strain (%)
after 8% pre-strain	550	320	5d1	0
			9d1	0.54
			10d1	1.05
			6d1	2.34
			2d1	4.21
			3d1	6.77 (rupture)
no pre-strain	675	150	14d1	3.3
			13d1	5.7
			12d1	14.8
			11d1	47.5 (rupture)

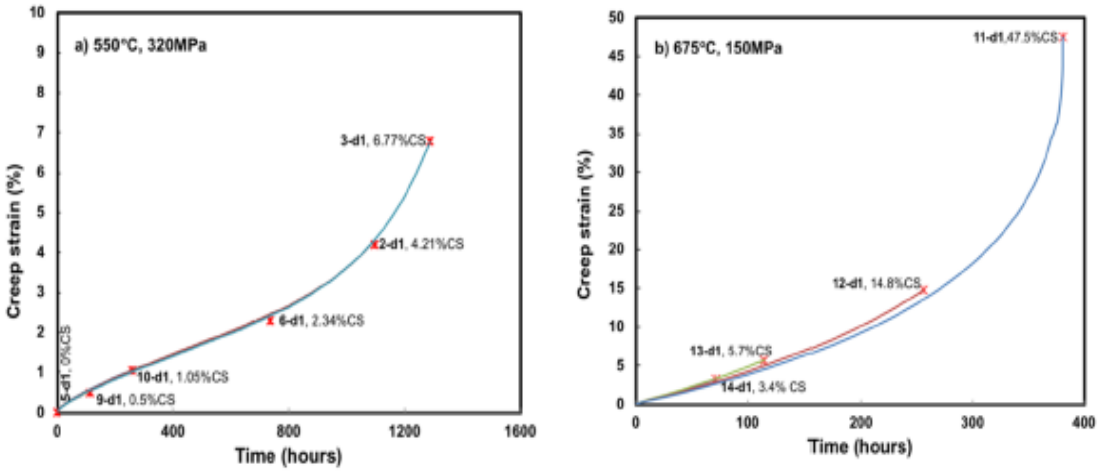

Figure 4.11 Creep curves for creep test conditions: a) 550°C under 320MPa (after 8% pre-strain); b) 675°C under 150MPa (no pre-strain) (Jazaeri et al., 2019).

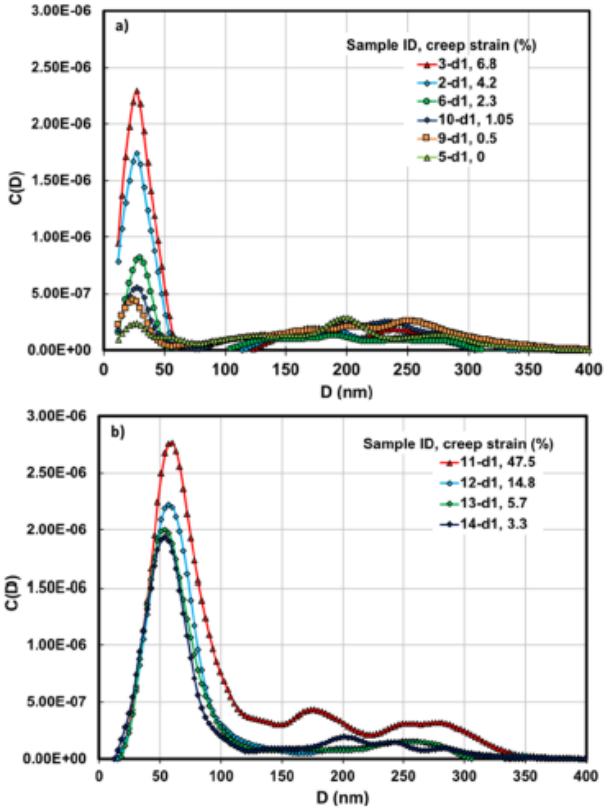

Figure 4.12 Cavity size distribution: a) 550°C under 320MPa (after 8% pre-strain); b) 675°C under 150MPa (no pre-strain) (Jazaeri et al., 2019).

4.3.5 The observation of cavitation damage for P92 steel

There is one set of experimental data referenced from Panait's thesis (2010a) in which data is provided by SZMF, Germany. It has been summarised and shown in the Appendix (Tables 9 and 10). This data is used to describe the deficiencies of the classical constitutive equations and to apply a "novel hyperbolic sine law" for discussing the relationship between minimum strain rate and different stresses, of which detailed information is supplied in section 5.2.

For the verification of the science and rationality for the author's results, there is another set of experimental data extracted by reading the published graph under various applied stress levels at 600°C and 650°C for P92 steels by Yin et al. (2006). The graphs from this are displayed in Figures 4.13 and 4.14, respectively. This is the reason for choosing this data. Figure 4.13 shows the relationship between the strain and time to calculate the relationship between the minimum strain rate and time. This minimum strain rate occurs in the second creep stage in creep deformation and damage, the relevant data used in section 5.2. The data in Figure 4.14 was adopted in section 6.4 to calculate the value of coefficient *U'* under different stress levels.

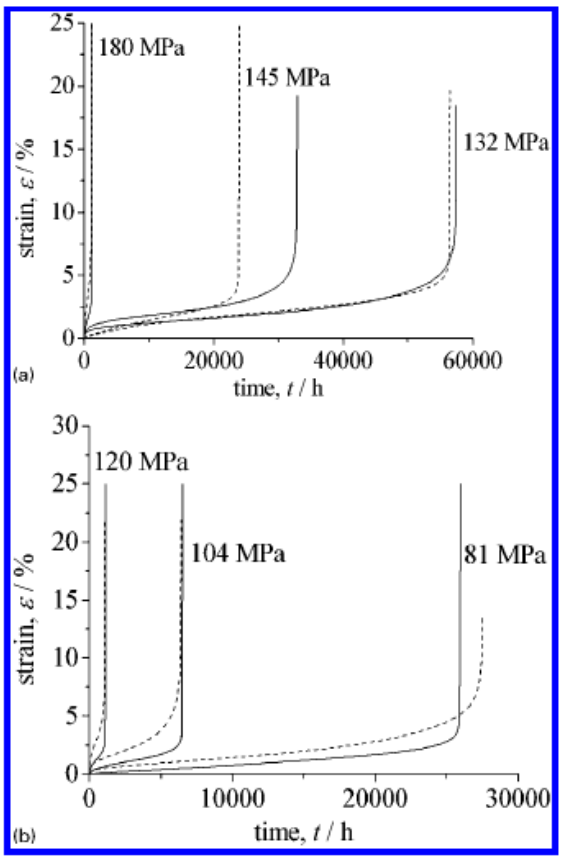

Figure 4.13 Examples of experimental data and CDM predicted creep curves for P92 steel present as broken and solid lines respectively under different stress: (a) 600°C; (b) 650°C (Yin et al., 2006).

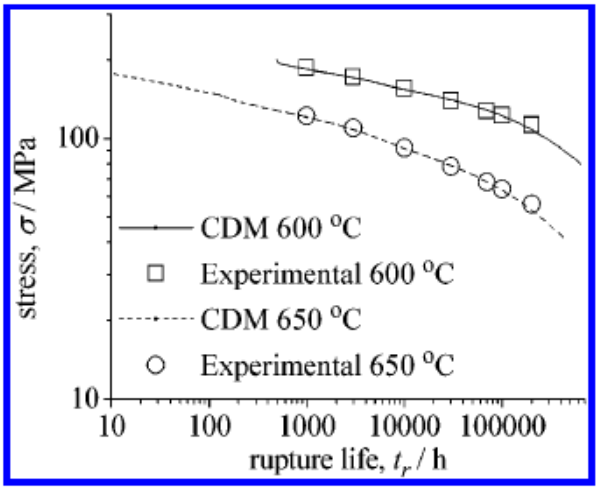

Figure 4.14 Experimental creep rupture data and CDM modelling lines (Yin et al., 2006).

4.4 Summary

This chapter has listed and summarised the collection of the experimental data for high Cr steel under different stresses and temperatures. It then outlines why the data was chosen and where they were utilised in the following chapters, which includes NIMS creep data and experimental observation data of cavitation damage. For example, the reason for choosing E911 steel is to show the relationship between the number of cavity and radium and the published rupture time. This data is available and the necessary conditions to apply and calculate a new cavitation damage equation is outlined in section 6.3. However, the NIMS data sheet (section 4.2.1 and section 4.2.2) cannot be produced and published for these relative experimental data. How to use this data to develop and then apply developed creep damage constitutive equations is outlined in the following relative chapters. This chapter cannot only build a good foundation for the next chapters but also aids in confidently developing creep damage constitutive equations based on the experimental data.

Chapter 5 Minimum creep strain rate and applied stress equation for high Cr steel over a wide range of stress

5.1 Introduction

The minimum creep strain rate and stress equation is critical in respect to the research of rupture criteria and creep deformation and damage. This chapter introduces the deficiencies of the classical constitutive equations which are used to describe the relationship between the minimum creep strain rate and stress. The chapter also presents the application of a novel minimum creep strain rate equation under a wide range of stress. The specific strategies to research the relationship between minimum creep strain rate and stress in order to achieve the application of the "novel hyperbolic sine law" can be demonstrated below:

(1) To investigate the deficiencies related to the existing functions.

(2) To apply a new minimum creep strain rate equation (Xu et al. 2017a) under a wide range of stress.

(3) To compare the predicted results with their experimental data.

The experimental data for this chapter includes:

(1) Creep test one: P91 (9Cr–1Mo–V–Nb), the temperature at 600°C, stress range from 70MPa to 200MPa, minimum creep strain rate between $1\times10^{-7}h^{-1}$and $1.5\times10^{-3}h^{-1}$ (NIMS, 2014).

(2) Creep test two: P92 (9Cr–1.8W–0.5Mo–V-Nb): 1) the temperature at 600℃, stress range from 120MPa to 180MPa, minimum creep strain rate between $3.7\times10^{-7}h^{-}1$ and $1.22\times10^{-5}h^{-1}$; 2) the temperature at 650℃, stress range from 70MPa to 140MPa, minimum creep strain rate between $7.9\times10^{-7}h^{-1}$ and $1.44\times10^{-4}h^{-1}$ (Panait, 2010a).

(3) Creep test three: ASME Grade 92 (9Cr–1.8W–0.5Mo–V-Nb) steel: 1) the temperature at 600℃, stress range from 120MPa to 250MPa, minimum creep strain rate between $1.81\times10^{-5}h^{-1}$ and $9.96\times10^{-1}h^{-1}$; 2) the temperature at 650℃, stress range from 50MPa to 160MPa, minimum creep rate between $1.5\times10^{-5}h^{-1}$ and $5.6\times10^{-1}h^{-1}$ (NIMS, 2018; Zheng et al., 2020).

5.2 Investigation of classical constitutive equations for minimum creep strain rate

The existing experimental data of minimum creep strain rate, and stress for P92 (9Cr–1.8W–0.5Mo–V-Nb) steel are summarised and shown in Figure 5.1. A part of the specific data about minimum creep strain rate for P92 (9Cr–1.8W–0.5Mo–V-Nb) steel was adopted from the NIMS (2018) creep data sheet with the remaining being based on Panait's thesis (2010a) whose experimental data was provided by Salzgitter Mannesmann Forschung GmbH (SZMF) (Panait, 2010a). The remaining portion of the relevant empirical data was extracted from the published graph.

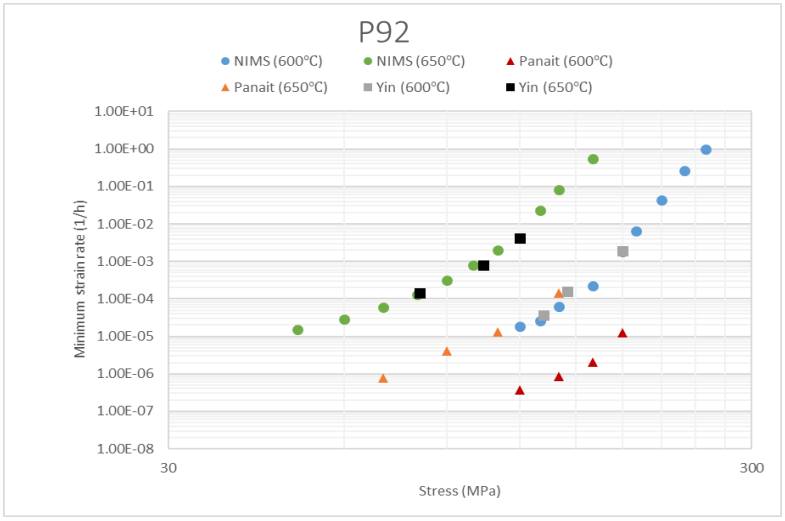

Figure 5.1 Experimental data of minimum creep strain rate and stress summarised at 600°C and 650°C for P92 steel (circle points referenced by NIMS (2018), triangle points referenced by Panait's thesis (2010a), square points referenced by Yin (2010a)) (Zheng et al., 2020).

The conventional minimum creep strain rate and street equations were summarised and proposed in Table 5.1 (Gorash, 2008). The power law and Norton power law are the same types, though they can be written in two forms. These are shown respectively as the current author referenced Panait's values (2010a) who had used the second form.

Table 5.1 The typical constitutive equations between minimum creep strain rate and stress (Gorash, 2008).

Power law (Norton, 1929)	$\dot{\varepsilon}_{min} = A\sigma^n$
or Norton power law (Panait, 2010a)	$\dot{\varepsilon}_{min} = A(\frac{\sigma}{\sigma_0})^n$
Linear+power law (Naumenko et al., 2007; Naumenko et al., 2009)	$\dot{\varepsilon}_{min} = A\sigma[1 + (B\sigma)^n]$
Hyperbolic sine law (Dyson et al., 1997; Dyson, 2000)	$\dot{\varepsilon}_{min} = Asinh(B\sigma)$

5.2.1 Investigation of power law

Power law usually assumes that the moving of crystal dislocations is formed by a systematic mode in a stress field and that the steady-state creep is controlled by the dislocation mechanism. The power law is widely used in the analysis of the property of many metals and heat resistant steels. Power law is often used in the high stress and over stress creep level, but Norton power law represents a steady-state creep. To reflect the relationship between the minimum creep strain rate and stress, some past research has been based on the Norton power law to study the steady-state creep, such as Panait (2010a) who adopted this law to discuss the stress exponent *n* at low and high stresses at 600℃ and 650℃ respectively. Displaying the deficiencies of the power law and Norton power law, a group of three sets of experimental data under different stress ranges were utilised in this investigation at 600°C for high Cr steel. The values of these material parameters are shown in Table 5.2. Another group was the two sets of experimental data under different stress ranges that were utilised in this investigation at 650°C for high Cr steel. The values of these material parameters are shown in Table 5.3.

Table 5.2 Material parameters based on power law and Norton power law at 600°C for high Cr steel.

	σ	A	n
P91 (power law) (Gorash, 2008)	<110MPa	$2.5\times10^{-9}MPa^{-1}h^{-1}$	1
	≥110MPa	$2.5\times10^{-31}MPa^{-1}h^{-1}$	12
P92 (Norton power law)	<160MPa	$1.19\times10^{-7}h^{-1}$	6
($\sigma_0 = 100\ MPa$) (Panait, 2010a)	≥160MPa	$5.18\times10^{-10}h^{-1}$	18
P92 (power law)		$1\times10^{-39}MPa^{-1}h^{-1}$	16.2

The values of material parameters for creep test one P91 steel were taken from Gorash's thesis (2008) who had adopted power law and distinguished low and high stress ranges from discussing the values of *A* and *n* respectively. The modelling result with the material parameters are reproduced and shown in Figure 5.2.1. The values of material parameters for creep test two P92 steel was referenced by Panait's thesis (2010a) who had used Norton power law and distinguished low and high stress range to research the values of *A* and *n* respectively. The modelling result with the material parameters reproduced are shown in Figure 5.2.2. The reason for using Norton power law is that Panait (2010a) used the experimental data under the steady-state creep condition. For creep test three P92 steel, the creep parameters *A* and *n* are unknown. The current author, which based the work on the power law, did not distinguish the stress range to calibrate the values of material parameters *A* and *n* at 600°C for P92 steel. The values can be displayed in the bottom set of data in Table 5.2, and the modelling result is shown in Figure 5.2.3.

1)

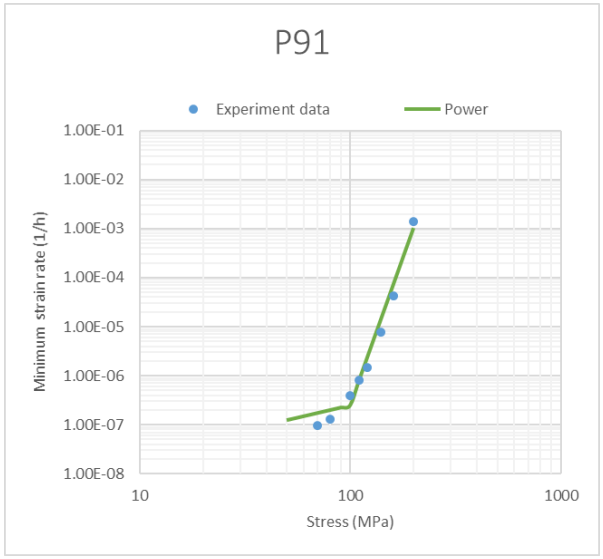

2)

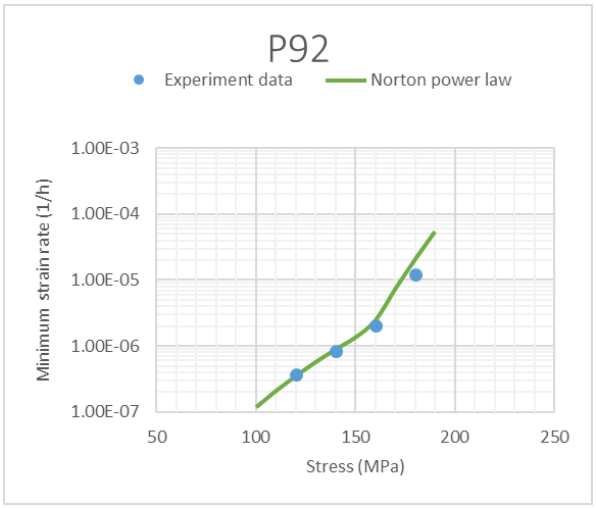

3)

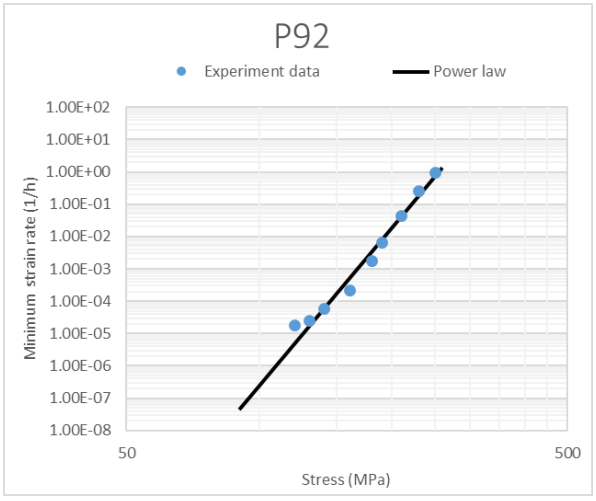

Figure 5.2 The modelling results compared with experimental data at 600 °C: 1) P91 is based on power law (Xu et al., 2017a; Gorash, 2008); 2) P92 is based on Norton power law (Panait, 2010a); 3) P92 is based on power law.

Figure 5.2 shows the comparison of the power law and Norton power law with their experimental data at 600°C for P91, P92 steels, respectively. Figure 5.2.1 reveals that the minimum creep strain rate predicted by the power law fit well with the experimental data under high stresses (≥110MPa). However, the minimum creep strain rate is higher than that of the experimental data at low pressures (<110MPa). As Figure 5.2.2 displays, the minimum creep strain rate predicted by the Norton power law is fitted well with the experimental data at low stresses (<160MPa). However, the minimum creep strain rate is higher than that of the experimental data at high stresses (≥160MPa). As Figure 5.2.3 indicates, the minimum creep strain rate predicted by the power law almost fits with their experimental data at high stresses. However, the minimum creep strain rate is lower than that of the experimental data at low stresses.

Table 5.3 Material parameters based on Norton power law and power law at 650°C for high Cr steel.

	σ	A	n
P92 (Norton power law)	≤110MPa	$9.78\times10^{-6}h^{-1}$	6
($\sigma_0 = 100\ MPa$) (Panait, 2010)	>110MPa	$1.07\times10^{-6}h^{-1}$	18
P92 (power law)		$8.8\times10^{-23}MPa^{-1}h^{-1}$	9.6

The values of material parameters for creep test two P92 steel was referenced by Panait's thesis (2010a) who used Norton power law and distinguished low and high stress ranges to research the values of *A* and *n* respectively. The modelling result with the material parameters reproduced and shown in Figure 5.3.1. The reason for using Norton power law is that Panait (2010a) used the experimental data under the steady-state creep condition. For creep test three P92 steel, the creep parameters *A* and *n* are unknown. The current author, who based the work on the power law, did not distinguish the stress range to calibrate the values of material parameters *A* and *n* at 650°C for P92 steel. The values are displayed in the bottom set of data in Table 5.3 and the modelling result is shown in Figure 5.3.2.

1)

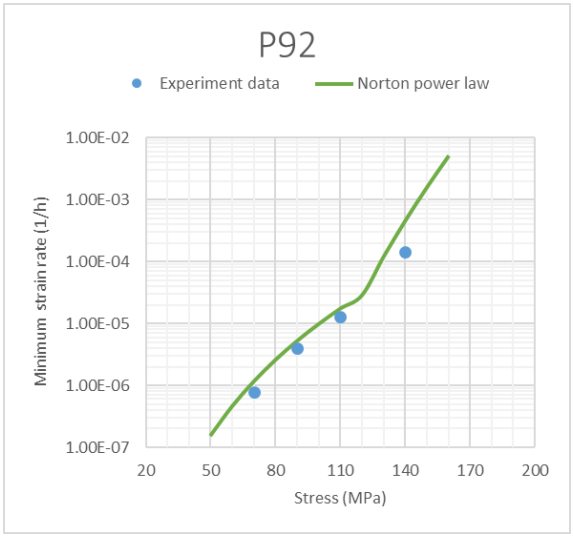

2)

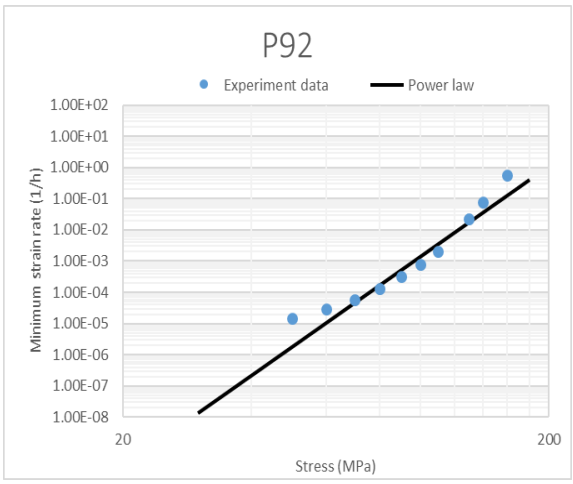

Figure 5.3 The modelling results compared with experimental data at 650°C: 1) P92 is based on Norton power law (Panait, 2010a); 2) P92 is based on power law.

Figure 5.3 shows the comparison of the Norton power law and power law with their experimental data at 650°C for P92 steel. As Figure 5.3.1 displays, the minimum creep strain rate predicted by the Norton power law is almost the same as the experimental data under low stress levels (≤110MPa). However, the minimum creep strain rate is higher than that of the experimental data at high stresses (>110MPa). As Figure 5.3.2 indicates, the minimum creep strain rate predicted by the power law almost fits with their experimental data at the intermediate stress level. However, the minimum creep strain rate is lower than that of the experimental data at low and high stresses.

5.2.2 Investigation of linear + power law

It is well-known that the diffusion and dislocation mechanism can control creep deformation during the intermediate stress level, and that the ground boundary sliding can also be inspected at this stress level. However, to decide which creep mechanism plays a significant factor is very difficult, the superimposition of diffusion and

dislocation mechanism can produce a transparent creep damage process to extend the power law, some research is based on the linear power law, such as Gorash (2008) who adopted this law to discuss the values of material parameters *A* and *B* at 600℃. According to Gorash (2008), this constitutive equation joins the power law with a diffusion mechanism. To display the deficiencies of the linear power law, two materials under different stress range were utilised in this investigation at 600°C for high Cr steel. The values of these material parameters are shown in Table 5.4.

Table 5.4 Material parameters based on linear power law at 600°C for high Cr steel.

	A ($MPa^{-1}h^{-1}$)	B (MPa^{-1})	n
P91 (linear power law) (Xu et al.,2017; Gorash, 2008)	2.5×10^{-9}	1×10^{-2}	11
P92 (linear power law)	1.5×10^{-9}	1×10^{-2}	16

The values of material parameters for creep test one P91 steel was taken from Gorash's thesis (2008) who adopted linear power law to discuss the values of *A*, *B* and *n*. A researcher of our current group subsequently reproduced and published the modelling result in a journal paper (Xu et al., 2017a). The modelling product with the material parameters, which are reproduced independently by the author, are shown in Figure 5.4.1. This process is reviewing and studying progress. For creep test three P92 steel, the creep parameters *A*, *B* and *n* are unknown. The current author based it on the linear power law to calibrate the values of material parameters *A*, *B* and *n* at 600°C for P92 steel. The values are displayed in the bottom set of data in Table 5.4, and the modelling result is shown in Figure 5.4.2.

1)

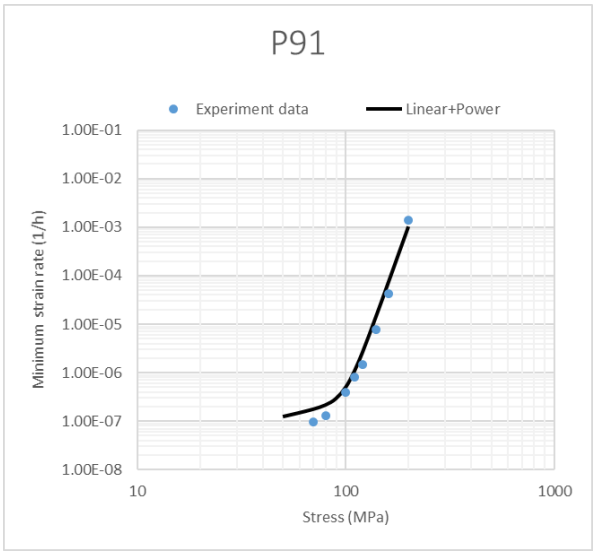

2)

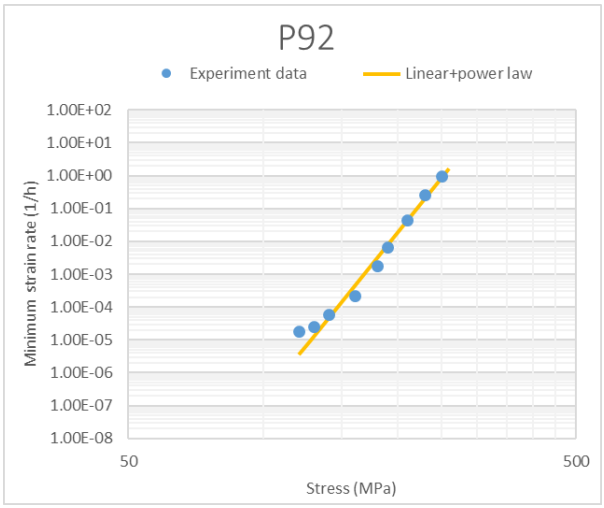

Figure 5.4 The predicted results of linear power law compared with their experimental data at 600°C: 1) P91 (Xu et al.,2017a; Gorash, 2008); 2) P92.

Figure 5.4 indicates the comparison of the linear power law with their experimental data at 600°C for P91 and P92 steels. As Figure 5.4.1 displays, the minimum creep strain rate produced by the linear power law is a good fit with the experimental data at high stresses. However, the minimum creep strain rate is higher than that of the experimental data at low stresses. As Figure 5.4.2 reveals, the minimum creep strain rate produced by the linear power law almost fits with the experimental data at the high stresses. However, the minimum creep strain rate is lower than that of the experimental data at low stresses.

5.2.3 Investigation of the hyperbolic sine law

According to this study, the climb and glide of dislocations control the grain boundary sliding rate within the grain. This rate is approximately a constant fraction of the total

creep strain rate. The dislocation mechanism is described by the power law relationship generally, but some researchers propose the climb and glide occur in parallel rather than as a sequential process such as in Dyson and Osgerby. These parallel processes cause the creep strain rate to have a hyperbolic sine with the applied stress, rather than the conventional power law. Gorash (2008) used the hyperbolic sine law to investigate the values of material parameters *A* and *B* at 600℃ for P91 steel. To display the deficiencies of the conventional hyperbolic sine law, three sets of experimental data under different stress ranges were utilised in this investigation at 600°C for high Cr steel. The values of these material parameters are shown in Table 5.5. A further group was the two sets of experimental data under different stress ranges that were utilised in this investigation at 650°C for high Cr steel. The values of these material parameters are shown in Table 5.6.

Table 5.5 Material parameters based on conventional hyperbolic sine law at 600°C for high Cr steel.

	A (h^{-1})	B (MPa^{-1})
P91 (hyperbolic sine law) (Xu et al.,2017; Gorash, 2008)	4.5×10^{-8}	5×10^{-2}
P92 (hyperbolic sine law)	1×10^{-9}	5.4×10^{-2}
P92 (hyperbolic sine law)	1.4×10^{-9}	8.4×10^{-2}

The values of material parameters for creep test one P91 steel was taken from Gorash's thesis (2008), who adopted conventional hyperbolic sine law to discuss the values of *A* and *B*. A researcher of our research group subsequently reproduced and published the modelling result in a journal paper (Xu et al.,2017a). The modelling product with the material parameters are reproduced independently by the current author and are shown in Figure 5.5.1. This process is a review and study of progress. For creep test two P92 steel, the creep parameters *A* and *B* are unknown. The current author based on the conventional hyperbolic sine law calibrated the values of material parameters *A* and *B* for P92 steel. The modelling result is shown in Figure 5.5.2. For creep test three P92 steel, the creep parameters *A* and *B* are unknown. The author again based the conventional hyperbolic sine law to calibrate the values of material parameters *A* and *B* at 600°C for P92 steel. The values are displayed in the bottom set of data in Table 5.5, and the modelling result is shown in Figure 5.5.3.

1)

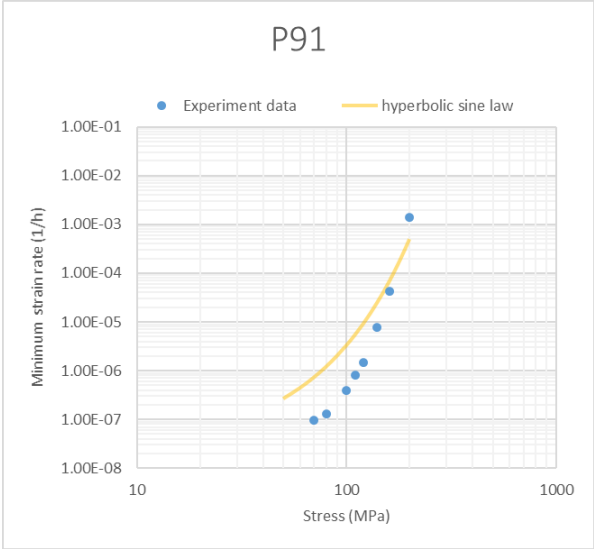

2)

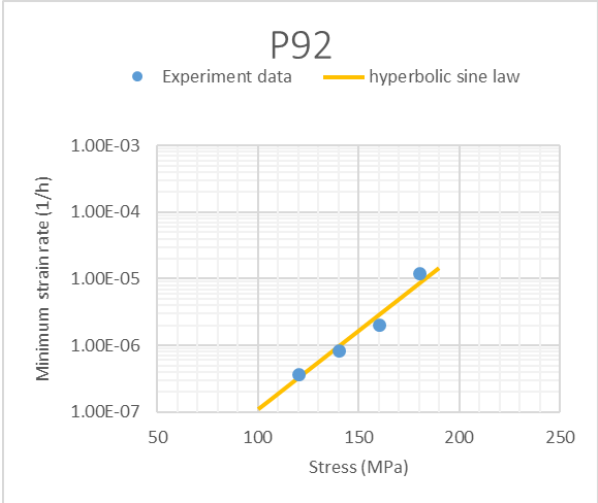

3)

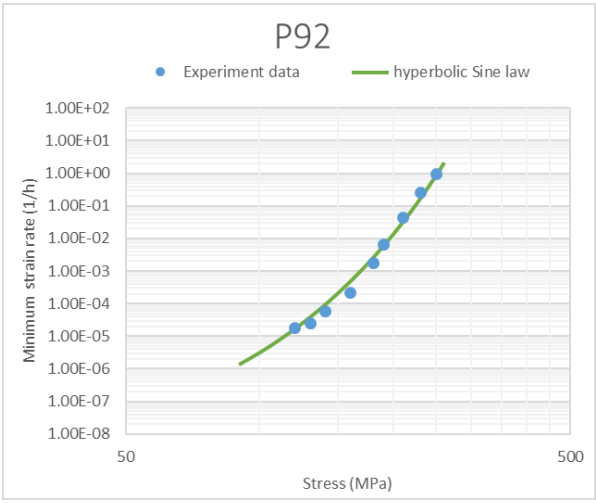

Figure 5.5 The predicted results of hyperbolic sine law compared with experimental data at 600°C: 1) P91 (Xu et al.,2017a; Gorash, 2008); 2) P92 (experimental data referenced by Panait's thesis (2010a)); 3) P92.

Figure 5.5 displays the comparison of conventional hyperbolic sine law with the experimental data at 600°C for P91 and P92 steels. As Figure 5.5.1 indicates, the minimum creep strain rate is produced by the hyperbolic sine law which fits the experimental data under high stress levels. However, the minimum creep strain rate is higher than that of the experimental data at low stresses. As Figure 5.5.2 reveals, the minimum creep strain rate produced by hyperbolic sine law almost fits with the experimental data at a low stress range. However, the minimum creep strain rate is lower than that of the experimental data at high stresses. As Figure 5.5.3 displays, the minimum creep strain rate is produced by hyperbolic sine law which fits with the experimental data at an over stress range. However, the minimum creep strain rate is higher than that of the experimental data at the intermediate stress level.

Table 5.6 Material parameters based on conventional hyperbolic law at 650°C for high Cr steel.

	A (h^{-1})	B (MPa^{-1})
P92 (hyperbolic sine law)	5×10^{-9}	8×10^{-2}
P92 (hyperbolic sine law)	1.4×10^{-7}	9.6×10^{-2}

For creep test two P92 steel, the creep parameters *A* and *B* are unknown. The current author based the work on the conventional hyperbolic sine law to calibrate the values of material parameters *A* and *B* for P92 steel. The modelling result is shown in Figure 5.6.1. For creep test three P92 steel, the creep parameters *A* and *B* are unknown. The author again used the conventional hyperbolic sine law to calibrate the values of material parameters *A* and *B* at 650°C for P92 steel. The values are displayed in the bottom set of data in Table 5.6, and the modelling result is shown in Figure 5.6.2.

1)

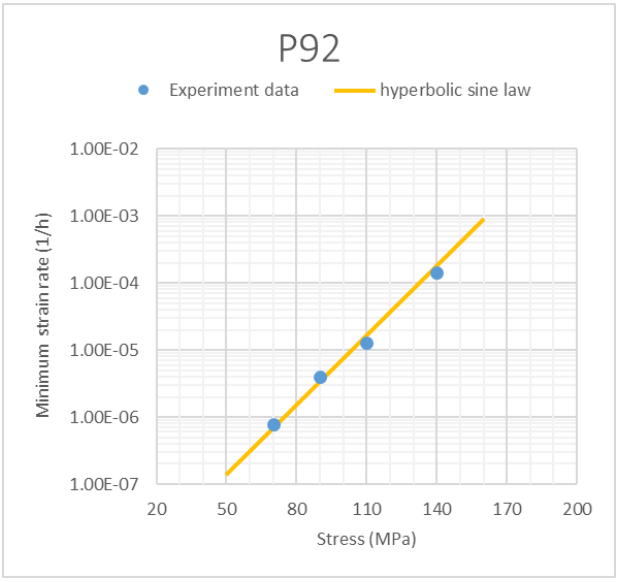

2)

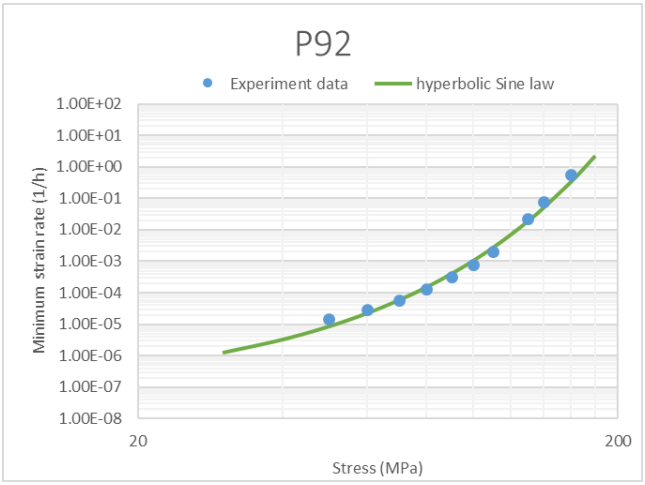

Figure 5.6 The predicted results of hyperbolic sine law compared with their experimental data at 650°C: 1) P92 (experimental data referenced by Panait's thesis (2010a)); 2) P92.

Figure 5.6 displays the comparison of conventional hyperbolic sine law with their experimental data at 650°C for P92 steel. As Figure 5.6.1 reveals, the minimum creep strain rate is produced by hyperbolic sine law which almost fits with the experimental data at a low stress range. However, the minimum creep strain rate is higher than that of the experimental data at high stress levels. As Figure 5.6.2 reveals, the minimum creep strain rate produced by hyperbolic sine law almost fits with the experimental data at intermediate stress level. However, the minimum creep strain rate is lower than that of the experimental data at the ends of low and high stresses.

5.3 Applied a novel minimum creep strain rate equation

According to the investigation of the classical constitutive equations for minimum creep strain rate, the hyperbolic sine law has indicated an almost fit with their

experimental data at over stress range. However, the minimum creep strain rate is higher than that of the experimental data at intermediate stress level at 600°C for P92 steel. The hyperbolic sine law displayed a good fit with its experimental data at intermediate stress level. However, the minimum creep strain rate is lower than that of the experiment data at the ends of low and high stresses at 650°C for P92 steel. Xu et al. (2007a) propose that this phenomenon may be due to lacking consideration of the breaking mechanisms of change; this mechanism affects microstructural changes at different stress level (Zheng et al., 2020). Thus, the characteristic of the novel minimum creep strain rate equation is to weaken the effects of stress level on the minimum creep strain rate.

A "novel hyperbolic sine law" has reported by Xu et al. (2017a) and applied in Xu (2016), Xu et al., (2017a) and Zheng et al., (2020) where it is given in Equation 5.1:

$$\dot{\varepsilon}_{min} = A \sinh(B\sigma^q) \tag{5.1}$$

where A and B are material parameters, and q is stress exponent.

The "novel hyperbolic sine law" was successfully applied to either low or high Cr steels. The materials and their parameters are listed in Table 5.7.

Table 5.7 Materials and parameters (Zheng et al., 2020).

Material	Parameters A (h^{-1})	Parameters B (MPa^{-1})	q
0·5Cr–0·5Mo–0·25 V	4.12×10^{-8}	2.51×10^{-4}	2
2·25Cr–1Mo	5.57×10^{-7}	2.4×10^{-4}	2
P91	6.1×10^{-7}	2.14×10^{-4}	2

Application of the "novel hyperbolic sine law" and three sets of experimental data under different stress ranges are utilised in this investigation at 600°C for high Cr steel. The values of these material parameters are shown in Table 5.8. Another group is the two sets of experimental data under different stress range that were utilized in this investigation at 650°C for high Cr steels. The values of these material parameters are shown in Table 5.9.

Table 5.8 Material parameters based on the "novel hyperbolic sine law" at 600°C under 50-200MPa for P91 steel, and under 90-260MPa for P92 steel.

	A (h^{-1})	B (MPa^{-1})	q
P91 (novel hyperbolic sine law)	6.5×10^{-8}	2.7×10^{-4}	2
P92 (novel hyperbolic sine law)	3.65×10^{-8}	1.96×10^{-4}	2
P92 (novel hyperbolic sine law)	1.12×10^{-6}	2.47×10^{-4}	2

The current author calibrated the values of material parameters for creep test one P91 steel, and the modelling result was reproduced independently by the author and shown in Figure 5.7.1. This process is reviewing and studying progress. For creep test two P92,

the creep parameters *A, B* and *q* are unknown. The author again based the "novel hyperbolic sine law" to calibrate the values of material parameters *A, B* and *q* for P92 steel. The modelling result is displayed in Figure 5.7.2. For creep test three P92, the creep parameters *A, B* and *q* are unknown. The author again based the "novel hyperbolic sine law" to calibrate the values of material parameters *A, B* and *q* at 600°C for P92 steel. The values are displayed in the bottom set of data in Table 5.8, and the modelling result are shown in Figure 5.7.3.

1)

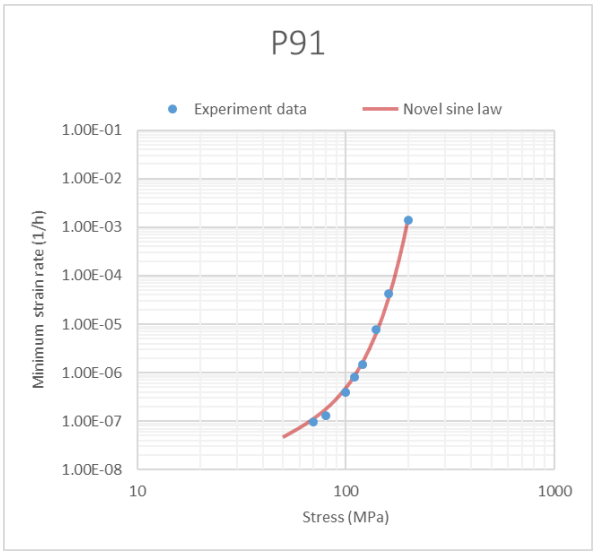

2)

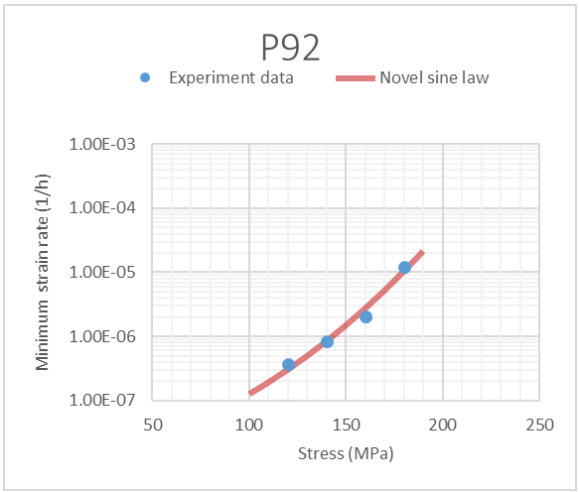

3)

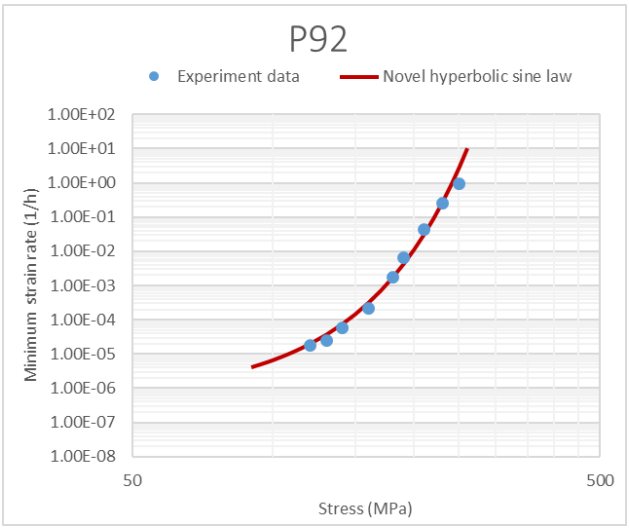

Figure 5.7 The modelling results of the “novel hyperbolic sine law” compared with their experimental data at 600°C: 1) P91 (Xu et al., 2017; Gorash, 2008); 2) P92 (experimental data referenced by Panait’s thesis (2010a)); 3) P92.

Figure 5.7 shows the comparison of the "novel hyperbolic sine law" with their experimental data at 600°C for P91 and P92 steels. As Figure 5.7.1 indicates, the minimum creep strain rate is produced by the "novel hyperbolic sine law" which fits well with the experimental data over stresses. As Figure 5.7.2 displays, the minimum creep strain rate is expected by the "novel hyperbolic sine law" which is a good fit with the experimental data at a limited stress range. Figure 5.7.3 reveals the minimum creep strain rate is made by the "novel hyperbolic sine law" which fits well with the experimental data at over stress range, and as a result, a favourable agreement was an achievement.

Table 5.9 Material parameters based on the "novel hyperbolic sine law" at 650°C under 30-180MPa for high Cr steel.

	A (h^{-1})	B (MPa^{-1})	q
P92 (novel hyperbolic sine law)	3.2×10^{-7}	3.58×10^{-4}	2
P92 (novel hyperbolic sine law)	1×10^{-5}	4.95×10^{-4}	2

For creep test two P92 steel, the creep parameters *A*, *B* and *n* are unknown. The current author based the "novel hyperbolic sine law" to calibrate the values of material parameters *A*, *B* and *n* for P92 steel. The modelling result is shown in Figure 5.8.1. For creep test three P92 steel, the creep parameters *A*, *B* and *n* are unknown. The author again based the "novel hyperbolic sine law" to calibrate the values of material parameters *A*, *B* and *n* at 650°C for P92 steel. The values are displayed in the bottom set of data in Table 5.9, and the modelling result are shown in Figure 5.8.2.

1)

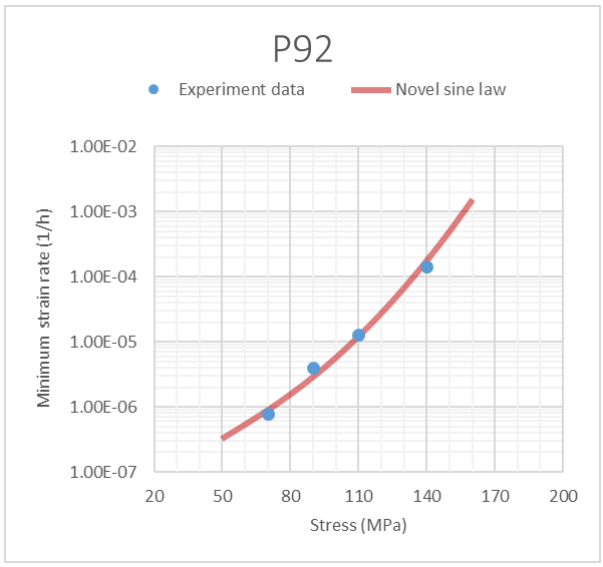

2)

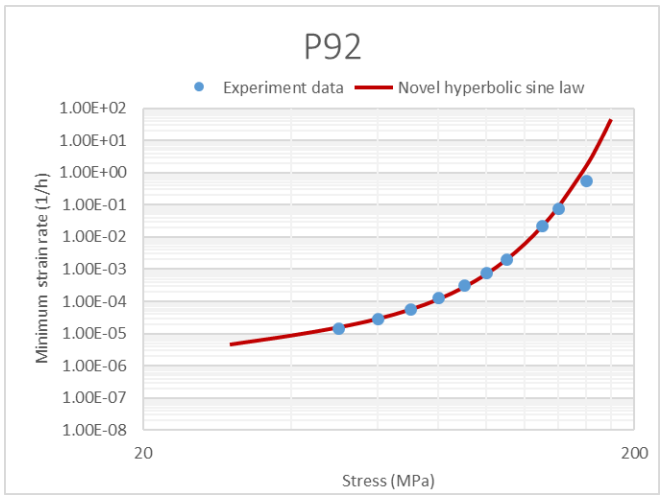

Figure 5.8. The modelling results of "novel hyperbolic sine law" compared with their experimental data at 650°C: 1) P92 (experimental data referenced by Panait's thesis (2010a)); 2) P92.

Figure 5.8 shows the comparison of "novel hyperbolic sine law" with their experimental data at 650°C for P92 steel. As Figure 5.8.1 indicates, the minimum creep strain rate is made by the "novel hyperbolic sine law" which is a good fit with the experimental data at a limited stress range. As Figure 5.8.2 reveals, the minimum creep strain rate is produced by the "novel hyperbolic sine law" which fits well with the experimental data over a wide range of stress, and as a result, a favourable agreement was an achievement.

5.4 Comparison and discussion of predicted results of different functions with experimental data

5.4.1 Comparison and discussion of predicted results of different functions with experimental data for P91 steel

For creep test one P91 steel, the calibrated material parameters are indicated in Table 5.10. The modelling results produced by a conventional power law, linear power law, sine law and the "novel hyperbolic sine law" are shown in Figure 5.9.

Table 5.10 The functions of minimum creep strain rate with calibrated material parameters at 600°C for P91 steel.

	A	B	n	q	σ
Power law (Xu et al.,2017a; Gorash, 2008)	2.5×10^{-9} $MPa^{-1}h^{-1}$		1		<110MPa
	2.5×10^{-31} $MPa^{-1}h^{-1}$		12		≥110MPa
Linear+Power law (Xu et al.,2017a; Gorash, 2008)	2.5×10^{-9} $MPa^{-1}h^{-1}$	1×10^{-2} MPa^{-1}	11		
Hyperbolic sine law (Xu et al.,2017a; Gorash, 2008)	4.5×10^{-8} h^{-1}	5×10^{-2} MPa^{-1}			
Novel hyperbolic sine law	6.5×10^{-8} h^{-1}	2.7×10^{-4} MPa^{-1}		2	

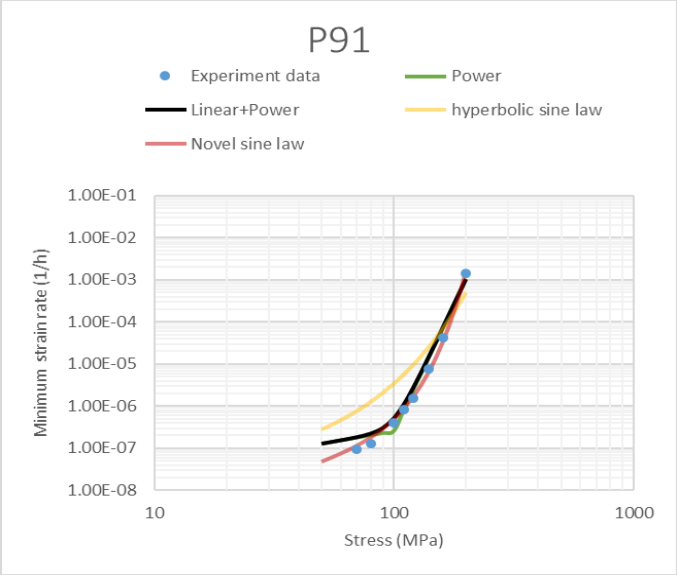

Figure 5.9 The comparison between the different functions of minimum creep strain rate and applied stress at 600°C for P91 steel.

Figure 5.9 displays the comparison of the above four functions, and as can be seen, the curve of prediction by "novel hyperbolic sine law" fits very well with the experimental data and as a result, a favourable agreement was achieved.

5.4.2 Comparison and discussion of predicted results of different functions with experimental data for P92 steel (experimental data referenced by Panait's thesis (2010a))

For creep test two P92 steel at 600°C, the calibrated material parameters are displayed in Table 5.11. The modelling results produced by a Norton power law, hyperbolic sine law and the "novel hyperbolic sine law" are indicated in Figure 5.10.

Table 5.11 The functions of minimum creep strain rate with calibrated material parameters at 600°C for P92 steel (experimental data referenced by Panait's thesis (2010a)).

	A (h^{-1})	B (MPa^{-1})	n	q	σ (MPa)
Norton power law (Panait, 2010a)	1.19×10^{-7}		6		<160
	5.18×10^{-10}		18		≥160
Hyperbolic sine law	1×10^{-9}	5.4×10^{-2}			
Novel hyperbolic sine law	3.65×10^{-8}	1.96×10^{-4}		2	

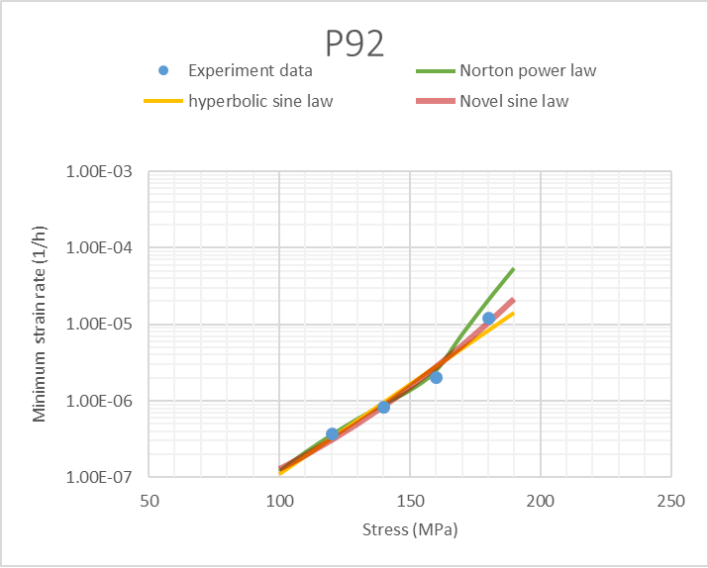

Figure 5.10 The comparison between the different functions of minimum creep strain rate and applied stress at 600°C for P92 steel (experimental data referenced by Panait's thesis (2010a)).

Figure 5.10 shows the comparison of the above three functions, which as can be seen,

the curve of prediction by "novel hyperbolic sine law" fits very well with experimental data and therefore achieves a favourable agreement.

For creep test two P92 steel at 650°C, the calibrated material parameters are summarised in Table 5.12. The modelling results produced by a Norton power law, conventional hyperbolic sine law and the "novel hyperbolic sine law" are given in Figure 5.11.

Table 5.12 The functions of minimum creep strain rate with calibrated material parameters at 650°C for P92 steel (experimental data referenced by Panait's thesis (2010a)).

	A (h^{-1})	B (MPa^{-1})	n	q	σ (MPa)
Norton power law (Panait, 2010a)	9.78×10^{-6}		6		≤110
	1.07×10^{-6}		18		>110
Hyperbolic sine law	5×10^{-9}	8×10^{-2}			
Novel hyperbolic sine law	3.2×10^{-7}	3.58×10^{-4}		2	

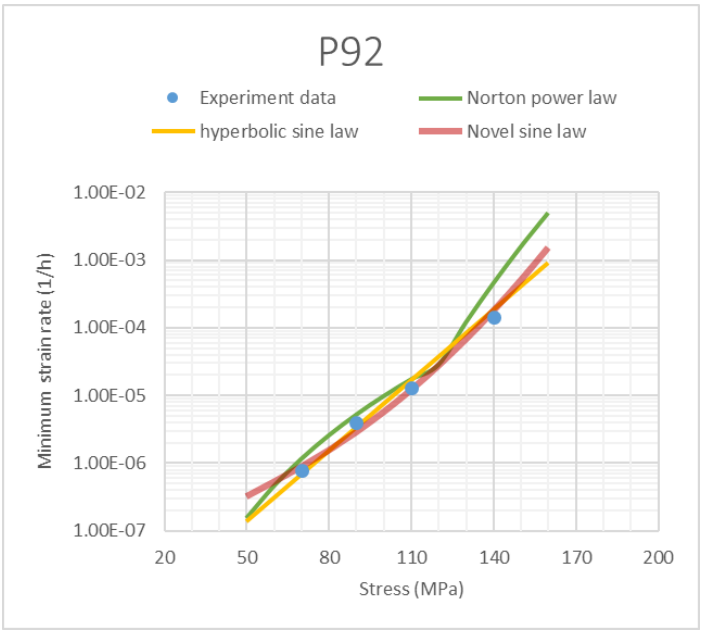

Figure 5.11 The comparison between the different functions of minimum creep strain rate and applied stress at 650°C for P92 steel (experimental data referenced by Panait's thesis (2010a)).

Figure 5.11 shows the comparison of the above three functions, which as can be seen, the curve of prediction by "novel hyperbolic sine law" fits very well with its experimental data and therefore achieves a favourable agreement.

5.4.3 Comparison and discussion of predicted results of different functions with experimental data for P92 steel

For creep test three P92 steel at 600°C, the calibrated material parameters are displayed in Table 5.13. The modelling results produced by a power law, linear power law, conventional hyperbolic sine law and the "novel hyperbolic sine law" are indicated in Figure 5.12.

Table 5.13 The functions of minimum creep strain rate with calibrated material parameters at 600°C for P92 steel (Zheng et al., 2020).

	A	B	n	q
Power law	1×10^{-39} $MPa^{-1}h^{-1}$		16.2	
Linear+Power law	1.5×10^{-9} $MPa^{-1}h^{-1}$	1×10^{-2} MPa^{-1}	16	
Hyperbolic sine law	1.4×10^{-9} h^{-1}	8.4×10^{-2} MPa^{-1}		
Novel hyperbolic sine law	1.12×10^{-6} h^{-1}	2.47×10^{-4} MPa^{-1}		2

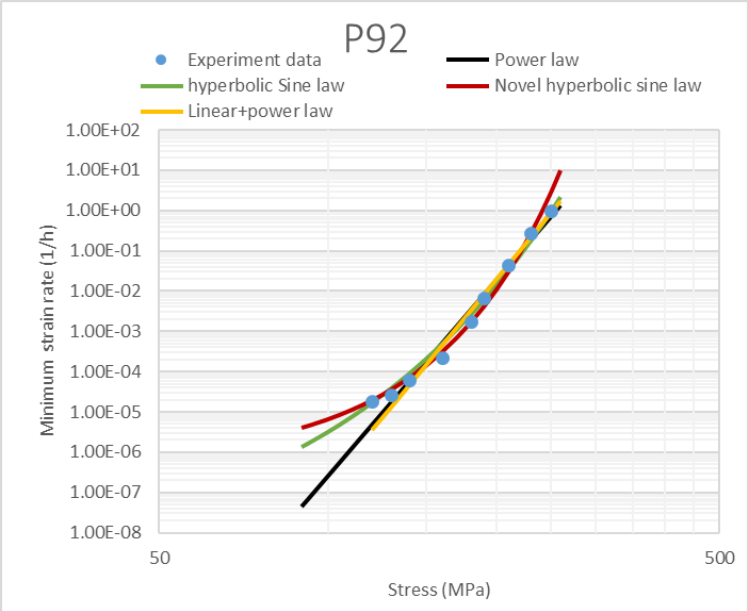

Figure 5.12 The comparison between the different functions for minimum creep strain rate and applied stress at 600°C for P92 steel (Zheng et al., 2020).

Figure 5.12 shows the comparison of the above four functions, which as can be seen, the curve of prediction by "novel hyperbolic sine law" fits very well with experimental data and therefore achieves a favourable agreement.

For creep test three P92 steel at 650°C, the calibrated material parameters are summarised in Table 5.14. The modelling results predicted by a power law,

conventional hyperbolic sine law and the "novel hyperbolic sine law" are displayed in Figure 5.13.

Table 5.14 The functions of minimum creep strain rate with calibrated material parameters at 650°C for P92 steel (Zheng et al., 2020).

	A	B	n	q
Power law	8.8×10^{-23} $MPa^{-1}h^{-1}$		9.6	
Hyperbolic sine law	1.4×10^{-7} h^{-1}	9.6×10^{-2} MPa^{-1}		
Novel hyperbolic sine law	1×10^{-5} h^{-1}	4.95×10^{-4} MPa^{-1}		2

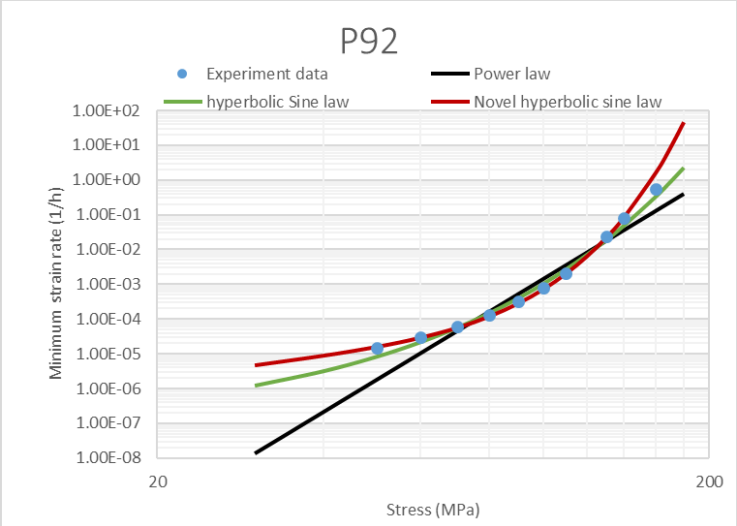

Figure 5.13 The comparison between the different functions for minimum creep strain rate and applied stress at 650°C for P92 steel (Zheng et al., 2020).

Figure 5.13 shows the comparison of the above three functions, which as can be seen, the curve of prediction by "novel hyperbolic sine law" fits very well with experimental data and therefore achieves a favourable agreement.

5.5 Summary

According to discussing the deficiencies of the classical constitutive equations, it is based on the three sets of experimental creep data, including power law, linear power law and hyperbolic sine law. The limitations of power law and linear power law cannot be fitted very well with its experimental data under a wide range of stress. Their stress needs to be divided into two or three stages to investigate them in these two equations. For the hyperbolic sine law, it also cannot fit very well with its experimental data under low stresses and medium stresses such as in Figure 5.12 and Figure 5.13. In other words, the degree of bending of the predicted curve is not enough in these curves. This disadvantage can be solved by adding an exponent "q" and so forming the "novel

hyperbolic sine law". The new development is that a "novel hyperbolic sine law" is successfully applied and calculated over a wide range of stress for P92 steel, such as at 600°C, 625°C and 650°C for P91 and P92 steels, respectively. The equation is the newest law, and the collected experimental data is in the widest stress range from NIMS data; hence, it is evidence that the "novel hyperbolic sine law" is the best adaptability.

Chapter 6 Creep cavitation damage equation and rupture for high Cr steel

6.1 Introduction

This chapter describes the application and calculation of a new cavitation damage equation based on the cavity area fraction along the grain boundary. This is the main objective of the chapter. The methodology for the calibration of the cavity nucleation and cavity growth models is based on the x-ray microtomography cavitation data. This method, which was reported by Xu et al. (2017a), was a successful development and application for P91 steel in a prediction of the creep lifetime model. This chapter is focused on the application of such methodology to the other materials, for example, E911, P92 and MARBN, to which the x-ray microtomography cavitation data has been available. To achieve and evidence their viability, the current author understands the methodology and repeats the research on them for P91 and CB8 individually. Thus, this chapter also includes the author studying and repeating results produced by Xu et al. (2017a).

The process for this chapter is summarised as five parts:

(1) To understand the basic theory of cavitation damage functions.

(2) To research and know the methodology of application concerning a new cavitation damage equation for P91 steel at rupture time and to summarise the existing approach and to develop a new way to determine the material constants.

(3) Based on the appropriate methodology to calibrate the cavitation damage curve for E911 accordingly to set a new way to determine the values of five material constants.

(4) Based on the NIMS experimental data under different stress and different temperatures at creep rupture time for P91 and P92 steels to calculate the value of material coefficient U' in the cavity area fraction equation and discuss its relationship with stresses.

(5) To apply the published number of cavity density under different stress for high Cr steel (namely CB8 and MARBN) and to discuss and display the trend of cavity nucleation rate coefficient A_2 with stress.

The experimental data for this chapter includes:

(1) P91 (9Cr–1Mo–V–Nb) steel: the temperature at 575°C, creep time at 1.02×10^4h, the minimum and maximum cavity diameter of 1.2μm and 4.8μm at rupture

time (Renversade et al., 2014).

(2) E911 steel: the temperature at 600°C, creep time at 3.78×10^4h, the minimum and maximum cavity diameter of 1.2μm and 9.5μm at rupture time (Renversade et al., 2014; Xu et al., 2018b; Zheng et al., 2020).

(3) P91 (9Cr–1Mo–V–Nb) steel: the temperature at 600°C, stress range from 70MPa to 160MPa, lifetime from 9.71×10^2h to 8.0736×10^4h; the temperature at 625°C, stress range from 90MPa to 140MPa, lifetime from 9.9×10^1h to 2.1372×10^4h (NIMS, 2014).

(4) ASME Grade 92 (9Cr–1.8W–0.5Mo–V-Nb) steels: 1) the temperature at 600°C, stress range from 120MPa to 250MPa, lifetime from 5.1 h to 6.53634×10^4 h; the temperature at 625°C, stress range from 100MPa to 160MPa, lifetime from 2.134×10^2h to 3.35185×10^4h; the temperature at 650°C, stress range from 60MPa to 160MPa, lifetime from 1.05×10^1h to 9.28452×10^4h (NIMS, 2018); 2) the temperature at 600°C, stress range from 110MPa to 185MPa, lifetime from 1×10^3h to 2×10^5h; the temperature at 650°C, stress range from 60MPa to 115MPa, lifetime from 1×10^3h to 2×10^5h, according to that reported in Yin et al. (2006) (Xu et al., 2018b; Zheng et al., 2020).

(5) CB8 (10.86%Cr): the temperature at 600°C, stress range from 120MPa to 180MPa, lifetime from 2.8×10^3h to 5.1406×10^4h, cavity number density between 3.75×10^{-6}um^{-3} and 1.0625×10^{-5}um^{-3} (Gupta et al., 2013; Gupta et al., 2015).

(6) MARBN-heat 1 cross-welds (Martensitic Boron–Nitrogen strengthened steel): the temperature at 650°C, stress range from 70MPa to 130MPa, lifetime from 3.433×10^3h to 1.72×10^4h, cavity number density between 2.95×10^{-5}um^{-3} and 3.03×10^{-5}um^{-3} (Schlacher, 2015; Zheng et al., 2020).

6.2 Function for cavity area fraction and the cavity size distribution

Riedel (1987) present the generic theory of cavity area fraction along the grain boundary. The function of cavity size distribution is shown in Equation 6.1.a. Some authors developed and applied it in their work such as Xu et al. (2017a), Renversade et al. (2014), and Sket et al. (2010):

$$N(R,t)=\frac{A_2}{A_1}R^{\beta}t^{\alpha+\gamma}\left(1-\frac{1-\alpha}{1+\beta}\frac{R^{\beta+1}}{A_1t^{1-\alpha}}\right)^{(\alpha+\gamma)/(1-\alpha)} \quad (6.1.a)$$

where A_1, A_2, α, β, and γ are material constants, which depend on stress. $N(R,t)$ is the number of cavitation.

The growth rates of the cavity radius and nucleation rate are shown in Equation 6.2 and Equation 6.3 respectively (Xu et al., 2017a; Renversade et al., 2014; Riedel, 1987; Sket et al., 2010):

$$\dot{R} = A_1 R^{-\beta} t^{-\alpha} \tag{6.2}$$

$$J^* = A_2 t^{\gamma} \tag{6.3}$$

where the $\dot{R}$ is the non-stationary growth rate of the cavity radius, and J^* is the nucleation rate of the cavity.

The above Equations 6.2 and 6.3 can be used to calculate any experimental data for the cavity nucleation and cavity growth models theoretically. The function of cavity size distribution is a function about creep time when the cavity size distribution at creep rupture time t_f is shown as:

$$N(R, t_f) = \frac{A_2}{A_1} R^{\beta} {t_f}^{\alpha+\gamma} \left(1 - \frac{1-\alpha}{1+\beta} \frac{R^{\beta+1}}{A_1 {t_f}^{1-\alpha}}\right)^{(\alpha+\gamma)/(1-\alpha)} \tag{6.1.b}$$

where α, β, and γ can use for the determination of the parameter's values in the cavity nucleation and cavity growth models.

In this part, the values of α, β, and γ can be discussed and determined. The value of β is close to 2 in the literature (Xu et al., 2017a; Renversade et al., 2014; Riedel, 1987; Sket et al., 2010), which can agree with the constrained diffusional mechanism and controls cavity growth. Renversade et al. (2014) describes $\beta \approx 2.1 \pm 0.3$ for P91 and E911, while Sket et al. (2010) reports $\beta = 2$. In this chapter, the value of $\beta = 2$ is adopted. In the literature (Riedel, 1987; Sket et al., 2010), the exponent $(\alpha + \gamma)/(1 - \alpha) \approx 200$ and the value of α and γ suggests ≈ 1 in the actual case. When $\alpha = 1$, Equation 6.1.b rewrites to Equation 6.4.

$$N(R, t_f) = \frac{A_2}{A_1} R^{\beta} {t_f}^{1+\gamma} exp\left(-\frac{1+\gamma}{1+\beta} \frac{R^{\beta+1}}{A_1}\right) \tag{6.4}$$

The value of $\gamma = 1$ indicates the characteristic of the continuum cavity nucleation with cavity constrained growth (Xu et al., 2017a; Sket et al., 2010). Xu et al. (2017a) discussed and confirmed the value of γ by comparing the prediction shape with the experimental data for P91steel. When $\gamma = 1$, the Equation 6.4 rewrites to Equation 6.5.a.

$$N(R, t_f) = C_1 R^{\beta} exp\left(-\frac{C_2 R^{\beta+1}}{1+\beta}\right) \tag{6.5.a}$$

where C_1, C_2 is a material parameter, $C_1 = \frac{A_2}{A_1} {t_f}^{1+\gamma}$ and $C_2 = \frac{1+\gamma}{A_1}$.

The above Equation 6.5.a is declared in the literature and shown in Equation 6.5.b (Xu et al., 2017a; Sket et al., 2010):

$$f(R) = C_1 R^{\beta} exp\left(-\frac{C_2 R^{\beta+1}}{1+\beta}\right) \quad (6.5.b)$$

6.3 The calibration of cavity growth rate and nucleation rate models for P91 and E911 steels

The following part is compared to the prediction curve with the experimental data by confirming the values of $\alpha=1$, $\beta=2$, $\gamma=1$. It indicates that the actual experimental data is much denser, and only limited numbers can be obtained from the graph for comparison.

6.3.1 Determination of model constants for P91 steel

This part describes that the values of A_1, A_2, C and t_0 for the sample of P91 steel can be calculated, which is based on two different methods. The forward approach is summarised by the current author, which is based on Xu's published journal paper (Xu et al., 2017a). The second method has been independently devised by the current author to find numerical answers. The author individually researched the two methods for P91 steel based on the same experimental data and then successfully using the second method to another material for E911 steel.

6.3.1.1 The forward method

In this method, the time for the measurable minimum cavity size must be assumed by a series of trial and error methods. The process for this part of work is taken from Xu et al. (2017a, 2019) and Yang (2018):

Firstly, assuming the value of t_0, if t_0=41.367h, R_1=0.6μm and t_f=10200h, R_2=2.4μm, respectively.

Secondly, integrating the above Equation 6.2 produced:

$$\frac{1}{3}R^3 = A_1 lnt + C \quad (6.6)$$

Equation 6.6 twice, deleting C is shown as:

$$A_1 = \frac{R_2^3 - R_1^3}{3(lnt_f - lnt_0)} \quad (6.6.a)$$

with the values of t_0, R_1, t_f, and R_2 calculated the value of A_1=8.2358×10^{-1}μm^3/ln(h).

Thirdly, the above Equation 6.6 is used with the values of A_1, R_2, and t_f to calculate the value of C= -2.9938μm^3.

Finally, A_1 is substituted into the above Equation 6.4 with the leftmost point on the

histogram (R_1=0.6μm, $N(R_1, t_f)$ =3800) giving:

$$A_2 = \frac{N(R_1,t_f)A_1}{{R_1}^2 {t_f}^2 \exp(-2{R_1}^3/3A_1)} \quad (6.7.a)$$

or with the rightmost point on the histogram (R_2=*2.4μm, N* (R_2, t_f) =*1*) giving:

$$A_2 = \frac{N(R_2,t_f)A_1}{{R_2}^2 {t_f}^2 \exp(-2{R_2}^3/3A_1)} \quad (6.7.b)$$

the value of A_2=9.95×10^{-5}μm^{-3}h^{-2}.

Thus, the gradation of calculation is the value of t_0, A_1, C and A_2. In this method, only one point from the histogram is taken for the determination of the constants. It is reported that it is difficult to judge the best value for t_0 when it is around 41 hours, hence there is a small degree of inaccuracy and uncertainty. Figure 6.1 displays the prediction curve by using Equation 6.4, which fits well with the experimental data.

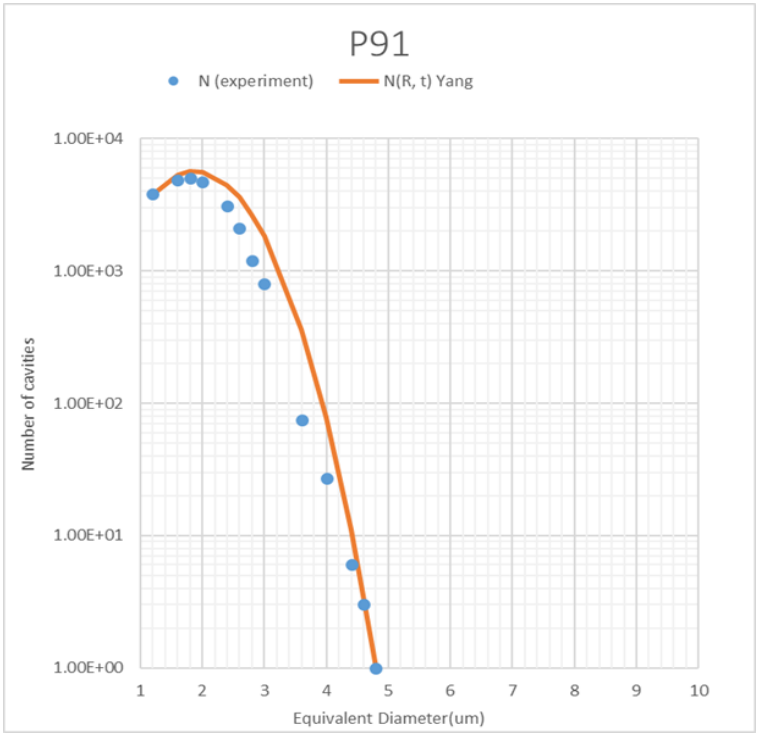

Figure 6.1 The probability density function of cavity equivalent radius for P91 steel by the forward method. Dots: experimental data from Renversade et al. (2014).

According to the values of t_0, A_1, C and A_2, the curve can be extended to include the condition of the minimum diameter. The time is occurring before t_0. The following Figure 6.2 displays the prediction curve, which includes the shape of the minimum diameter.

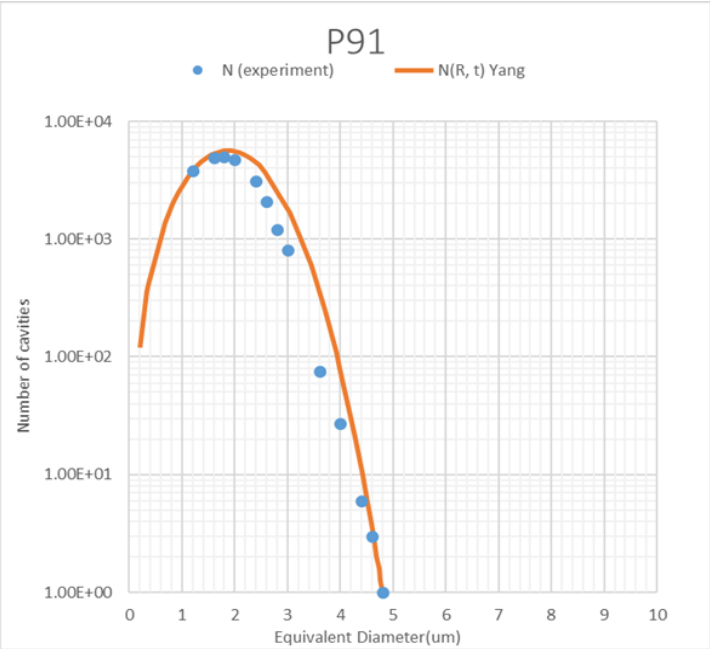

Figure 6.2 The prediction curve by the forward method for P91 steel, including the condition of the minimum diameter. Dots: experimental data from Renversade et al. (2014).

6.3.1.2 The second method

This method, which is called the backward method, is directly taken by two points from the histogram, and the values of A_1 and A_2 can be used to solve the two simultaneous in Equations 6.4. The process for this part of the work is from Zheng et al. (2020):

The first step is to choose the leftmost and rightmost points for calculation and illustration, it is t_f=10200h, respectively, R_1=0.6μm, $N(R_1, t_f)$ =3800 and R_2=2.4μm, $N(R_2, t_f)$ =1.

The second step is to use Equation 6.4 with above choosing two points; the equations concerning the values of A_1 and A_2, which are shown as:

$$A_1 = \frac{-2{R_1}^3+2{R_2}^3}{3Ln(N(R_1,t_f){R_2}^2/N(R_2,t_f){R_1}^2)} \tag{6.8}$$

$$A_2 = \frac{N(R_1,t_f)A_1}{{R_1}^2{t_f}^2\exp(-2{R_1}^3/3A_1)} \tag{6.7.a}$$

or

$$A_2 = \frac{N(R_2,t_f)A_1}{{R_2}^2{t_f}^2\exp(-2{R_2}^3/3A_1)} \tag{6.7.b}$$

The values of two points are substituted into Equation 6.8 to calculate the value of A_1= $8.2358\times10^{-1}\mu m^3/\ln(h)$ and Equation 6.7.a or Equation 6.7.b with the value of A_1 used to calculate the value of A_2= $9.95\times10^{-5}\mu m^{-3}h^{-2}$.

The third step is to use the integrating Equation 6.6 with the values of A_1, R_2, and t_f to calculate the value of C= -2.9938μm^3.

The final step is to use the integrating Equation 6.6 with the values of integration constant C, R_1 and A_1 to calculate the value of t_0=41.367h.

Thus, the gradation of calculation is the value of A_1, A_2, C and t_0. Figure 6.3 displays the prediction curve by using Equation 6.4 which fits well with the experimental data.

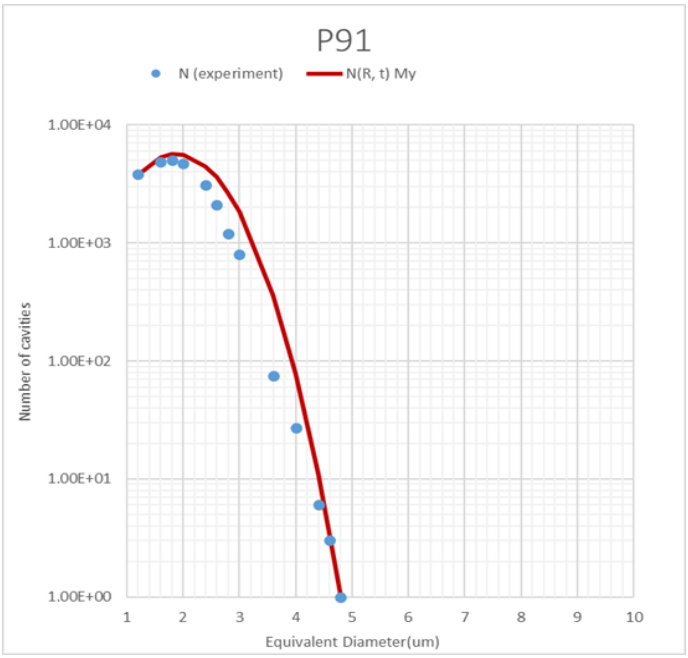

Figure 6.3 The probability density function of cavity equivalent radius for P91 steel by the backward method. Dots: experimental data from Renversade et al. (2014).

Figures 6.1 and 6.3 show that the curves fit going through the first and last point because these curves are based on these two points to calculate the values of A_1 and A_2 et al. This is not a constraint of the algorithm. For example, the line in Figure 6.8 is not going through the first and last point but it also has got a nice curve. This curve fits better than other curves that are based on another two points for P91 steel. It is not to say that method gives too much weight to those two points. The method is that any two points can be chosen, and the curve can go through these two points. However, whether the curve goes through or near to any of the remaining points is the question. In other words, the trend of the curve is the same as its experimental data and almost all points are approaching the curve; this curve is based on these two points. The operation method applies throughout the rest of the material in this thesis, for example, E911 and 316H steels.

According to the values of A_1, A_2, C and t_0, the curve can be extended to include the

state of the minimum diameter. The time occurs before t_0. The following Figure 6.4 displays the prediction curve, including the state of the minimum diameter.

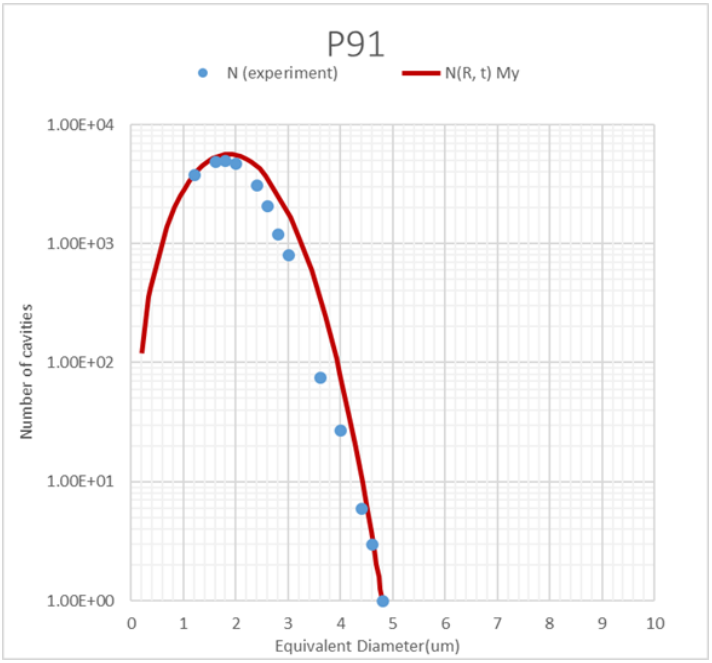

Figure 6.4 The prediction curve, including the condition of the minimum diameter by the backward method for P91 steel. Dots: experimental data from Renversade et al. (2014).

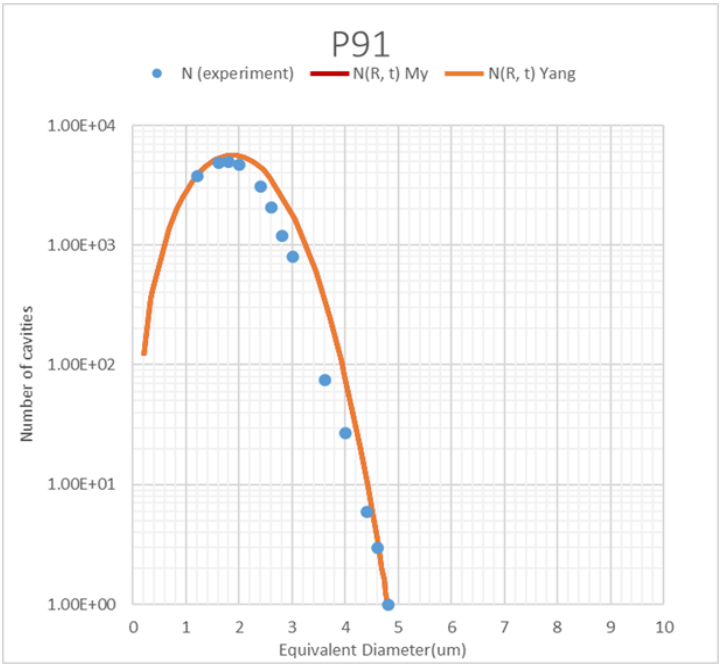

Figure 6.5 The comparison of the accuracy of the two methods for P91 steel. Dots: experimental data from Renversade et al. (2014).

In Figure 6.5, the comparison of the two methods shows that both ways can produce

accurate results and the difference between them is very small to the naked eye. The backward method is better than the forward approach due to its directness for determining A_1 and A_2.

To achieve the predicted curve fitting better with the experimental data than its original curve, the current author put values on the errors from the input points, including plus 10%, minus 10%, 2nd minus 10%, and 3rd minus 10%. The injecting values are shown in Table 6.1 and its prediction curves are shown in Figure 6.6, respectively.

Table 6.1 The injecting values for P91 steel.

Injecting condition	$A_1(\mu m^3/ln(h))$	A_2 ($\mu m^{-3}h^{-2}$)
Original value	8.24×10^{-1}	9.95×10^{-5}
Plus 10%	9.06×10^{-1}	1.09×10^{-4}
Minus 10%	7.41×10^{-1}	8.96×10^{-5}
2nd minus 10%	6.67×10^{-1}	8.06×10^{-5}
3rd minus 10%	6×10^{-1}	7.2×10^{-5}

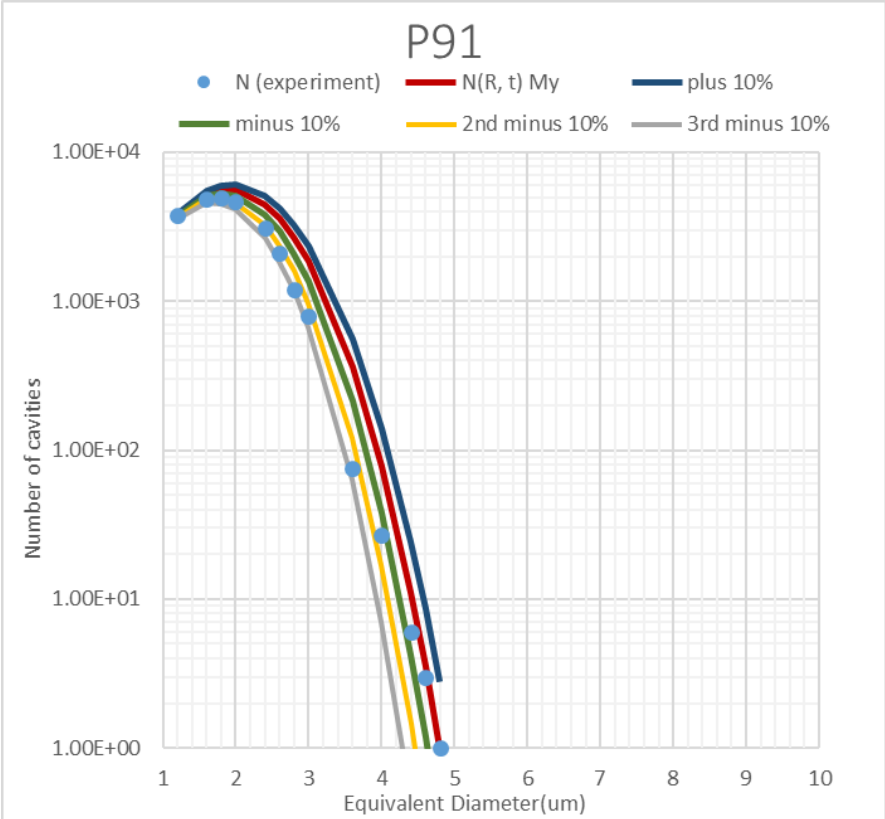

Figure 6.6 Injecting plus 10%, minus10%, 2nd minus 10%, and 3rd minus 10% of the errors from the input points for P91 steel. Dots: experimental data from Renversade et al. (2014).

According to Figure 6.6, when minus 10% of the errors is from the input points, the predicted curve will become a better fit with the experimental data than its original

curve, but it cannot fit the middle diameter levels. The current author when adding minus 10% as fixed values to the second injection, caused the predicted curve to fit better with the experimental data than its first minus 10%. When the author continued to inject the third minus 10%, the curve did not fit well with the experimental data. Thus, the injecting is useful and the predicted curve of 2nd minus 10% is the best fit with the experimental data. The values of C and t_0 can be calculated, respectively, C=-1.55μm^3 and t_0=11.36528h in the 2nd minus 10%. Then the curve can be extended to the condition of the minimum diameter, which occurs before t_0. Figure 6.7 displays the prediction curve, which includes the shape of the minimum diameter and its comparison with the original curve.

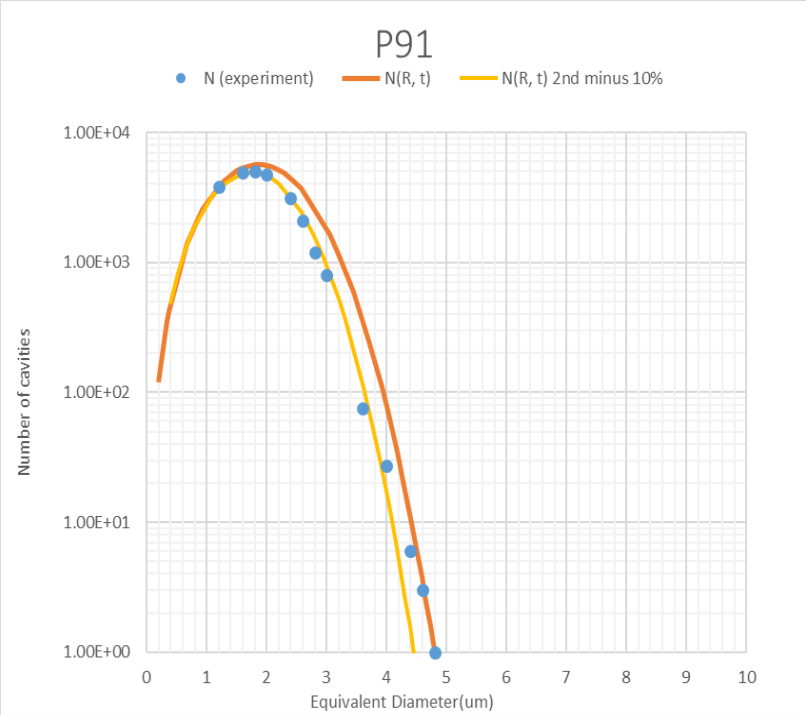

Figure 6.7 The new prediction curves based on injecting 2nd minus 10% of the errors from the input points and including the condition of minimum diameter for P91 steel. Dots: experimental data from Renversade et al. (2014).

Figure 6.7 shows that the prediction curve, including the condition of minimum diameter, fits better with the experimental data than its original curve when 2nd minus 10% of the errors from the input points is added.

According to the exercise for P91 steel, knowing the process for the applied cavitation damage equation and how to calculate the values of A_1 and A_2 based on the forward method require the development of a new calculated method.

6.3.2 Determination of model constant for E911

This part describes that the values of A_1, A_2, C and t_0 for the sample of E911 steel are calculated based on the second (backward) method. The second method has been independently devised to find the numerical answers by the author, which is from the production of a journal paper (Zheng et al., 2020). It directly took two points from the histogram, and the values of A_1 and A_2 can be used to solve the two simultaneous Equations 6.4. The process for this part of the work is:

Firstly, choosing two points for calculation and illustration, it is t_f=37800h, respectively, R_1=1.2μm, $N(R_1, t_f)$ =195 and R_2=4.75μm, $N(R_2, t_f)$ =1.

Secondly, using the above Equation 6.8 with the values of two points solve the value of A_1= 8.76μm^3/ln(h), then according to Equation 6.7.a or Equation 6.7.b with the value of A_1 calculate the value of A_2= 9.47×10^{-7}μm^{-3}h^{-2}.

Thirdly, using the integrating Equation 6.6 with the values of A_1, R_2, and t_f calculate the value of C= -56.607μm^3.

Finally, using the integrating Equation 6.6 with the values of integration constant C, R_1 and A_1 calculate the value of t_0=645.62h.

Thus, the gradation of calculation is the value of A_1, A_2, C and t_0. As the values of A_1 and A_2 can be calculated to C_1 and C_2, another method is used by Equation 6.5.b to solve the value of C_1=154ln(h)/μm^6 and C_2=0.228ln(h)/μm^3. Figure 6.8 displays the predicted curves by using Equation 6.1.b, Equation 6.4 and Equation 6.5.b, all of which fit well with the experimental data, respectively, especially under a diameter bigger than the value 2.4μm. The remaining experimental points under small diameter values cannot be located in the curve. To solve this deficiency, the current author conducted the values of optimisation to get a new curve, which is shown in Figure 6.10.

Figure 6.8 clearly shows that the three equations can produce accurate results. The difference between the three curves is small to the naked eye. Thus, it reversely conforms to the values of α=1, β=2 and γ=1.

Due to the values of A_1, A_2, C and t_0, the curve can be extended to include the condition of the minimum diameter. The time occurs before t_0. Figure 6.9 displays the prediction curves, which includes the shape of the minimum diameter.

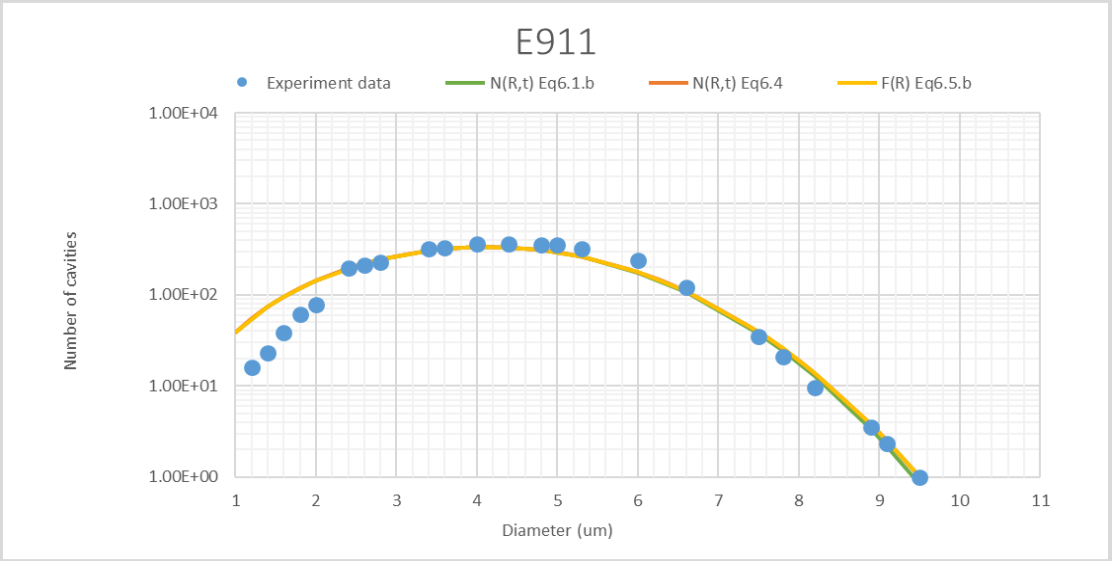

Figure 6.8 No notice of a difference of the predicted probability density function of cavity equivalent radius for E911. Dots: experimental data from Renversade et al. (2014); curves produced by Equations 6.1.b, 6.4 and 6.5.b (Xu et al., 2018b; Zheng et al., 2020).

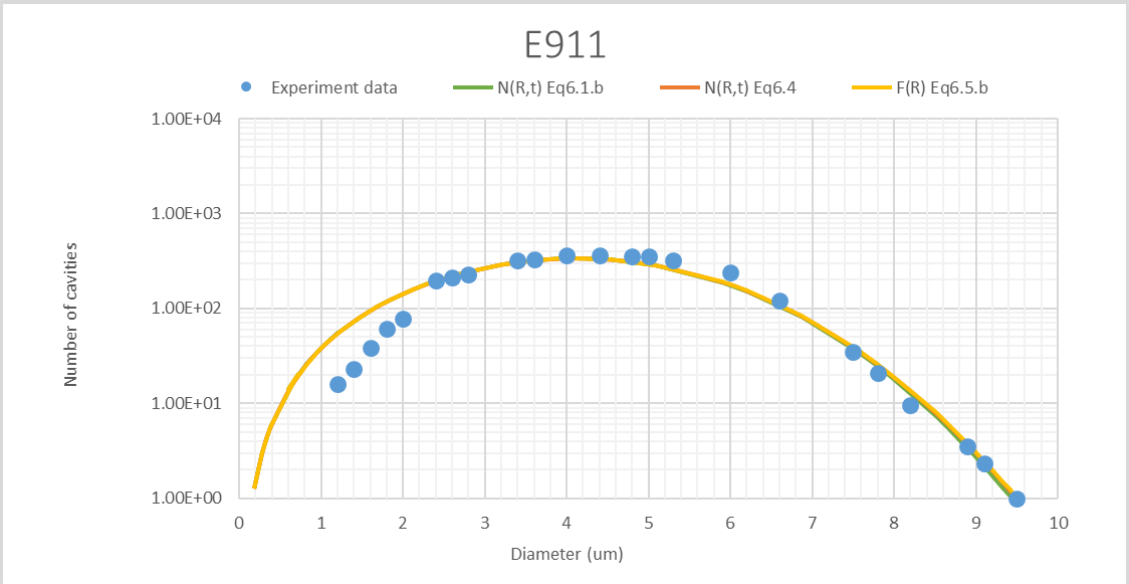

Figure 6.9 No notice of a difference of the predicted probability density function of cavity equivalent radius including the condition of the minimum diameter for E911. Dots: experimental data from Renversade et al. (2014); curves produced by Equations 6.1.b, 6.4 and 6.5.b.

In Figures 6.8 and 6.9, the curves did not fit well with the experimental data under small diameters. To achieve a good fitting curve and values of optimisation, there are two methods: the least square solution and radial basis function. The method of least square solution was chosen, due to its state of belonging to the linear. The reason is that all the

data and factors, which includes important predicted data, are available and satisfied in this case. The specific operation is to obtain a set of values, which are the minimum sum of square errors between the predicted data and the experimental data. After many calculations such as increasing the value of $\beta=2.4$ and updating of the relative new values of A_1, A_2 at the same time, it has set fixed values to add minus 1%, 2%, 3%, 4% until the sum of square errors is the smallest in the set of minus 3%. The sets of values are shown in Table 6.2 and the comparison of the two prediction curves is shown in Figure 6.10.

Table 6.2 The values of the material parameter for E911.

Material parameter	Values	After optimisation values
A_1 ($\mu m^3/ln(h)$)	8.76	13.67
A_2 ($\mu m^{-3}h^{-2}$)	9.47×10^{-7}	1×10^{-6}
α	1	1
β	2	2.472
γ	1	1
C	-56.607	-79.7
t_0 (h)	645.62	341.189
C_1 ($ln(h)/\mu m^6$)	154	104.52
C_2 ($ln(h)/\mu m^3$)	0.228	0.146

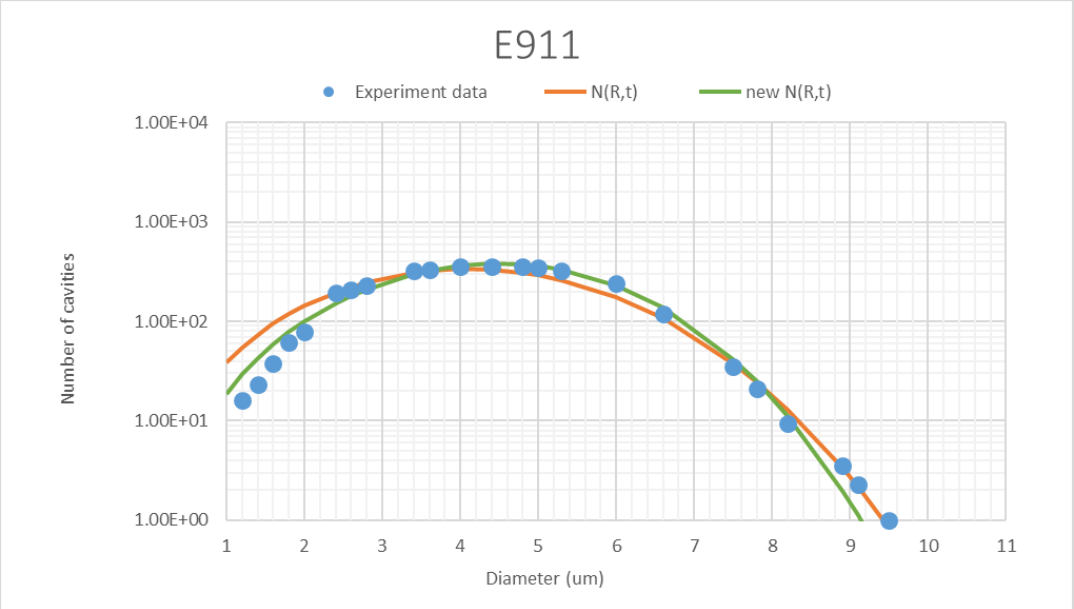

Figure 6.10 The predicted density function of cavity equivalent radius for E911. Dots: experimental data from Renversade et al. (2014); curves produced by Equation 6.1.b based on the original value and after the optimisation value, respectively.

Table 6.3 Comparison of material coefficients for P91 and E911 steels (Zheng et al., 2020).

Material	Temperature (°C)	Axial stress (MPa)	Internal stress (MPa)	lifetime (h)	Parameters A_1 ($\mu m^3/ln(h)$)	Parameters A_2 ($\mu m^{-3}h^{-2}$)
P91	575	52.6	23.6	10200	8.24×10^{-1}	9.95×10^{-5}
E911	600	48.9	17.7	37800	8.76	9.47×10^{-7}

Based on the x-ray microtomography experimental data, the cavity nucleation and cavity growth models for P91 and E911 steels have been calibrated. The comparison of these coefficients for P91 and E911 steels is shown in Table 6.3. The E911 has a much higher growth rate and a much slower nucleation rate than P91 steel.

6.4 The trend of creep lifetime coefficient *U'* with stress levels for P91 and P92

Riedel (1987) propose a generic mathematical formula for the creep cavitation damage. This formula is based on creep cavity nucleation, growth, and coalescence. Xu et al. (2017a) for the first derived a specific mathematical equation for a given nucleation rate model and growth rate model. The current author individually repeats the research method for P91 steel and successfully applied this method to another material for P92 steel. This method is based on the above Equations 6.1, 6.2 and 6.3. From this, the cavity area fraction *w* can be obtained and is shown in Equation 6.9 (Xu et al., 2017a, 2019; Zheng et al., 2020).

$$w = \int \pi R^2 N(R,t) dR \tag{6.9}$$

Substituting the value of α=1, β=2, and γ=1 into Equation 6.9, the cavity area fraction *w* rewrites to the below:

$$w = \pi \times \frac{3}{5} \times 3^{\frac{2}{3}} \times U^5 \times A_1^{\frac{2}{3}} \times A_2 \times t^2 \tag{6.10}$$

If $U' = \pi \times \frac{3}{5} \times 3^{\frac{2}{3}} \times U^5 \times A_1^{\frac{2}{3}} \times A_2$

$$w = U' \times t^2 \tag{6.11}$$

when *w* attains a critical value, this occurs at rupture time. The *w* rewrites to w_f, and the *t* rewrites to t_f.

$$w_f = U' \times t_f^2 \tag{6.12}$$

In discussing the relationship of *U'* with the stress, the value of w_f needs to be determined first. According to Riedel (1987), the critical value w_f can be assumed to be the $\pi/4$. In this chapter, this value was adopted.

6.4.1 The value of coefficient *U'* for P91 steel

The experiment is based on the NIMS creep data sheet at creep rupture time under different stress levels and temperatures for P91 steel. The value of *U'* was calculated and is displayed in Tables 6.4 and 6.5.

Table 6.4 The value of *U'* at 600°C for P91 steel (Xu et al., 2017a; Yang, 2018).

Stress (MPa)	Rupture time (h)	U' (h^{-2})
70	80736.8	1.20489×10^{-10}
100	34141	6.7381×10^{-10}
110	21206.3	1.74647×10^{-9}
120	12858.6	4.7501×10^{-9}
140	3414.7	6.73573×10^{-8}
160	971.2	8.32669×10^{-7}

Table 6.5 The value of *U'* at 625°C for P91 steel (Xu et al., 2017a; Yang, 2018).

Stress (MPa)	Rupture time (h)	U' (h^{-2})
90	21372.4	1.71943×10^{-9}
100	9895.4	8.0209×10^{-9}
120	1657.9	2.85741×10^{-7}
140	399	4.93337×10^{-6}

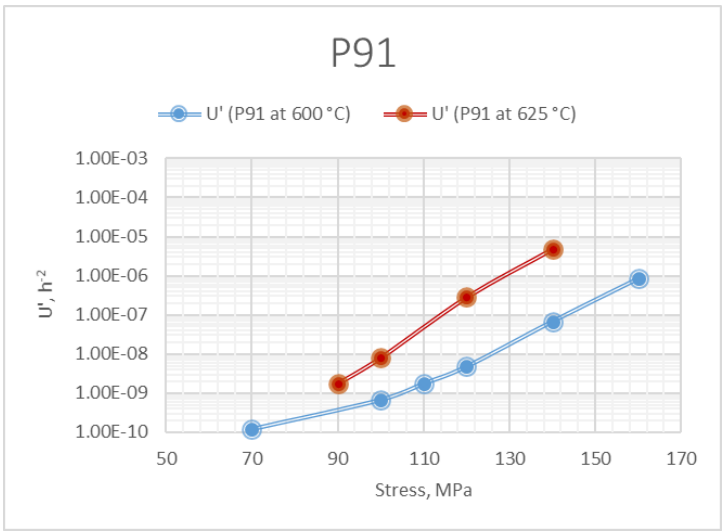

Figure 6.11 The trend of the values of *U'* under different stress and temperature for P91 steel (Xu et al., 2017a; Yang, 2018).

Figure 6.11 shows an apparent trend concerning creep rupture time coefficient *U'* with different stress for P91 steel. In addition, it can provide much more stable scientific findings.

6.4.2 The value of coefficient *U'* for P92 steel

The experiment is based on the NIMS creep data sheet at creep rupture time under different stress levels and temperatures for P92 steel. The value of *U'* was calculated and is summarised in Tables 6.6, 6.7 and 6.8.

Table 6.6 The value of *U'* at 600°C for P92 steel (Xu et al., 2018b; Zheng et al., 2020).

Stress (MPa)	Rupture time (h)	U' (h^{-2})
120	65363.4	1.84×10^{-10}
130	39539.9	5.02×10^{-10}
140	25944.6	1.17×10^{-9}
160	8219.9	1.16×10^{-8}
180	1740.7	2.59×10^{-7}
190	613.4	2.09×10^{-6}
210	112.6	6.19×10^{-5}
230	19.9	1.98×10^{-3}
250	5.1	3.02×10^{-2}

Table 6.7 The value of *U'* at 625°C for P92 steel (Zheng et al., 2020).

Stress (MPa)	Rupture time (h)	U' (h^{-2})
100	33518.5	6.9907×10^{-10}
110	17530	2.5558×10^{-9}
130	3886.1	5.2007×10^{-8}
140	1458.2	3.69365×10^{-7}
160	213.4	1.72465×10^{-5}

Table 6.8 The value of *U'* at 650°C for P92 steel (Xu et al., 2018b; Zheng et al., 2020).

Stress (MPa)	Rupture time (h)	U' (h^{-2})
60	92845.2	9.11×10^{-11}
70	50871.2	3.03×10^{-10}
80	21717.1	1.67×10^{-9}
90	10001.9	7.85×10^{-9}
100	3738.7	5.62×10^{-8}
110	1689.1	2.75×10^{-7}
130	194	2.09×10^{-5}
140	66	1.8×10^{-4}
160	10.5	7.12×10^{-3}

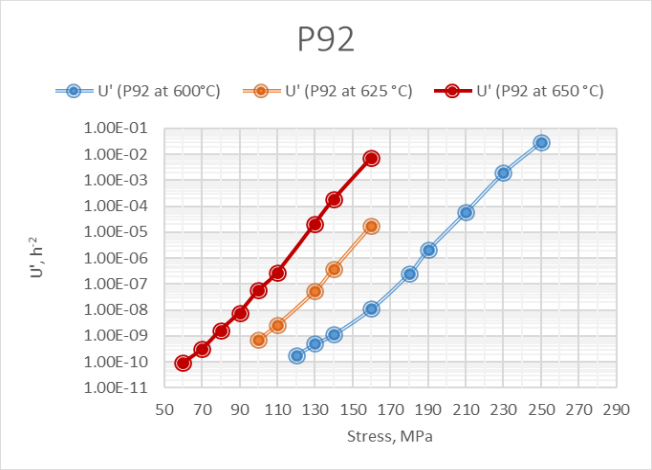

Figure 6.12 The trend of the values of *U'* under different stress and temperature for P92 steel (Zheng et al., 2020).

Figure 6.12 shows an apparent trend concerning creep rupture time coefficient *U'* with different stress for P92 steel. This can provide more stable scientific findings.

The current author wanted to verify the scientific and rationale of the trend. The relevant data were collected by reading the published graph under different stress levels at 600°C and 650°C for P92 steel as in Yin (2006). The value of *U'* was calculated and summarised in Tables 6.9 and 6.10. The trend is shown in Figure 6.13.

Table 6.9 The value of *U'* at 600°C for P92 steel (Zheng et al., 2020).

Stress (MPa)	Rupture time (h)	U' (h^{-2})
110	200000	1.9635×10^{-11}
115	95000	8.70247×10^{-11}
120	65000	1.85893×10^{-10}
135	30000	8.72665×10^{-10}
150	10000	7.85398×10^{-9}
170	3000	8.72665×10^{-8}
185	1000	7.85398×10^{-7}

Table 6.10 The value of *U'* at 650°C for P92 steel (Zheng et al., 2020).

Stress (MPa)	Rupture time (h)	U' (h^{-2})
60	200000	1.9635×10^{-11}
65	95000	8.70247×10^{-11}
70	65000	1.85893×10^{-10}
80	30000	8.72665×10^{-10}
90	10000	7.85398×10^{-9}
105	3000	8.72665×10^{-8}
115	1000	7.85398×10^{-7}

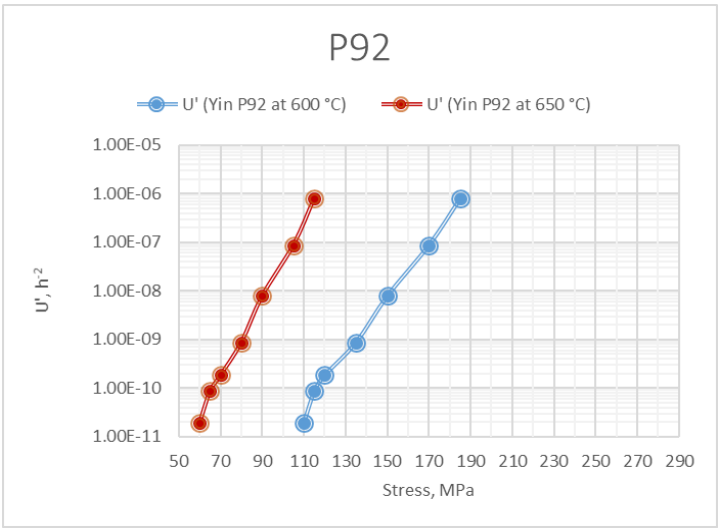

Figure 6.13 The trend of the values of *U'* under different stress and temperature for P92 steel (Xu et al., 2018b; Zheng et al., 2020).

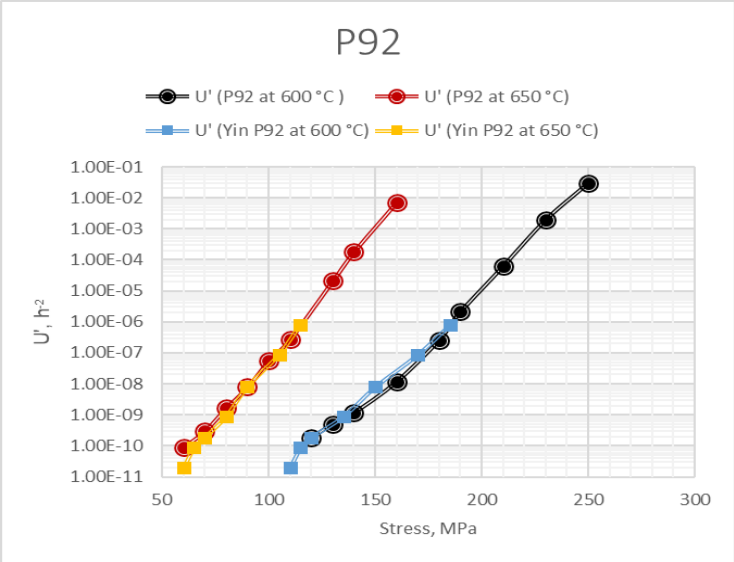

Figure 6.14 Comparison of *U'* with experimental data (NIMS, 2018; Yin, 2006) for P92 steel (Xu et al., 2018b; Zheng et al., 2020).

In Figure 6.14, although experimental data is based on NIMS (2018) and Yin (2006), respectively, the two groups of trend results are the same at 600°C and 650°C. Hence, it provides a scientifically sound and novel method for a predicted lifetime. The detailed prediction method is introduced in Chapter 7.

6.5 The trend of cavity nucleation rate coefficient A_2 under different stress for CB8 and MARBN

If assuming the cavity nucleation rate coefficient A_2 is dependent on the stress in Equation 6.3; simplification is simply no incubation time. Integrating Equation 6.3 with γ=1 shows (Xu et al., 2017a; Zheng et al., 2020):

$$J = \frac{1}{2} A_2 t^2 \tag{6.13}$$

where J is the number density of cavities.

To investigate the dependence between coefficient A_2 and stress, the set of 3D cavitation data are available and referenced by X-ray microtomography technology. Xu et al. (2017a) found experimental data on the number density of cavities at failure for CB8 and researched their relationship. The current author individually repeats this to investigate the relationship and successful application of this method to another material for MARBN.

6.5.1 The value of A_2 for CB8

The number density of cavities at failure for CB8 under over stress levels from 120MPa to 180MPa are available (Gupta et al., 2015). The relevant data is extracted from reading the published graph and table. Using the experimental data, the calculated value of A_2 under different stress is summarised in Table 6.11 and its trend is shown in Figure 6.15.

Table 6.11 The number of cavities at failure and the individual value of A_2 under different stress for CB8.

Stress (MPa)	Lifetime (h)	The number density of cavities ($10^{-5}um^{-3}$)	A_2 ($\mu m^{-3}h^{-2}$)
120	51406	1.0625	8.04139×10^{-10}
135	29466	0.6376	1.46871×10^{-9}
150	15316	0.475	4.04979×10^{-9}
165	6779	0.45	1.95844×10^{-8}
180	2825	0.375	9.39776×10^{-8}

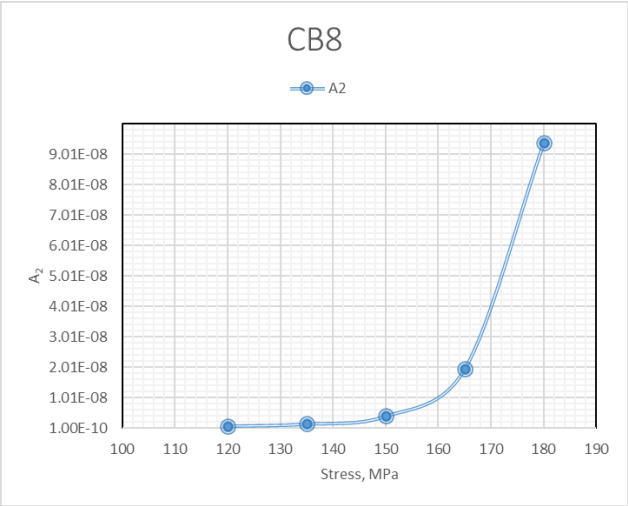

Figure 6.15 The trend of cavity nucleation rate coefficient A_2 under different stress for CB8 (Xu et al., 2017a; Yang, 2018).

From Figure 6.15, A_2 only reduces slightly with stress under below 150MPa.

6.5.2 The value of A_2 for MARBN

Fortunately, another set of 3D cavity experimental data was found by the current author. The number density of cavities for MARBN-heat 1 cross-welds under different stress from 70MPa to 130MPa at rupture time is available (Schlacher, 2015; Gupta et al., 2015). The relevant data was extracted from reading the published graph and table. The experimental data was used to calculate the value of A_2 under different stress levels and is summarised in Table 6.12 with its trend shown in Figure 6.16.

Table 6.12 The number of cavities at rupture time and the individual value of A_2 under different stress for MARBN (Zheng et al., 2020).

Stress (MPa)	Lifetime (h)	The number density of cavities ($10^{-5}um^{-3}$)	A_2 ($\mu m^{-3}h^{-2}$)
70	17200	3.03	2.05×10^{-8}
80	12981	6.95	8.25×10^{-8}
100	8682	7.33	1.94×10^{-7}
130	3433	2.95	5.01×10^{-7}

Figure 6.16 The trend of cavity nucleation rate coefficient A_2 under different stress for MARBN (Zheng et al., 2020).

6.6 Summary

In this chapter, further application of the creep cavitation damage equation on more steel is achieved. The theory is based on the creep fracture model at the grain boundary. A scientifically sound method is based on cavity growth and cavity nucleation. Therefore, the current author is only the second person to apply the creep cavitation damage equation and experimental data produced by the 3D X-ray microtomography technology. The simple method which allows lifetime prediction was proposed for example that the traditional creep damage equation is based on the creep strain; this method is not accurate. The detailed prediction method is introduced in Chapter 7.

Chapter 7 Creep rupture modelling for P92 steel

7.1 Introduction

Creep cavitation at grain boundary is a significant rupture mechanism for P92 steel. This chapter describes the methodology of creep lifetime modelling based on creep cavitation at the grain boundary. The derived equation is generally applicable to a wide range of stress, and it does not depend on creep strain or creep strain rate. The relationship between U' and stress for P91 steel was first reported as a trend curve by Xu (2018a)and Xu et al. (2019). The current author confirms a "novel hyperbolic sine law" equation and applies it for P92 steel at 600°C and 650°C respectively. The creep data was again from NIMS (2018).

The outline for the research in this chapter is as follows:

(1) The relationship between coefficient U' and stress to develop the modelling and determine the material parameters is determined.

(2) The relationship between stress and rupture time to develop the modelling and determine the relative material parameters A_1, and B_1 is determined.

(3) The relationship between minimum strain rate with rupture time to calculate the material parameters is outlined.

(4) The relationship between coefficient U' and minimum strain rate is determined.

Therefore, the main objective is to develop and apply a creep cavitation rupture modelling for P92 steel in this chapter.

The experiment data for this chapter includes:

(1) ASME Grade 92 (9Cr–1.8W–0.5Mo–V-Nb) steels: 1) the temperature at 600℃, stress range from 120MPa to 250MPa, minimum creep rate between 1.81E-5$h^{-1}$and 9.96E-1h^{-1}, lifetime from 5.1h to 65363.4h; 2) the temperature at 650℃, stress range from 60MPa to 160MPa, minimum creep rate between 2.93E-5h^{-1} and 5.6E-1h^{-1}, lifetime from 10.5h to 92845.2h (NIMS, 2018; Zheng et al., 2020).

7.2 The relationship between coefficient *U'* and stress

The value of coefficient U' was calculated in section 7.2. The experimental data is based on the NIMS creep data sheet at creep rupture time under different stress levels and temperature. This section reports the relationship between coefficient U' over a wide range of stress status, especially for low stress levels.

The current author proposes a "novel hyperbolic sine law" that is the same format as that in Equation 5.1. Equation 5.1 is discussed in terms of the relationship between the minimum creep strain rate and stress, but this equation now investigates the relationship between the coefficient *U'* and stress. The equation is shown below:

$$U' = A_1 sinh(B_1 \sigma^q) \tag{7.1}$$

where A_1 and B_1 are material parameters, and q is stress exponent.

The "novel hyperbolic sine law" successfully applied to P92 steel at 600℃ and 650℃, and the values of these material parameters are summarised in Tables 7.1 and 7.2, respectively.

Table 7.1 Material parameters based on the "novel hyperbolic sine law" at 600℃ for P92 steel.

Material parameter	A_1 (h^{-2})	B_1 (MPa^{-2})	q
Value	1.55×10^{-12}	4.00×10^{-4}	2

The current author calibrated the values of material parameters at 600℃ for P92 steel and the corresponding modelling result is shown in Figure 7.1.

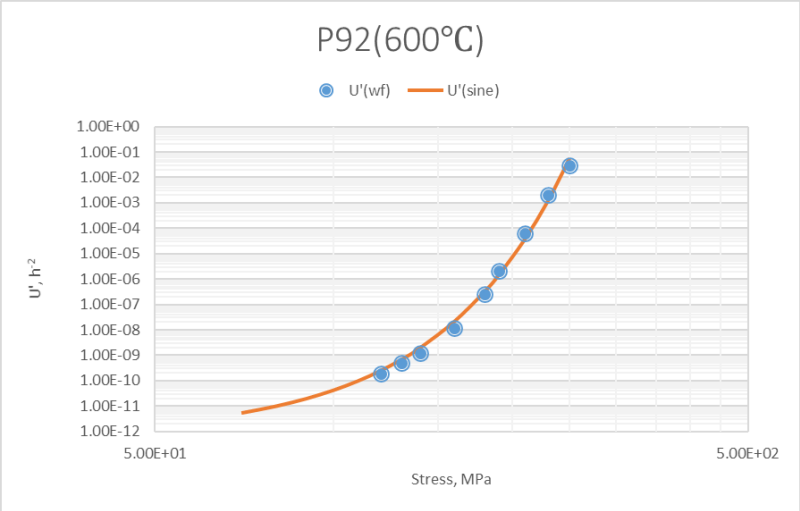

Figure 7.1 The predicted curve of the "novel hyperbolic sine law" compared with experimental data at 600°C for P92 steel (the relationship between *U'* and stress, *U'*(wf) is experimental data).

The comparison of "novel hyperbolic sine law" with their experimental data at 600°C for P92 steel is shown in Figure 7.1. The coefficient *U'* predicted by the "novel hyperbolic sine law" fits very well with the experimental data under a wide range of stress, and therefore a favourable agreement was achieved with our expected results.

Table 7.2 Material parameters based on the "novel hyperbolic sine law" at 650°C for P92 steel.

Material parameter	A_1 (h^{-2})	B_1 (MPa^{-2})	q
Value	1.10×10^{-11}	8.75×10^{-4}	2

The current author again calibrated the values of material parameters at 600°C for P92 steel and the resulting modelling obtained is shown in Figure 7.2.

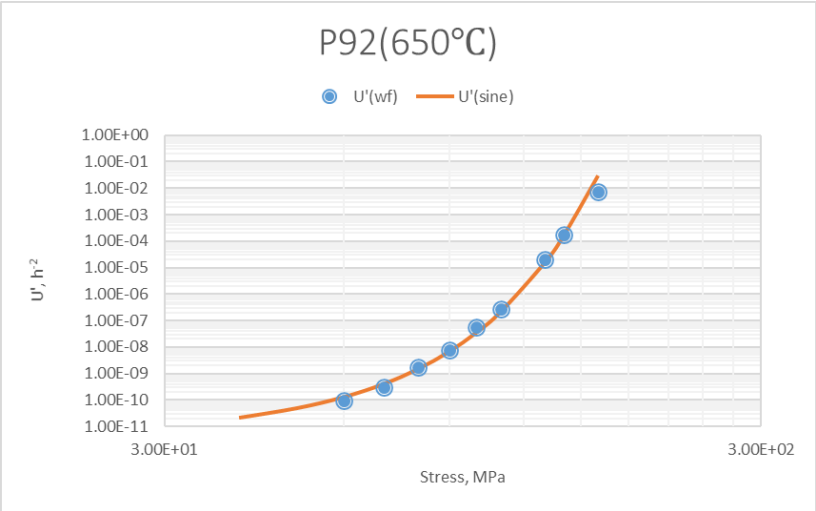

Figure 7.2 The predicted curve of the "novel hyperbolic sine law" compared with experimental data at 650 °C for P92 steel (the relationship between *U'* and stress, *U'*(wf) is experimental data).

Figure 7.2 shows the comparison of "novel hyperbolic sine law" with their experimental data at 650°C for P92 steel. The coefficient *U'* predicted by the "novel hyperbolic sine law" fits well with the experimental data under a wide range of stress, and therefore a favourable agreement was again achieved.

7.3 The relationship between stress and lifetime

According to Samuel et al. (2013) and Sakthivel et al. (2015), the relationship between stress and lifetime are shown in the following Equation 7.2:

$$t_f = A\sigma^{-n} \tag{7.2}$$

where *A* is material parameters, and *n* is stress exponent.

Almost all researchers now believe that the above Equation 7.2 can show the relationship between stress and lifetime. which is based on the function of the power law. The current author used this method to determine the values of *A* and stress exponent *n* at 600°C for P92 steel, which is shown in Table 7.3.

Table 7.3 Material parameters at 600°C for P92 steel.

Material parameter	A	n
Value	1×10^{36}	14.72

The current author again calibrated the values of material parameters at 600°C for P92 steel and the modelling result is shown in Figure 7.3.

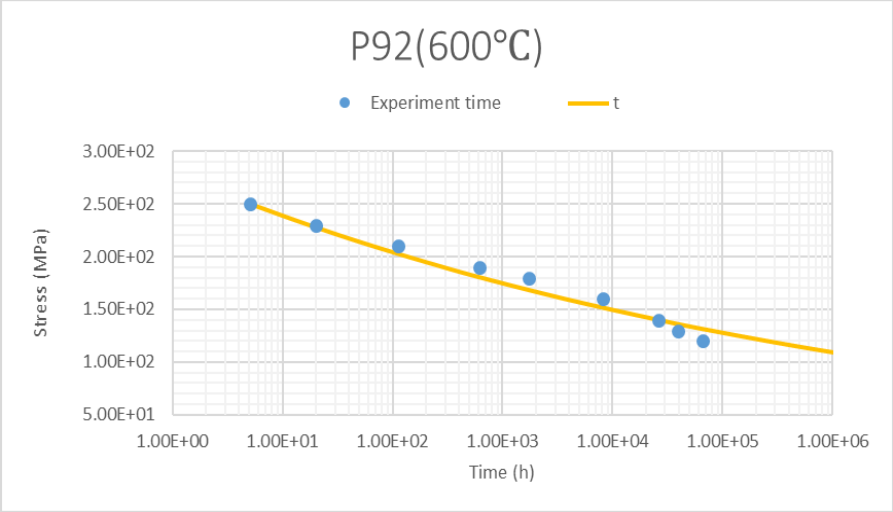

Figure 7.3 The predicted curve of the traditional Equation 7.2 compared with experimental data at 600°C for P92 steel (the relationship between rupture time and stress). Dots: experimental data from NIMS (2018).

In Figure 7.3, the above Equation 7.2 cannot be fitted well against the experimental data at 600°C for P92 steel, and primarily, the trend cannot be satisfied under low stresses and over long time periods.

Samuel et al. (2013) reported the values of stress exponent *n* in two regions at 650°C for P92 steel (as shown in Figure 2.13 in Chapter 2). The current author also used the above method to determine the values of *A* which are summarised in Table 7.4.

Table 7.4 Material parameters at 650°C for P92 steel.

Material parameter	A	n	σ (MPa)
Value	7×10^{11}	3.9	≤80
	6.80×10^{2}	9.7	>80

The current author calibrated the values of *A* and adopted the values of *n* from Samuel et al. (2013) into two regions at 650°C for P92 steel and the modelling result is shown

in Figure 7.4.

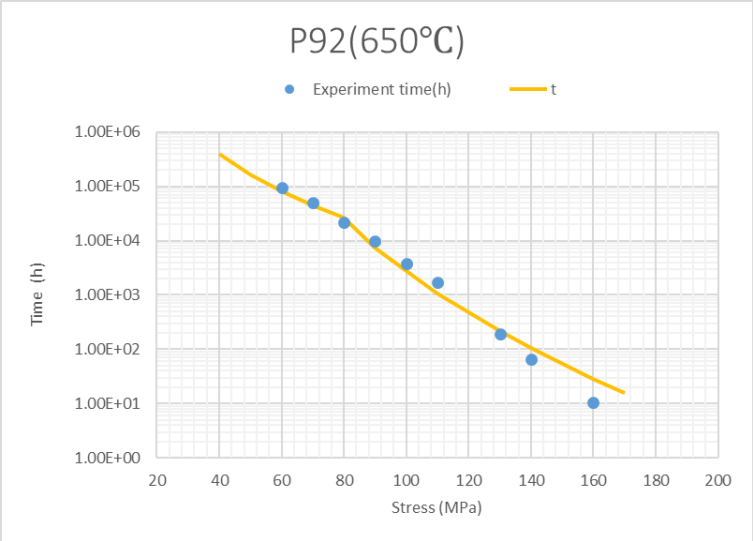

Figure 7.4 The prediction of the traditional Equation 7.2 compared with experimental data at 650°C for P92 steel (the relationship between rupture time and stress). Dots: experimental data from NIMS (2018).

In Figure 7.4, Equation 7.2 also cannot be fitted well against the experimental data at two regions at 650°C for P92 steel. Mainly, the trend cannot be satisfied under low stresses and over long time periods.

The above Equation 7.2 also cannot accurately be used to show the relationship between stress and lifetime in Figure 7.3 and Figure 7.4. Thus, the current author based Equation 6.12 and Equation 7.1 together to get a "novel hyperbolic sine law", and the resulting Equation 7.3 to show its relationship, which is as follows:

$$w_f = U' \times t_f^2 \tag{6.12}$$

$$U' = A_1 sinh(B_1 \sigma^q) \tag{7.1}$$

$$t_f = (W_f/(A_1 sinh(B_1 \sigma^q))^{(\frac{1}{2})} \tag{7.3}$$

When the current author used the "novel hyperbolic sine law" with the values of A_1, B_1 and q which are shown in Table 7.1 at 600°C for P92 steel, the modelling result obtained is displayed in Figure 7.5. The results showing a comparison of the two equations is displayed in Figure 7.6.

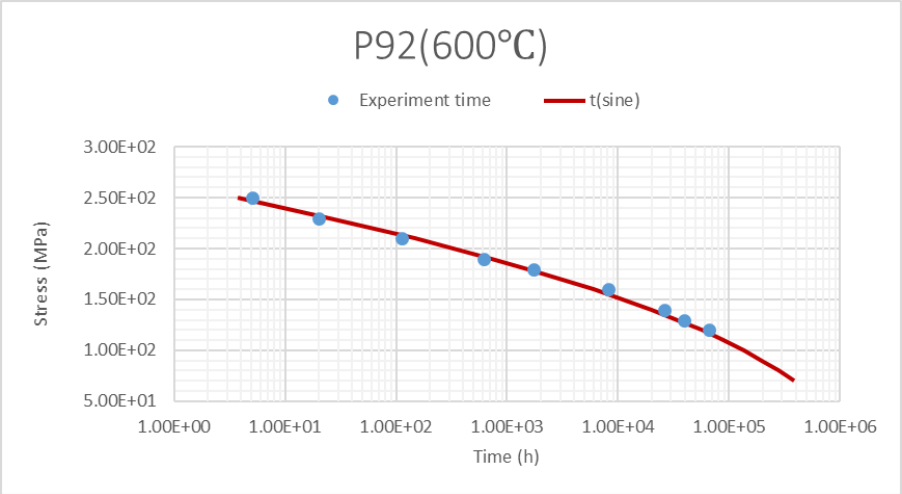

Figure 7.5 The predicted curve of the "novel hyperbolic sine law" at 600°C for P92 steel (the relationship between rupture time and stress). Dots: experimental data from NIMS (2018).

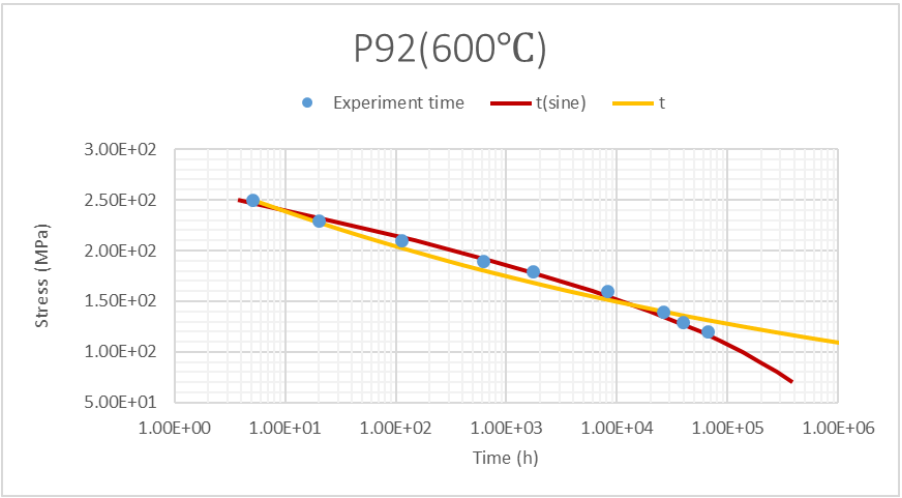

Figure 7.6 The predicted curves compared with experimental data at 600°C for P92 steel.

Figure 7.6 shows curves fitting with the experimental data generated by Equation 7.2 and Equation 7.3, respectively. The "novel hyperbolic sine law" Equation 7.3 can therefore work very well with the experimental data at 600°C for P92 steel, and importantly, the trend can satisfy under low stress and over long time periods.

The current author also used the "novel hyperbolic sine law" with the values of A_1, B_1 and q shown in Table 7.2 at 650°C for P92 steel, the modelling result is displayed in Figure 7.7 and a comparison of the two equations' results are shown in Figure 7.8.

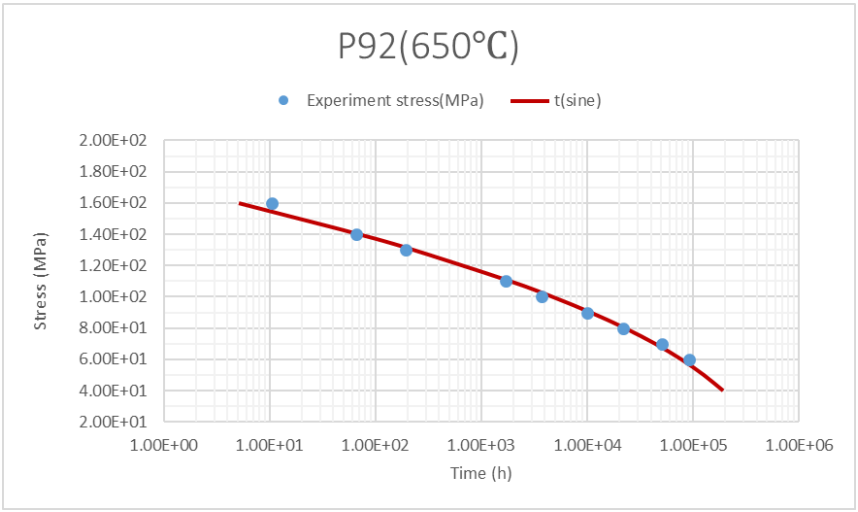

Figure 7.7 The predicted curve of the "novel hyperbolic sine law" compared with experimental data at 650°C for P92 steel (the relationship between rupture time and stress). Dots: experimental data from NIMS (2018).

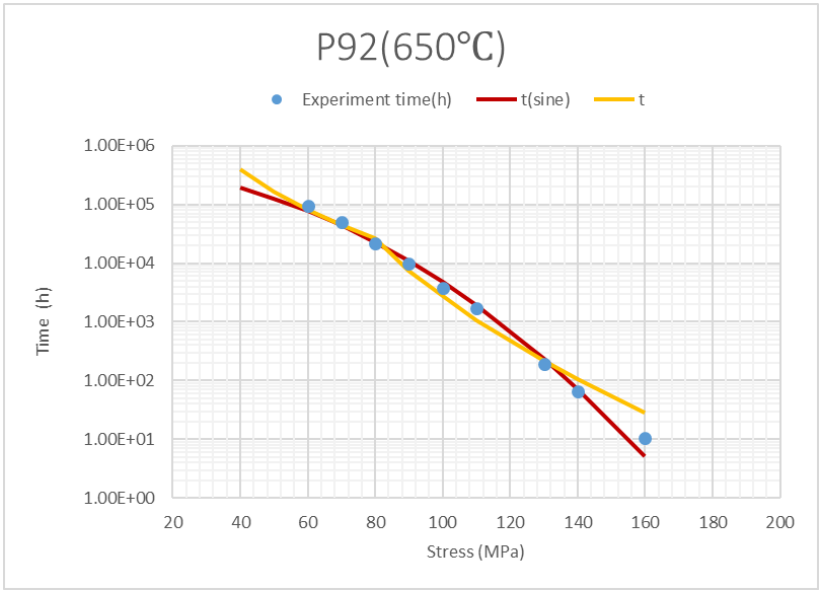

Figure 7.8 The predicted curves compared with experimental data at 650°C for P92 steel.

Figure 7.8 shows curves fitting with the experimental data formed by Equation 7.2 and Equation 7.3, respectively. The "novel hyperbolic sine law" (Equation 7.3) works very well with the experimental data at 650°C for P92 steel, and importantly, the trend can satisfy under low stresses and over long time periods. Equation 7.2 cannot be fitted well against the experimental data even if is divided into two regions.

7.4 The relationship between minimum strain rate and lifetime

The relationship between minimum strain rate and rupture time is reported by the Monkman-Grant (M-G) equation as reported in Monkman et al. (1956), Sakthivel et al. (2015), Panait (2010a), Sundararajan (1989), and Kvapilova et al. (2013):

$$\dot{\varepsilon}_{min} = (\frac{C_{MGR}}{t_f})^{1/m} \tag{7.4}$$

where $\dot{\varepsilon}_{min}$ is the minimum creep rate, t_f is the rupture time, m is the constant and close to unity, C_{MGR} the is Monkman-Grant (M-G) constant. The constant of m and C_{MGR} are independent of the test temperature and applied stress.

The above Equation 7.4 is based on the empirical model. The current author used the equation to determine the values of m and C_{MGR} at 600°C for P92 steel, and it gives the data listed in Table 7.5. The modelling result is shown in Figure 7.9.

Table 7.5 Material parameters based on the Monkman-Grant (M-G) equation at 600°C for P92 steel.

Material parameter	C_{MGR}	m
Value	8.2	8.227×10^{-1}

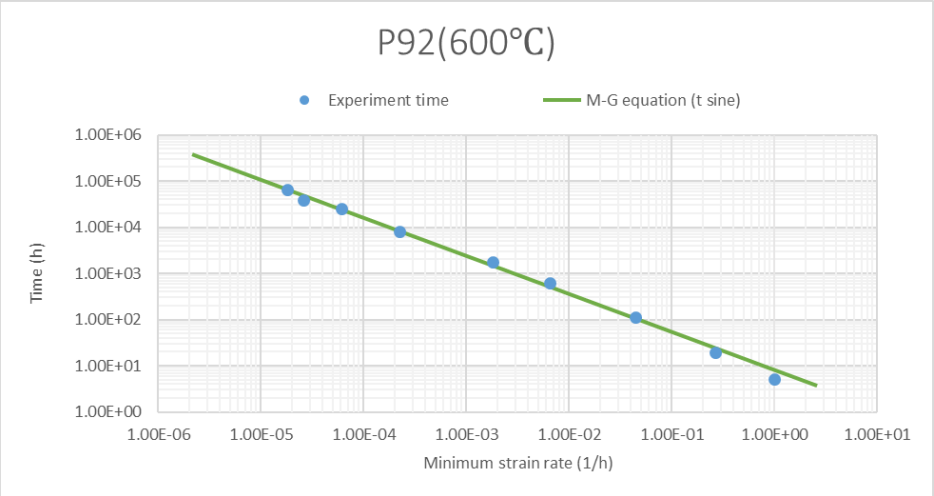

Figure 7.9 The predicted curve of the M-G equation compared with experimental data at 600°C for P92 steel (the relationship between the minimum strain rate and rupture time).

Figure 7.9 shows that the is Monkman-Grant (M-G) equation fits well with the experimental data at 600°C for P92 steel. Importantly, the trend can be satisfied under the condition of low stresses and over long time periods. In addition, the confirmation

of the Monkman-Grant (M-G) equation means it is also suitable for our modelling.

When the current author used Equation 7.4 to determine the values of m and C_{MGR} for P92 steel at 650°C, the values obtained are given in Table 7.6, and the modelling result is displayed in Figure 7.10.

Table 7.6 Material parameters based on the Monkman-Grant (M-G) equation at 650°C for P92 steel.

Material parameter	C_{MGR}	m
Value	6.02	9.24×10^{-1}

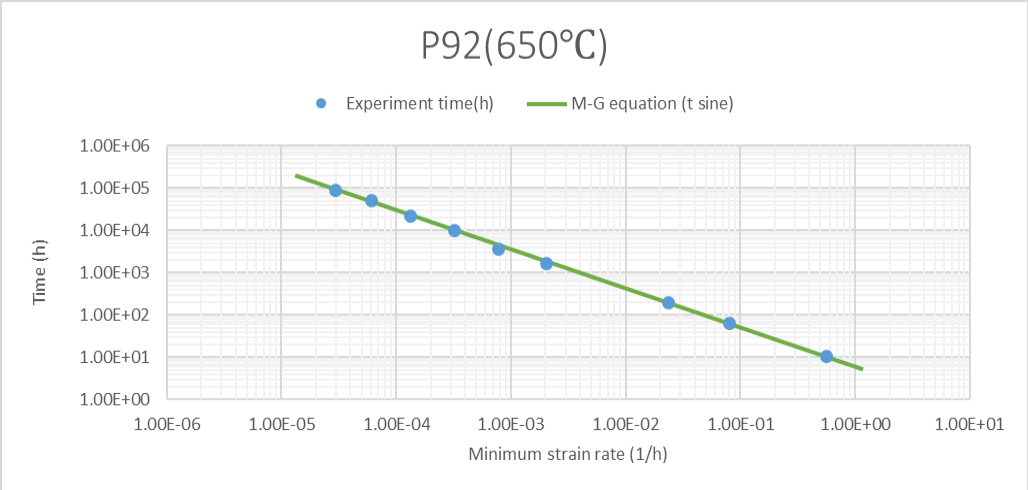

Figure 7.10 The predicted curve of the M-G equation compared with experimental data at 650°C for P92 steel (the relationship between minimum strain rate and rupture time).

Figure 7.10 shows that the Monkman-Grant (M-G) equation fits well with the experimental data at 650°C for P92 steel. Importantly, the trend can be satisfied under the condition of low stresses and over long time periods. In addition, the confirmation of the Monkman-Grant (M-G) equation means that it is suitable for our modelling.

7.5 The relationship between coefficient *U'* and minimum strain rate

In order to research the relationship between coefficient U' and minimum strain rate, the current author based Equation 6.12 and Equation 7.4 together to get a new Equation 7.5 in order to show its relationship. This gives as follows:

$$w_f = U' \times t_f^2 \tag{6.12}$$

$$\dot{\varepsilon}_{min} = \left(\frac{C_{MGR}}{t_f}\right)^{1/m} \tag{7.4}$$

$$\dot{\varepsilon}_{min} = \left(\frac{C_{MGR}}{(W_f/U\prime)^{(\frac{1}{2})}}\right)^{1/m} \tag{7.5}$$

When the current author used the new equation with the values of C_{MGR} and m shown in Tables 7.5 and 7.6 at 600°C and 650°C for P92 steel, respectively, the modelling results obtained are displayed in Figures 7.11 and 7.12.

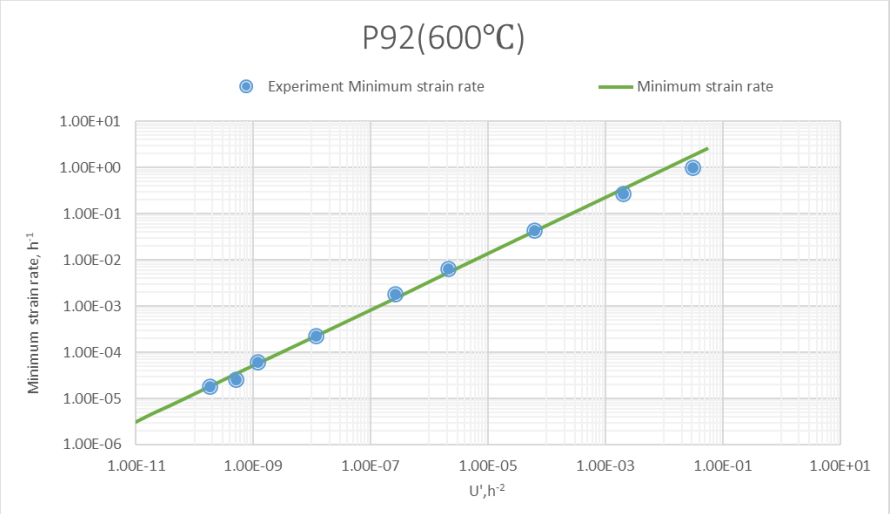

Figure 7.11. The predicted curve of the new equation compared with experimental data at 600°C for P92 steel (the relationship between U' and minimum strain rate).

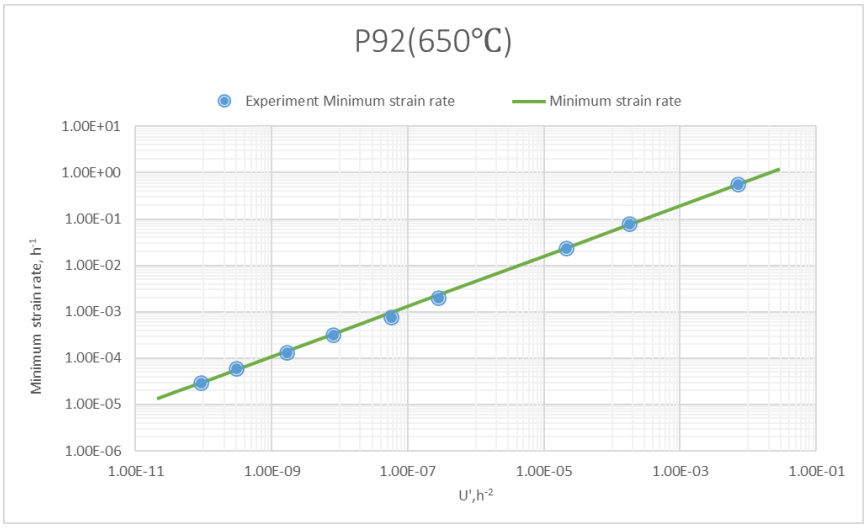

Figure 7.12 The predicted curve of the new equation compared with experimental data at 650°C for P92 steel (the relationship between U' and minimum strain rate).

Figures 7.11 and 7.12 show that the curves produced from Equation 7.5 can both fit well with its experimental data at 600°C and 650°C for P92 steel. In addition, its

confirmation of the relationship between coefficient U' and minimum creep rate exists as the linear connection, and that this can verify that the values of C_{MGR} and U' are accurate in the previous equation.

7.6 Summary

This chapter introduces the discussion on the relationship between coefficient U', stress, rupture time, and minimum strain rate and the described methodology used for developing creep rupture modelling. The creep cavitation rupture modelling was based on the NIMS (2018) data sheet at 600°C and 650°C for P92 steel, respectively. The achievement of the derived Equation 7.3 confirmed that an equation related to sine law and applied at a wide range of stress was the next objective to develop a creep cavitation equation in Chapter 6. Predicting the component lifetime under low stress and over a long time period was more accurate than the traditional Equation 7.2, and it also confirmed that the rupture modelling along the grain boundary is dependent on applied stress and tested temperature, not on the creep strain rate.

Chapter 8 Calibration of creep cavitation model for 316H steel

8.1 Introduction

316H steel has been widely used in the power generation industry during the past ten years. The creep rupture of 316H steel is considered a major problem within the industry. A series of 3D cavitation data set for 316H steel was generated and published within the past two years, but no one has yet developed a creep cavitation model for this steel. The current author has successfully applied a creep cavitation equation on E911 steel (as outlined in Chapter 6). In order to achieve the development of a creep cavitation model for this steel and then observe the changing coefficients of cavity growth and cavity nucleation over time, the current author uses the empirical values of exponent α, β, and γ to calibrate the curve. These values have not investigated or published before, meaning that the curves do not fit well with their corresponding experimental points in this chapter. According to the conclusion of E911 steel, these curves can be optimised by decreasing the value of β. Thus, this chapter aims to develop a creep cavitation model for 316H steel. A creep cavitation model was calibrated for 316H steel at 675°C under 150MPa and 550°C under 320MPa, respectively. The second set of experimental data was subjected to a plastic 8% pre-strain. Jazaeri et al. (2019) reported that using two sets of experimental data is aimed to examine the effects of pre-strain on the creep damage formation and represented its current and future operation in the power plant. Two sets of experimental data were achieved for the development of the creep cavitation model and to further apply the creep cavitation equation for other high Cr steel. The effects of pre-strain on the creep damage formation were not considered in this chapter.

The process of work for this chapter is based on two parts as follows:

(1) The cavity nucleation and cavity growth model used to develop a creep cavitation model at different stages of creep lifetime.

(2) The values of material parameters at rupture time used to research the process of W, J, R, R rate with time.

Thus, the main objective is to develop and calibrate a creep cavitation model at different stages of creep lifetime for 316H steel.

The experimental data for this chapter includes:

(1) The temperature at 675°C, creep time 381h, stress 150MPa (Jazaeri et al., 2019).

(2) The temperature at 550°C, creep time 1287h, stress 320MPa, after 8% pre-strain

(Jazaeri et al., 2019).

8.2 The calculation of model constant at 675°C

This part, based on a theory outlined in section 6.2 and the method described in section 6.3, aimed to develop a creep cavitation model at different stages of creep lifetime, including settings at 18% lifetime, 30% lifetime, 67.5% lifetime, and rupture time. There is no published data covering, for example, 85% lifetime or anywhere else very close to the rupture time; it is important to have results at times periods close to the failure. If there are further data available, the model can be updated. The account percent cannot easily be controlled because of unknown rupture time during the testing. The creep strain contains primary, secondary and tertiary regimes.

8.2.1 Determination of model constant at rupture time

The specimen ID number and rupture time are 11d1 and 381h, respectively. Equation 6.1 is combined with the backward method and used to calculate the values of A_1 and A_2, where the exponent $(\alpha+\gamma)/(1-\alpha) \approx 200$, α=1, β=2, γ=1. In achieving the predicted curve that can fit all experimental points, the values of A_1 and A_2 are continuously modified until it appears as the best curve in Figure 8.1 at present. The values of A_1, A_2, C, and t_0 are shown in Table 8.1. The experimental data and the prediction curve of the cavitation model are shown in Figure 8.1, where the extracted curve includes the condition of minimum diameters.

Table 8.1 The constant at rupture time.

Model constant	A_1 ($nm^3/ln(h)$)	A_2 ($nm^{-3}h^{-2}$)	C (nm^3)	t_0 (h)
Value	4×10^3	1.15×10^{-14}	116853.8	2.0548×10^{-13}

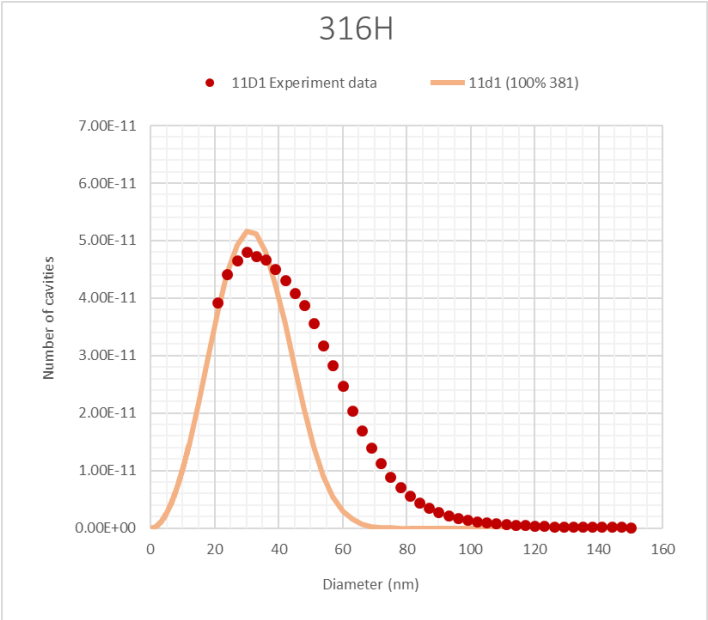

Figure 8.1 The predicted probability density function of cavity equivalent radius at rupture time for 316H, including the condition of the minimum diameter. Dots: experimental data from Jazaeri et al. (2019).

Figure 8.1 shows the calibration of the creep cavitation model for 316H steel at rupture time, in which the prediction curve is not fitting well against the experimental data. However, the trend of the curve is identical to the experiment. This result is acceptable both in the initial stage to develop a cavitation model for 316H steel and before the optimisation stage.

8.2.2 Determination of model constant at 67.5% lifetime

The specimen ID number and time are 12d1 and 257h, respectively. Equation 6.1is combined with the backward method is used to calculate the values of A_1 and A_2, where the exponent $(\alpha+\gamma)/(1-\alpha) \approx 200$, α=1, β=2, γ=1. In achieving the predicted curve that can fit all experimental points, the values of A_1 and A_2 are continuously modified until it appears to be the best curve in Figure 8.2 at present. The values of A_1 and A_2 are shown in Table 8.2. The experimental data and the prediction curve of the cavitation model are shown in Figure 8.2, where the extracted curve includes the condition of minimum diameters.

Table 8.2 The constant at 67.5% lifetime.

Model constant	A_1 ($nm^3/ln(h)$)	A_2 ($nm^{-3}h^{-2}$)
Value	3.9×10^{3}	2.3×10^{-14}

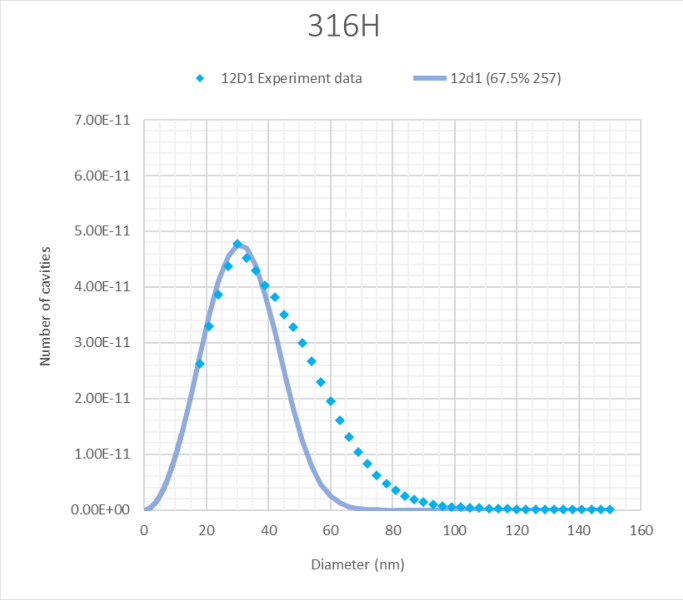

Figure 8.2 The predicted probability density function of cavity equivalent radius at 67.5% lifetime for 316H, including the condition of the minimum diameter. Dots: experimental data from Jazaeri et al. (2019).

Figure 8.2 shows the calibration of the creep cavitation model for 316H steel at 67.5% lifetime, in which the prediction curve is not fitting well against the experimental data. However, the trend of the curve is identical to the experimental data. This result is satisfying both in the initial stage to develop a cavitation model for 316H steel and before the optimisation stage.

8.2.3 Determination of model constant at 30% lifetime

The specimen ID number and time are 13d1 and 114h, respectively. Equation 6.1 is combined with the backward method and used to calculate the values of A_1 and A_2, where the exponent $(\alpha+\gamma)/(1-\alpha) \approx 200$, α=1, β=2, γ=1. In achieving the predicted curve that can fit all experimental points, the values of A_1 and A_2 are continuously modified until it appears the best curve in Figure 8.3 at present. The values of A_1 and A_2 are shown in Table 8.3. The experimental data and the prediction curve of the cavitation model are shown in Figure 8.3, where the extracted curve includes the condition of minimum diameters.

Table 8.3 The constant at 30% lifetime.

Model constant	A_1 ($nm^3/ln(h)$)	A_2 ($nm^{-3}h^{-2}$)
Value	3.95×10^{3}	1.15×10^{-13}

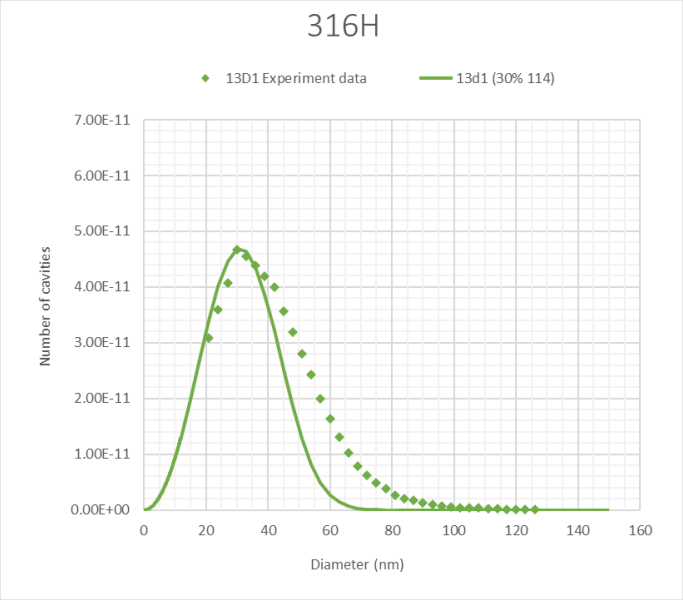

Figure 8.3 The predicted probability density function of cavity equivalent radius at 30% lifetime for 316H, including the condition of the minimum diameter. Dots: experimental data from Jazaeri et al. (2019).

Figure 8.3 shows the calibration of the creep cavitation model for 316H steel at 30% rupture time, in which the prediction curve is not fitting very well against the experimental data. However, the trend of the curve is identical to the experimental data. This result is satisfying both in the initial stage to develop a cavitation model for 316H steel and before the optimisation stage.

8.2.4 Determination of model constant at 18% lifetime

The specimen ID number and time are 14d1 and 69h, respectively. Equation 6.1 is combined with the backward method and used to calculate the values of A_1 and A_2, where the exponent $(\alpha+\gamma)/(1-\alpha) \approx 200$, α=1, β=2, γ=1. In achieving the predicted curve that can fit all experimental points, the values of A_1 and A_2 are continuously modified until it appears the best curve in Figure 8.4 at present. The values of A_1 and A_2 are shown in Table 8.4. The experimental data and the prediction curve of the cavitation model are shown in Figure 8.4, where the extracted curve includes the condition of minimum diameters.

Table 8.4 The constant at 18% lifetime.

Model constant	A_1 ($nm^3/ln(h)$)	A_2 ($nm^{-3}h^{-2}$)
Value	1.42×10^{3}	3.15×10^{-13}

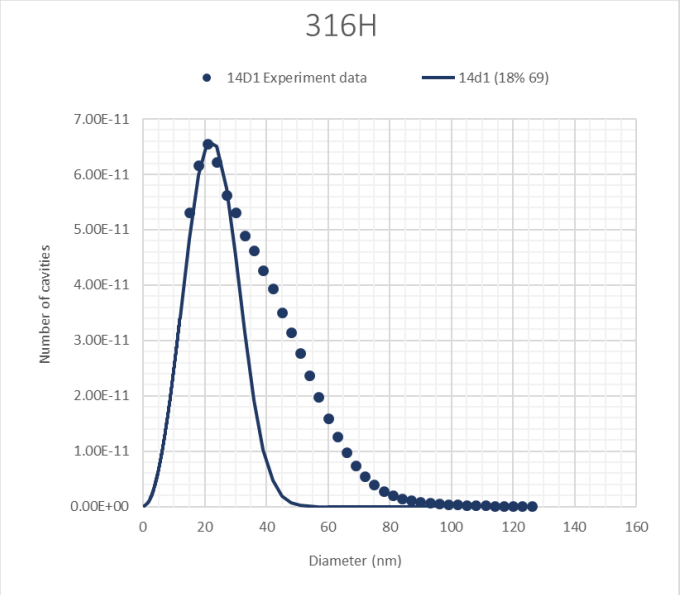

Figure 8.4 The predicted probability density function of cavity equivalent radius at 18% lifetime for 316H, including the condition of the minimum diameter. Dots: experimental data from Jazaeri et al. (2019).

Figure 8.4 shows the calibration of the creep cavitation model for 316H steel at 18% lifetime, in which the prediction curve is not fitting very well against the experimental data. However, the trend of the curve is identical to the experimental data. This result is satisfying both in the initial stage to develop a cavitation model for 316H steel and before the optimisation stage.

Thus, a creep cavitation model was developed for 316H at 675°C under 150MPa. The creep cavitation model at different stages of creep lifetime is shown in Figure 8.5.

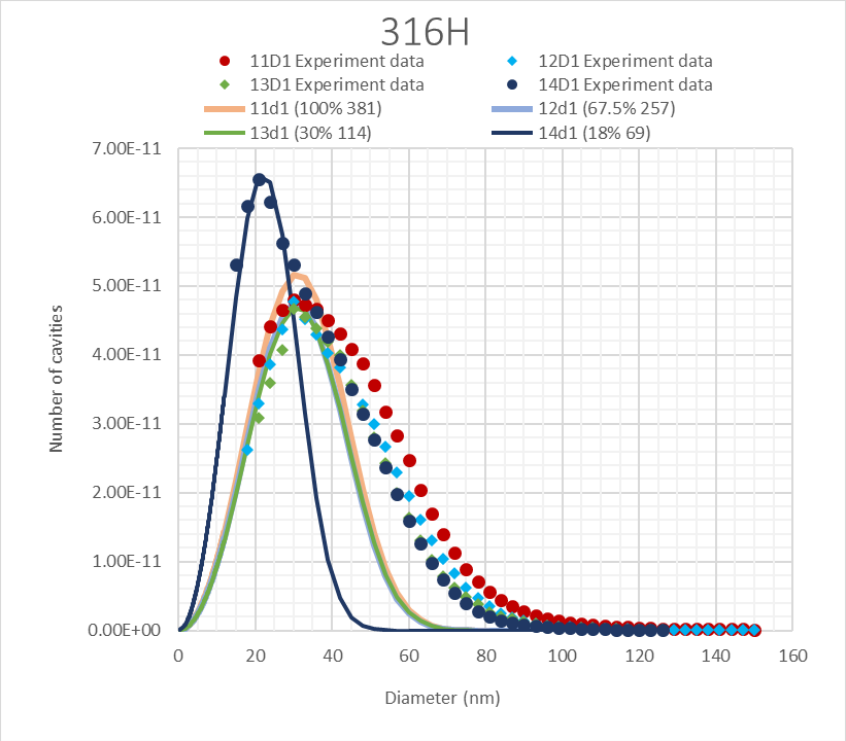

Figure 8.5 The prediction curve of the creep cavitation model and their experimental data at different stages of creep lifetime under 150MPa.

Figure 8.5 shows the calibration of the creep cavitation model for 316H steel at different stages of creep lifetime under 150MPa, in which the prediction curves are not fitting very well against the experimental data at different stages. However, the trend of the curve is identical to the experimental data. This result is satisfying both in the initial stage to develop a cavitation model for 316H steel and before the optimisation stage. An unaffected observation in the trend of coefficient A_1, A_2 is changed with time.

The model constants for the creep cavitation model are summarised in Table 8.5 and its trend of A_1 and A_2 with time is shown in Figure 8.6.

Table 8.5 The model constants under 150MPa.

Sample ID	time (h)	time/lifetime (%)	A_1 ($nm^3/ln(h)$)	A_2 ($nm^{-3}h^{-2}$)
14D1	69	18%	1.42×10^{3}	3.15×10^{-13}
13D1	114	30%	3.95×10^{3}	1.15×10^{-13}
12D1	257	67.50%	3.9×10^{3}	2.3×10^{-13}
11D1	381	100%	4×10^{3}	1.15×10^{-14}

1)

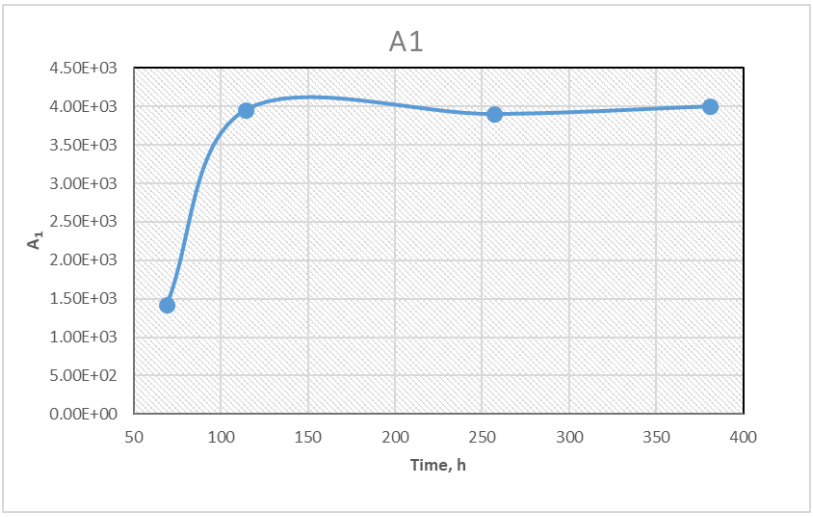

2)

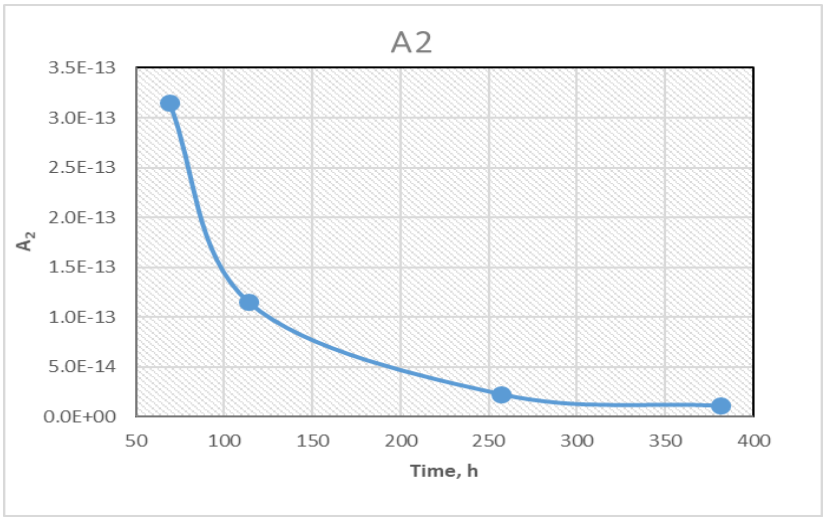

Figure 8.6 The trend of the coefficient: 1) A_1; 2) A_2 with time under 150MPa.

From Table 8.5 and Figure 8.6, the model indicates that the cavity growth rate is increasing by 181.69% while the nucleation rate is decreasing 96.35% during the lifetime. The parameter of the first point is significantly affected because some original voids have been brought into the sample during the production process, and as a result, the accuracy of the first point in the calculated parameters can be affected by these voids. This is one reason for the great change in the first parameter in Figure 8.6. The non-coalesced voids is another reason for changing the coefficient values. The application of the developed cavitation model indicates the characteristics of creep lifetime.

Based on Equation 6.11 with the values of A_1 and A_2. The change of U' over a lifetime is shown in Figure 8.7.

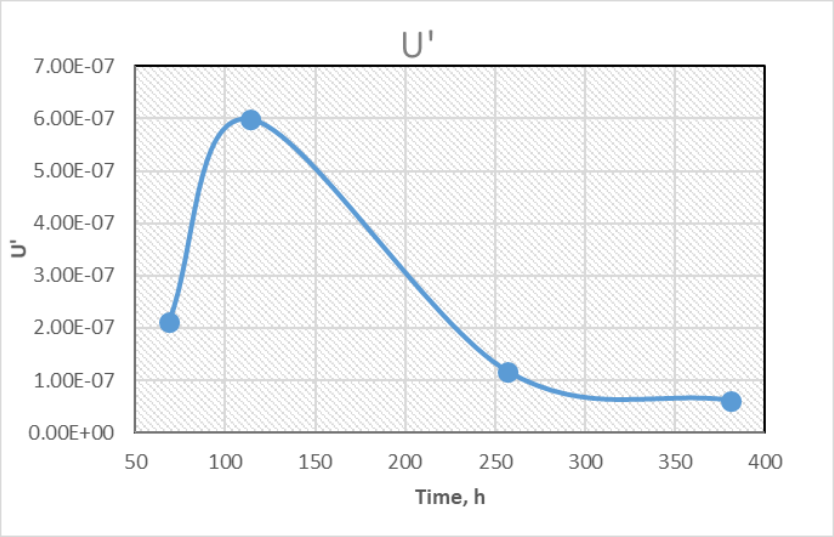

Figure 8.7. The trend of U' over lifetime under 150MPa.

The creep cavitation lifetime coefficient U' is decreasing 89.75% from 30% lifetime to rupture time in Figure 8.7. The change of U' over a lifetime is useful.

8.3 The calculation of model constant at 550°C (after 8% pre-strain)

This section, based on the theory outlined in section 6.2 and a method described in section 6.3, seeks to develop a creep cavitation model at different stages of creep lifetime, including stages at 1% lifetime, 10% lifetime, 22% lifetime, 55% lifetime, 90% lifetime and rupture time. The creep strain contains primary, secondary and tertiary regimes.

8.3.1 Determination of model constant at rupture time (after 8% pre-strain)

The specimen ID number and rupture time are 3d1 and 1287h, respectively. Equation 6.1 is combined with the backward method and used to calculate the values of A_1 and A_2, where the exponent $(\alpha+\gamma)/(1-\alpha) \approx 200$, α=1, β=2, γ=1. In achieving the predicted curve that can fit all experimental points, the values of A_1 and A_2 are continuously modified until it appears the best curve in Figure 8.8 at present. The values of A_1 and A_2 are shown in Table 8.6. The experimental data and the prediction curve of the cavitation model are shown in Figure 8.8, where the extracted curve includes the condition of minimum diameters.

Table 8.6 The constant at rupture time (after 8% pre-strain).

Model constant	A_1 ($nm^3/ln(h)$)	A_2 ($nm^{-3}h^{-2}$)	C	t_0 (h)
Value	2.4×10^{2}	7.8×10^{-15}	15859.70839	1.99955×10^{-29}

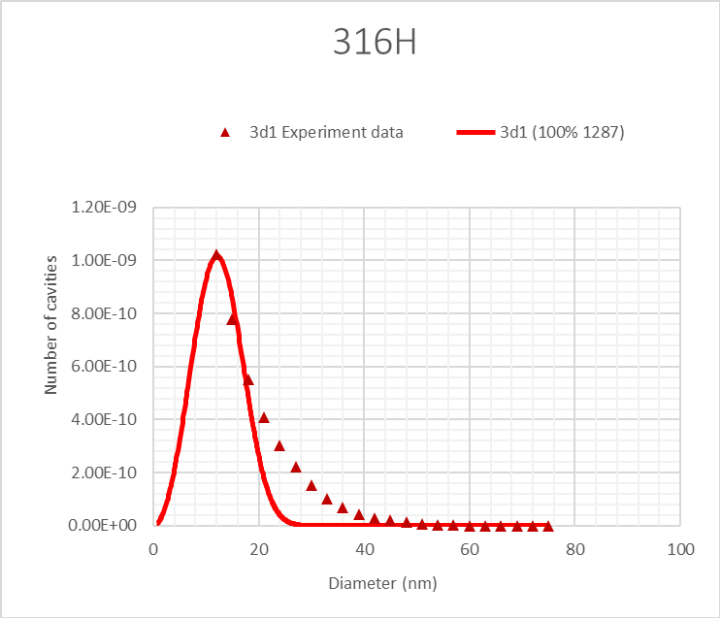

Figure 8.8 The predicted probability density function of cavity equivalent radius at rupture time for 316H (after 8% pre-strain), including the condition of the minimum diameter. Dots: experimental data from Jazaeri et al. (2019).

Figure 8.8 shows the calibration of the creep cavitation model for 316H steel at rupture time, in which the prediction curve is not fitting very well against the experimental data. However, the trend of the curve is identical to the experimental data. This result is satisfying both in the initial stage to develop a cavitation model for 316H steel and before the optimisation stage.

8.3.2 Determination of model constant at 90% lifetime

The specimen ID number and time are 2d1 and 1158h, respectively. Equation 6.1is combined with the backward method and used to calculate the values of A_1 and A_2, where the exponent $(\alpha+\gamma)/(1-\alpha) \approx 200$, α=1, β=2, γ=1. In achieving the predicted curve that can fit all experimental points, the values of A_1 and A_2 are continuously modified until it appears the best curve in Figure 8.9 at present. The values of A_1 and A_2 are shown in Table 8.7. The experimental data and the prediction curve of the cavitation model are shown in Figure 8.9, where the extracted curve includes the condition of minimum diameters.

Table 8.7 The constant at 90% lifetime (after 8% pre-strain).

Model constant	A_1 ($nm^3/ln(h)$)	A_2 ($nm^{-3}h^{-2}$)
Value	2.25×10^{2}	8.40×10^{-15}

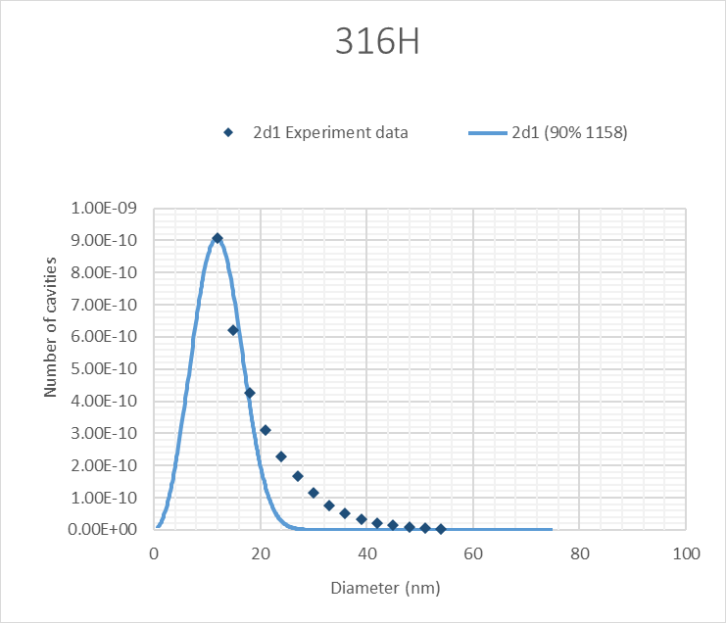

Figure 8.9 The predicted probability density function of cavity equivalent radius at 90% lifetime for 316H (after 8% pre-strain), including the condition of the minimum diameter. Dots: experimental data from Jazaeri et al. (2019).

Figure 8.9 shows the calibration of the creep cavitation model for 316H steel at 90% rupture time, in which the prediction curve is not fitting very well against the experimental data. However, the trend of the curve is identical to the experimental data. This result is satisfying both in the initial stage to develop a cavitation model for 316H steel and before the optimisation stage.

8.3.3 Determination of model constant at 55% lifetime

The specimen ID number and time are 6d1 and 708h, respectively. Equation 6.1 is combined with the backward method and used to calculate the values of A_1 and A_2, where the exponent $(\alpha+\gamma)/(1-\alpha) \approx 200$, α=1, β=2, γ=1. In achieving the predicted curve that can fit all experimental points, the values of A_1 and A_2 are continuously modified until it appears the best curve in Figure 8.10 at present. The values of A_1 and A_2 are shown in Table 8.8. The experimental data and the prediction curve of the cavitation model are shown in Figure 8.10, where the extracted curve includes the condition of minimum diameters.

Table 8.8 The constant at 55% lifetime (after 8% pre-strain).

Model constant	A_1 ($nm^3/ln(h)$)	A_2 ($nm^{-3}h^{-2}$)
Value	2.6×10^{2}	7.6×10^{-15}

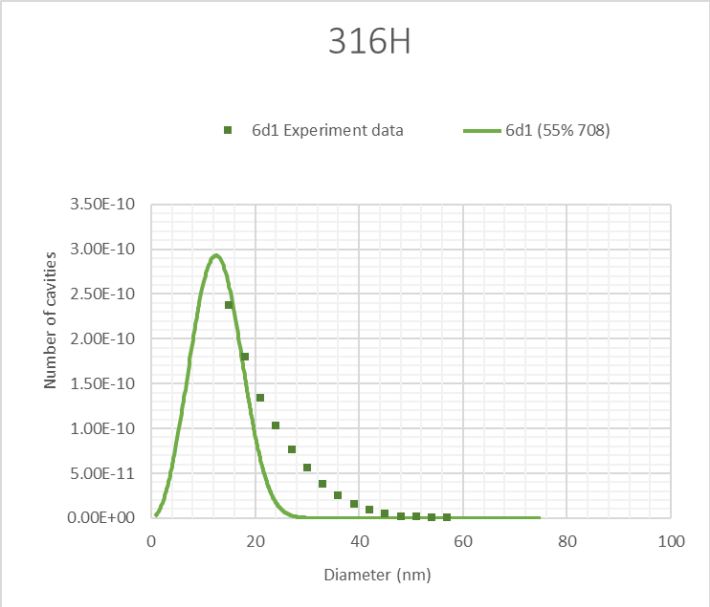

Figure 8.10 The predicted probability density function of cavity equivalent radius at 55% lifetime for 316H (after 8% pre-strain), including the condition of the minimum diameter. Dots: experimental data from Jazaeri et al. (2019).

Figure 8.10 shows the calibration of the creep cavitation model for 316H steel at 55% rupture time, in which the prediction curve is not fitting very well against the experimental data. However, the trend of the curve is identical to the experimental data. This result is satisfying both in the initial stage to develop a cavitation model for 316H steel and before the optimisation stage.

8.3.4 Determination of model constant at 22% lifetime

The specimen ID number and time are 10d1 and 283h, respectively. Equation 6.1 is combined with the backward method and used to calculate the values of A_1 and A_2, where the exponent $(\alpha+\gamma)/(1-\alpha) \approx 200$, α=1, β=2, γ=1. In achieving the predicted curve that can fit all experimental points, the values of A_1 and A_2 are continuously modified until it appears the best curve in Figure 8.11 at present. The values of A_1 and A_2 are shown in Table 8.9. The experimental data and the prediction curve of the cavitation model are shown in Figure 8.11, where the extracted curve includes the condition of minimum diameters.

Table 8.9 The constant at 22% lifetime (after 8% pre-strain).

Model constant	A_1 ($nm^3/ln(h)$)	A_2 ($nm^{-3}h^{-2}$)
Value	2.2×10^{2}	3×10^{-14}

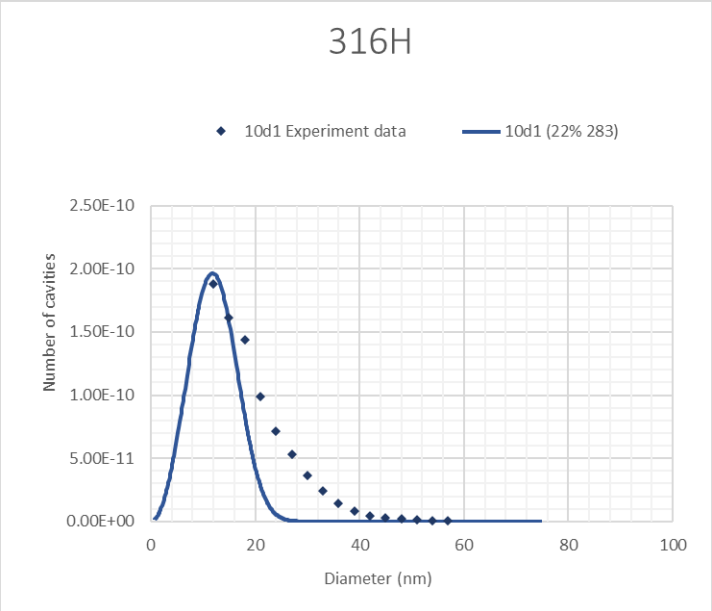

Figure 8.11 The predicted probability density function of cavity equivalent radius at 22% lifetime for 316H (after 8% pre-strain), including the condition of the minimum diameter. Dots: experimental data from Jazaeri et al. (2019).

Figure 8.11 shows the calibration of the creep cavitation model for 316H steel at 22% rupture time, in which the prediction curve is not fitting very well against the experimental data. However, the trend of the curve is identical to the experimental data. This result is satisfying both in the initial stage to develop a cavitation model for 316H steel and before the optimisation stage.

8.3.5 Determination of model constant at 10% lifetime

The specimen ID number and time are 9d1 and 129h, respectively. Equation 6.1 is combined with the backward method and used to calculate the values of A_1 and A_2, where the exponent $(\alpha + \gamma)/(1 - \alpha) \approx 200$, α=1, β=2, γ=1. In achieving the predicted curve that can fit all experimental points, the values of A_1 and A_2 are continuously modified until it appears the best curve in Figure 8.12 at present. The values of A_1 and A_2 are shown in Table 8.10. The experimental data and the prediction curve of the cavitation model are shown in Figure 8.12, where the extracted curve includes the condition of minimum diameters.

Table 8.10 The constant at 10% lifetime (after 8% pre-strain).

Model constant	A_1 ($nm^3/ln(h)$)	A_2 ($nm^{-3}h^{-2}$)
Value	2.2×10^{2}	1.6×10^{-13}

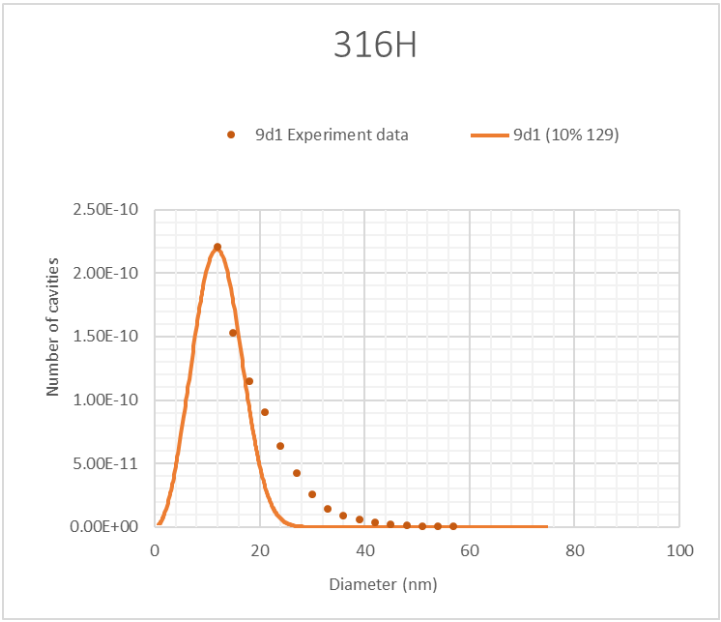

Figure 8.12 The predicted probability density function of cavity equivalent radius at 10% lifetime for 316H (after 8% pre-strain), including the condition of the minimum diameter. Dots: experimental data from Jazaeri et al. (2019).

Figure 8.12 shows the calibration of the creep cavitation model for 316H steel at 10% rupture time, in which the prediction curve is not fitting very well against the experimental data. However, the trend of the curve is identical to the experimental data. This result is satisfying both in the initial stage to develop a cavitation model for 316H steel and before the optimisation stage.

8.3.6 Determination of model constant at 1% lifetime

The specimen ID number and time are 5d1 and 13h, respectively. Equation 6.1 is combined with the backward method and used to calculate the values of A_1 and A_2, where the exponent $(\alpha+\gamma)/(1-\alpha) \approx 200$, α=1, β=2, γ=1. In achieving the predicted curve that can fit all experimental points, the values of A_1 and A_2 are continuously modified until it appears the best curve in Figure 8.13 at present. The values of A_1 and A_2 are shown in Table 8.11. The experimental data and the prediction curve of the cavitation model are shown in Figure 8.13, where the extracted curve includes the condition of minimum diameters.

Table 8.11 The constant at 1% lifetime (after 8% pre-strain).

Model constant	A_1 ($nm^3/ln(h)$)	A_2 ($nm^{-3}h^{-2}$)
Value	2.2×10^{2}	8×10^{-12}

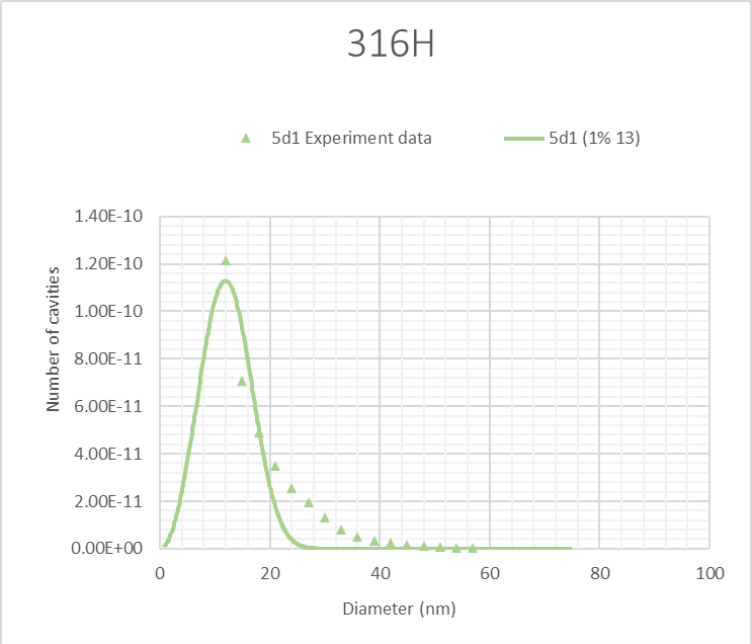

Figure 8.13 The predicted probability density function of cavity equivalent radius at 1% lifetime for 316H (after 8% pre-strain), including the condition of the minimum diameter. Dots: experimental data from Jazaeri et al. (2019).

Figure 8.13 shows the calibration of the creep cavitation model for 316H steel at 1% rupture time, in which the prediction curve is not fitting very well against the experimental data. However, the trend of the curve is identical to the experimental data. This result is satisfying both in the initial stage to develop a cavitation model for 316H steel and before the optimisation stage.

Thus, a creep cavitation model was developed for 316H steel at 550°C under 320MPa. The creep cavitation model at different stages of creep lifetime is shown in Figure 8.14.

Figure 8.14 shows the calibration of the creep cavitation model for 316H steel at different stages of creep lifetime under 320MPa, in which the prediction curves are not fitting very well against its experimental data at different stages. However, the trend of the curve is identical to the experimental data. This result is satisfying both in the initial stage to develop a cavitation model for 316H steel and before the optimisation stage. An unaffected observation to the trend of coefficient A_1, A_2 is changed with time.

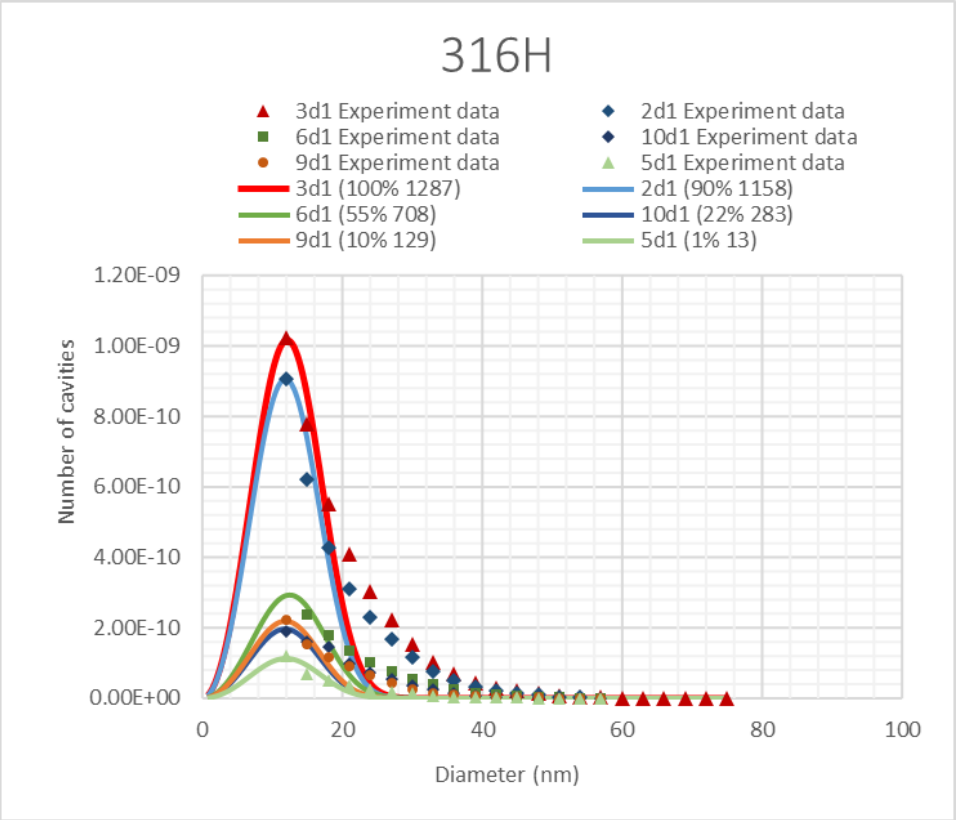

Figure 8.14 The prediction curve of the creep cavitation model and its experimental data at different stages of creep lifetime under 320MPa (after 8% pre-strain).

The model constants for the creep cavitation model are summarised in Table 8.12 and its trend of A_1 and A_2 with time is shown in Figure 8.15.

Table 8.12 The constants under 320MPa.

Sample ID	time (h)	time/lifetime (%)	A_1 ($nm^3/ln(h)$)	A_2 ($nm^{-3}h^{-2}$)
5d1	13	1%	2.2×10^{2}	8×10^{-12}
9d1	129	10%	2.2×10^{2}	1.6×10^{-13}
10d1	283	22%	2.2×10^{2}	3×10^{-14}
6d1	708	55.00%	2.6×10^{2}	7.6×10^{-15}
2d1	1158	90.00%	2.25×10^{2}	8.4×10^{-15}
3d1	1287	100%	2.4×10^{2}	7.8×10^{-15}

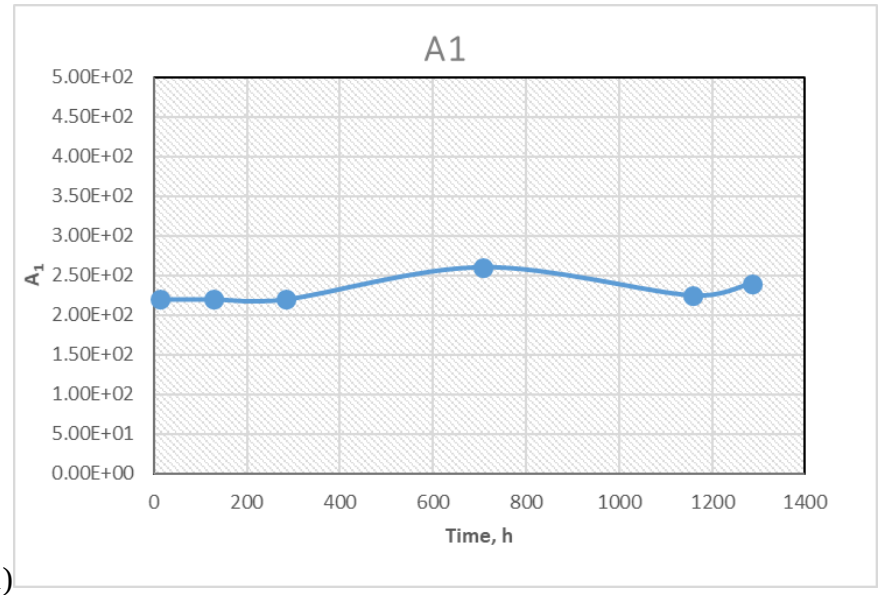

1)

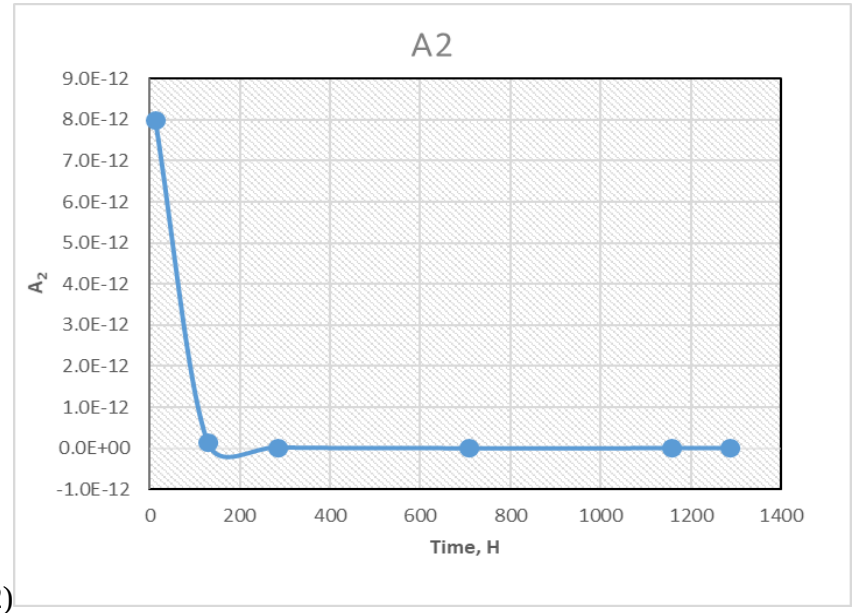

2)

Figure 8.15 The trend of coefficient: 1) A_1; 2) A_2 with time under 320MPa.

From Table 8.12 and Figure 8.15, the model shows that the cavity growth rate is increasing by 9.09% while the nucleation rate is decreasing 99.9% during the lifetime. The parameter of the first point is significantly affected because some original voids have been brought into the sample during the production process. The accuracy of the first point in the calculated parameters can be affected by these original voids. This is one reason for the great change in the first parameter in Figure 8.15. The non-coalesced voids are another reason for changing the coefficient values. The application of the developed cavitation model indicates the characteristics of creep lifetime.

Based on Equation 6.11 with the values of A_1 and A_2, the change of U' over a lifetime is shown in Figure 8.16.

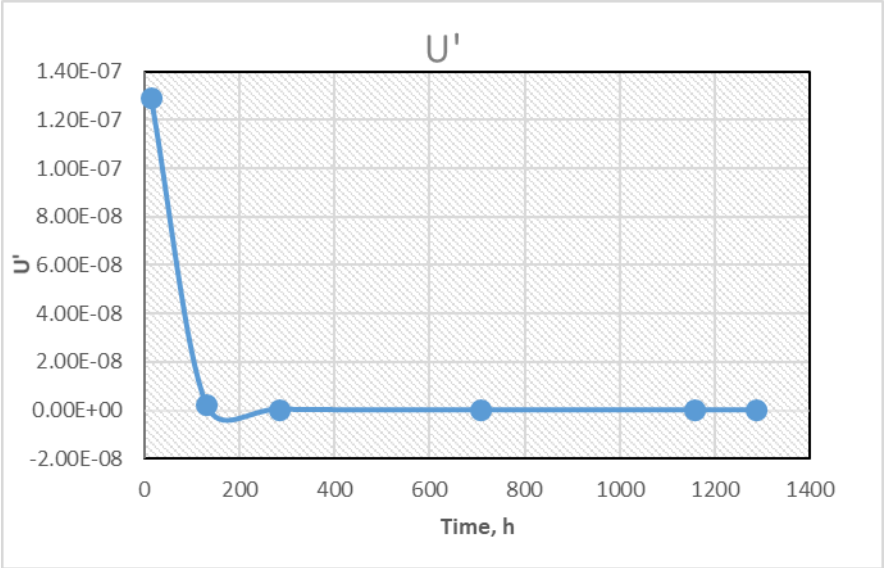

Figure 8.16 The trend of *U'* over lifetime under 320MPa.

The creep cavitation lifetime coefficient *U'* is decreasing 69.06% from 22% lifetime to rupture time in Figure 8.16. The change of *U'* over a lifetime is useful.

8.4 The characteristics of cavitation and creep damage

This section is to investigate the process of *W, J, R* and *R* rate with time at 675°C under 150MPa and 550°C under 320MPa for 316H steel. The research is based on the values of material parameters at rupture time.

8.4.1 The process of *W* with time

According to Equation 6.12 in Chapter 6 and rupture time under 150MPa and 320MPa for 316H steel, the value of *U'* can be calculated. The result produced by *W* and time are shown in Figure 8.17, respectively.

1)

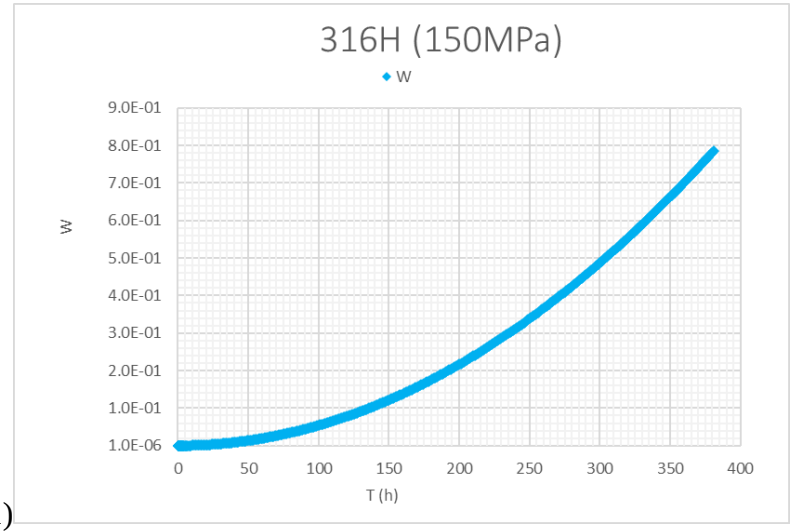

2)

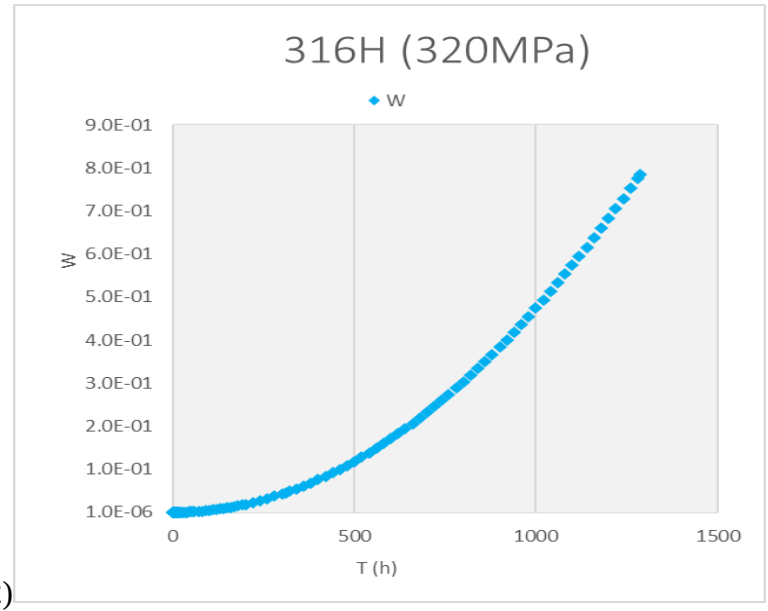

Figure 8.17 The result produced by *W* with time for 316H steel: 1) at 675°C under 150MPa; 2) at 550°C under 320MPa.

Figure 8.17 shows the relationship between *W* and time for 316H steel; the two sets for the value of *W*, increasing with time, will be up to 7.85×10^{-1} at the rupture time. The value of a theory is equal to the $\pi/4$, which is also satisfying the research for coefficient *U'*.

8.4.2 The process of cavity density *J* with time

This part, based on Equation 6.13 in Chapter 6, is combined with the values of A_2 at rupture time. The relationship between cavity density and time can be produced and is shown in Figure 8.18.

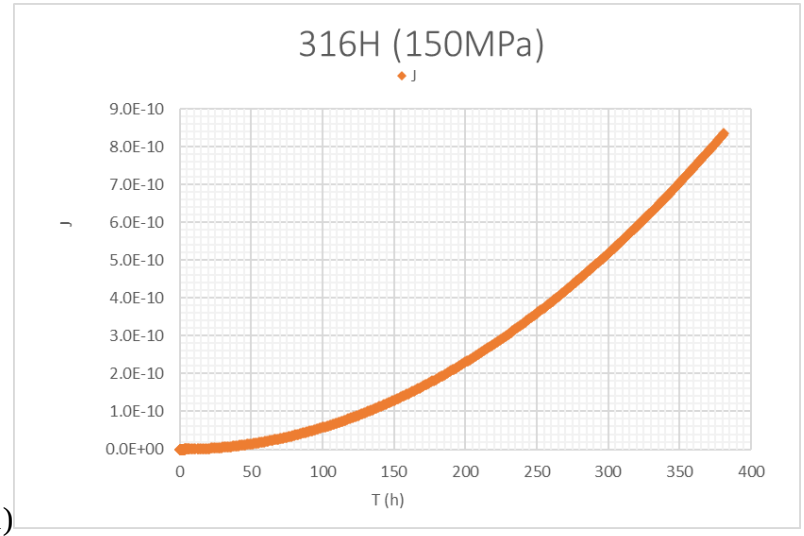

1)

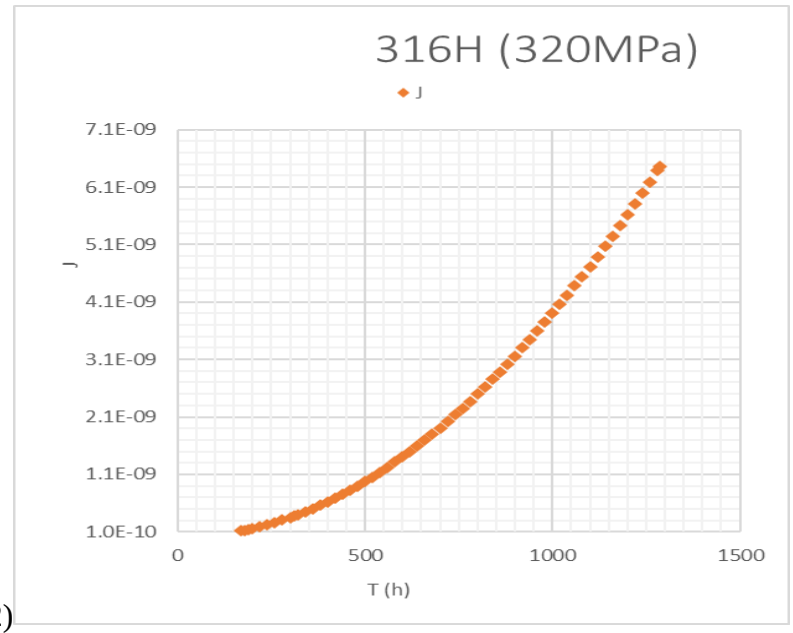

2)

Figure 8.18 The result produced by *J* with time for 316H steel: 1) at 675°C under 150MPa; 2) at 550°C under 320MPa.

Figure 8.18 shows the relationship between *J* and time for 316H steel: 1) displays the value of *J*, increasing with time, this will be up to 8.35×10^{-10} nm^{-3} at the rupture time; 2) indicates the value of *J*, increasing with time, this will be up to 6.46×10^{-9} nm^{-3} at the rupture time. The increasing trend is the same with two sets of data, but the values are different at the end.

8.4.3 The process of radius *R* with time

There are two methods to research the relationship between radius and time, respectively. One method is based on the values of A_1 and C at rupture time utilising Equation 6.6 in Chapter 6. The second route is based on the following equations which

gives:

$$R = R_0 + \Delta t\dot{R} \quad (8.1)$$

$$\dot{R} = A_1 R^{-\beta} t^{-\alpha} \quad (6.2)$$

where R_0 is an initial value, and β=2, α=1.

The relationship between radius R and time can be produced and is shown in the following Figure 8.19.

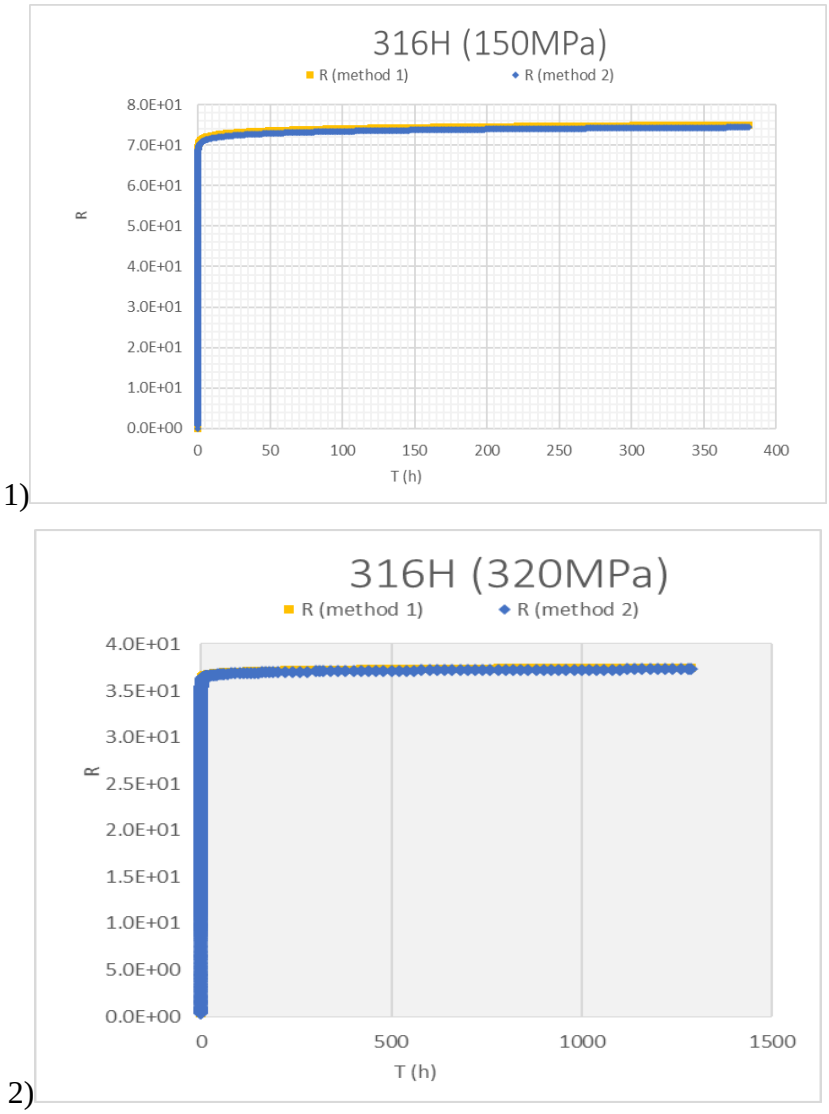

1)

2)

Figure 8.19 The results produced by radius R with time for 316H steel: 1) at 675°C under 150MPa; 2) at 550°C under 320MPa.

Figure 8.19 indicates the relationship between radius R and time for 316H steel, the yellow points are based on the first method and 1) the value of radius is 7.5×10^{1}nm at rupture time, and 2) the value of radius is 3.75×10^{1}nm at rupture time. According to the two methods compared, the blue points are based on the second method and 1) the value

of radius is 7.442×10^{1}nm at rupture time, and 2) the value of the radius is 3.732×10^{1}nm at rupture time. The values produced are approximately equal by both methods, and both trends of the results are similar. The increasing trend is the same for two sets of data, but the values are different at the end.

8.4.4 The process of radius rate $\dot{R}$ with time

According to Equation 6.2 in Chapter 6 and the value of A_1 at rupture time, the relationship between radius rate $\dot{R}$ and time can be produced and is shown in Figure 8.20.

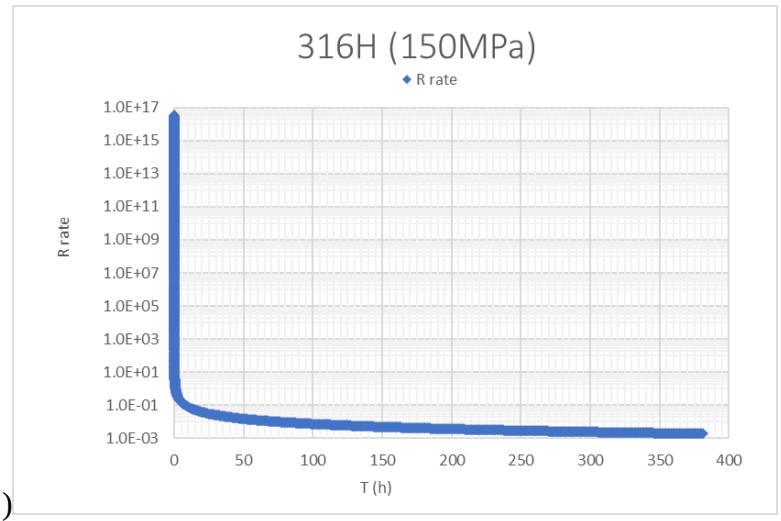

1)

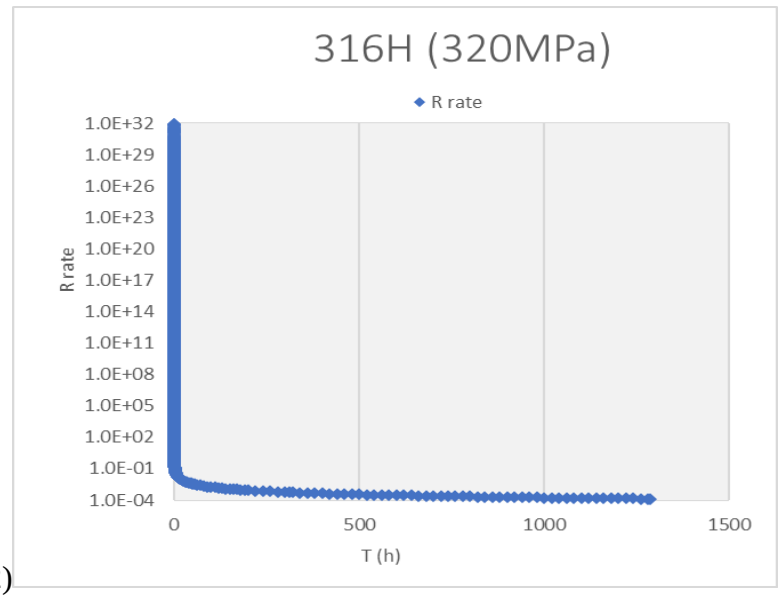

2)

Figure 8.20 The result produced by radius rate with time for 316H steel: 1) at 675°C under 150MPa; 2) at 550°C under 320MPa.

The relationship between radius rate and time for 316H steel is shown in Figure 8.19:

1) the value of radius rate decreases from 3.46×10^{16} nm/h to 1.9×10^{-3}nm/h with time, the radius rate decreases rapidly at the beginning of 22 hours, but radius rate decreases slowly during the remaining time; 2) the value of radius rate decreases from 8.54×10^{31} nm/h to 1.34×10^{-4}nm/h with time. The radius rate decreases rapidly with time at the beginning of 55 hours while the radius rate decreases slowly during the remaining time. The decreasing trend is the same for the two sets of data, but the values are different at the end.

8.5 Summary

This chapter was successful in developing the creep cavitation model and researching the characteristics of creep cavitation damage, which includes the process of *W, J, R* and *R* rate with time. The new development in this chapter was achieved by developing and calibrating a creep cavitation model at different stages of creep lifetime for 316H steel and completed by the further application of the novel creep cavitation equation in Chapter 6. This development confirmed that the creep cavitation damage equation is not only applied at creep rupture time but is also suitable at creep during any time. The experimental data was based on two sets of creep tested under different temperature and stress levels. The model reveals that the nucleation rate is decreasing while the cavity growth rate is increasing slightly during the lifetime. The application of the developed cavitation model shows the characteristics of creep lifetime.

Chapter 9 Conclusions and future work

9.1 Contributions and conclusions

This thesis has successfully developed and applied creep damage constitutive equations over a wide range of stress levels for high Cr steel. This was based on cavity nucleation and cavity growth models, and the creep cavitation fraction along with the grain boundary concept and model. According to the previous chapters, the significant contributions of this research are now summarised in the following section.

Firstly, the most accurate modelling of the minimum creep strain rate and a wide range of stress level at 600°C and 650°C for P92 steel were obtained. This is achieved by the application of the "novel hyperbolic sine law. This work has demonstrated that the typical power law, linear power law and the conventional sine law were inadequate for this task; they need to divide two or three stages to reflect the condition of minimum creep strain rate with different stress levels.

Secondly, a novel creep cavitation damage mechanism based creep rupture time model was developed for E911 steel, where the most accurate and representative cavitation data produced by 3D x-ray microtomography technology were used. The accurate cavitation data and the cavitation process based theoretical framework, as reported above, made this work as the most advanced and accurate (in comparison with other empirical based).

Thirdly, the creep cavitation rupture modelling has been developed based on the NIMS (2018) data sheet at 600°C and 650°C for P92 steel. This includes developing and confirming the "novel hyperbolic sine law" to discuss the relationship between the creep rupture time coefficient U' and a wide range of stress, and from this accurately predict lifetime for components, especially in the low stress and over long time period. The modelling confirmed that the cavitation damage along the grain boundary is not dependent on the creep strain rate; instead, it is dependent on applied stress and the tested temperature. This limitation of the "novel hyperbolic sine law" means it is not suitable in the higher stresses, but it is suitable in the lower stresses.

Finally, the knowledge of the evolution of the cavitation process at 550°C and 675°C for 316H steel were obtained. This achieves further application of the novel creep cavitation equation outlined in Chapter 6 and confirms that the creep cavitation damage equation is not only applied at creep rupture time but is also suitable at any creep time. The limitation of this model is the coefficient values can be changed by some original voids being brought into the sample during the production process and also by non-coalesced voids. The cavitation model has successfully been applied to the calibration and has shown the characteristics of creep lifetime for 316H steel at different stages of creep lifetime.

So far, the thesis has only covered three high Cr steel materials, including P92, E911 and 316H steels.

It is expected that the methodology developed can be applied to any other high temperature multi-grain alloys. They will include the existing low and high Cr steels (Figure 1.5) and the newly developed power plant steels, such as T/P122, 304, AISI321 and AISI347. The potential application is huge.

9.2 Future work

According to the current research findings of the PhD project, the author proposes below several areas that can be improved with further work in the future:

(1) The creep damage constitutive equations could be developed in the multi-axial stress state. The development could be expanded from the version of un-axial to multi-axial stress. In addition, the equations could be applied to finite element analysis software.

(2) The software of optimisation could be developed for the creep cavitation damage equation for high Cr steel, such as P91, E911 and 316H steels. The available central part is to optimise the material parameters and constants in operation.

(3) Suggested use of a series of β values. The optimisation of the creep cavitation damage equation for 316H steel can be completed by hand.

(4) The creep cavitation damage equation could be developed by thinking about the effect of the void coalescence. The development could decrease the error between the prediction curve and its experimental data in a large diameter at rupture.

(5) The creep damage constitute equations could be developed for other low or high Cr steels. This requires more experimental data to be gathered by the 3D x-ray microtomography technology and based on the cavitation damage evolution with creep rupture.

(6) The creep cavitation modelling approach should be generic to use for any other mechanisms of cavitation damage, for example, fatigue fracture and in combination with creep fracture.

(7) The effect of stress state on cavitation should be researched in the future.

References

Abe, F., Kern, T., Viswanathan, R. (2008). Creep-resistant steels. Woodhead publishing in Metals and Surface Engineering.

Ashby, M.F. (1972). Boundary defects and atomistic aspects of boundary sliding and diffusional creep. *Surface Science*, 31, 498-542.

Aghajani, A., Somsen, C.H., Eggeler, G. (2009). On the effect of long-term creep on the microstructure of a 12% chromium tempered martensite ferritic steel. *Acta Materialia*, 57 (17), 5093-5106.

Alang, N.A. (2018). Prediction of long-term static and cyclic creep rupture and crack growth of Grade 92 steels under different stress states. [Doctoral Thesis]. Imperial College of London.

Altenbach, H., Gorash, Y., Naumenko, K. (2008). Steady-state creep of a pressurized thick cylinder in both the linear and the power law ranges. *Acta Mechanica*, 195, 263-274.

An, L.L. (2015). The development of advanced creep constitutive equations for high chromium alloy steel (P91) at transition stress range [Doctoral Thesis]. The University of Huddersfield.

Armaki, H.G., Chen, R., Maruyama, K., Igarashi, M. (2010). Premature creep failure in strength enhanced high Cr ferritic steels caused by static recovery of tempered martensite lath structures. *Materials Science and Engineering A*, 527(24), 6581-6588.

Bailey, R.W. (1930). Creep of steel under simple and compound stress. *Engineering*, 121,129-265.

Basirat, M., Shrestha, T., Potirniche, G.P., Charit, I., Rink, K. (2012). *International Journal of Plasticity*, 37, 95-107.

Cane, B.J. (1979). Interrelationship between creep deformation and creep rupture in 2.25Cr1Mo steel. *Metal Science*, 13 (5), 287-294.

Chen, Y.X., Yan, W., Hu, P., Shan, Y.Y., Yang, K. (2011). CDM modeling of creep behavior of T/P91 steel under high stresses. *Acta Metallurgica Sinica*, 47 (11), 1372-1377.

Chalk, K. (2013). Weld consumables and PWHT for P92 power plant steel [Doctoral Thesis]. The University of Nottingham.

Cole, D.G. (2000). Design of heat-resistant streels for small power plant [Doctoral Thesis]. The University of Cambridge.

Czyrska, F.A., Zielińska, L.A., Ennis, P.J. (2006). Modified 9% Cr steels for advanced power generation: microstructure and properties. *Journal of Achievements in Materials and Manufacturing Engineering*, 19 (2), 43-48.

Dyson, B.F. Mclean, M. (2001). Micromechanism-quantification for creep constitutive equations. In S. Murakami, N. Ohno (Eds.) *IUTAM Symposium on Creep in Structures (1st Ed)*, 3-16.

Dyson, B. (2000). Use of CDM in materials modelling and component creep life prediction. *Journal of Pressure Vessel Technology*, 122, 281-296.

Dyson, B., McLean, M. (1997). Microstructural evolution and its effects on the creep performance of high temperature alloys. In: Strang A, Cawley J, Greenwood GW, editors. Microstructural stability of creep resistant alloys for high temperature plant applications. *IOM Communications*, London, 371–393.

Dyson, B. F. (1988). Creep and fracture of metals: mechanisms and mechanics. *Revue de Physique Appliquee*, 23(4), 605-613.

Dyson, B.F. Gibbons, T.B. (1987). Tertiary creep in nickel-base superalloys: analysis of experimental data and theoretical synthesis. *Acta Metallurgica*, 35 (9), 2355-2369.

Dyson, B.F. (1983). Continuous cavity nucleation and creep rupture. *Scripta Metallurgica*, 17, 31-37.

Eggeler, G., Earthman, J., Nilsvang, N., Ilschner, B. (1989). Microstructural study of creep rupture in a 12% chromium ferritic steel. *Acta Metallurgica*, 37(1), 49-60.

Elarbi, Y.M. (2008). Weldability of high Cr and 1 % tungsten alloyed creep resistant martensitic steel [Doctoral Thesis]. Budapest University of Technology and Economics.

Ennis, P.J., Czyrska, F.A. (2003). Recent advances in creep-resistant steels for power plant applications. *Sadhana*, 28(3 & 4), 709–730.

Ennis, P.J., Zielinska, L.A., Wachter, O., Czyrska, F.A. (1997). Microstructural stability and creep rupture strength of the martensitic steel P92 for advanced power plant. *Acta Mater*, 45(12), 4901-4907.

Evans, H. (1984). Mechanisms of creep fracture. *Elsevier Applied Science Publishers Ltd*, 319.

Evans, R.W., Wilshire, B. (1985). Creep of Metals and Alloys.

Fedoseeva, A., Dudova, N., Kaibyshev, R. (2016). Creep strength breakdown and microstructure evolution in a 3% Co modified P92 steel. *Materials Science & Engineering A*, 654, 1-12.

Gaffard, V., Besson, J., Gourgues, L.A.F. (2008). Modelling high temperature creep flow, damage and fracture behaviour of 9Cr1MoNbV steel weldments. *Materials at High Temperatures*, 25(3), 159-167.

Ghauri, P. N., Grønhaug, K. (2005). Research methods in business studies: A practical guide: Pearson Education.

Ghosh, R.N. (2013). Creep life predictions of engineering components: problems and prospects. *Procedia Engineering*, 55, 599-606.

Global Energy Statistical. (Yearbook 2020). Enerdata. Retrieved from https://yearbook.enerdata.net/total-energy/world-consumption-statistics.html.

Gorash, Y. (2008). Development of a creep-damage model for non-isothermal long-term strength analysis of high-temperature components operating in a wide stress range [Doctoral Thesis]. Martin-Luther-University Halle-Wittenberg, Halle (Saale), Germany.

Gupta, C., Toda, H., Mayr, P., Sommitsch, C. (2015). 3D creep cavitation characteristics and residual life assessment in high temperature steels: a critical review. *Materials Science and Technology*, 3 (5), 603-626.

Gupta, C., Toda, H., Schlacher, C., Adachi, Y., Mayr, P., Sommitsch, C., Kobayashi, M. (2013). Study of creep cavitation behavior in tempered martensitic steel using synchrotron micro-tomography and serial sectioning techniques. *Materials Science & Engineering A*, 564, 525-538.

Hayhurst, R.J., Vakili, T.F., Hayhurst, D.R. (2009). Verification of 3-D parallel CDM software for the analysis of creep failure in the HAZ region of Cr–Mo–V crosswelds. *International Journal of Pressure Vessels and Piping*, 86(8),475-485.

Hayhurst, D.R., Lin, J., Hayhurst, R.J. (2008). Failure in notched tension bars due to high-temperature creep: Interaction between nucleation controlled cavity growth and continuum cavity growth. *International Journal of Solids and Structures*, 45, 2233-2250.

Hayhurst, D.R., Hayhurst, R.J., Vakili, T.F. (2005a). Continuum damage mechanics

predictions of creep damage initiation and growth in ferritic steel weldments in a medium bore branched pipe under constant pressure at 590 °C using a five-material weld model. *Proceedings of the Royal Society A*, Mathematical, Physical, and Engineering Sciences, 461 (2060), 2303-2326.

Hayhurst, R. J., Mustata, R., Hayhurst, D. R. (2005b). Creep constitutive equations for parent, Type IV, R-HAZ, CG-HAZ and weld material in the range 565–640°C for Cr–Mo–V weldments. *International Journal of Pressure Vessels and Piping*, 82(2), 137-144.

Hayhurst, D.R., Dimmer, P.R., Morrison, C.J. (1984). Development of continuum damage in the creep rupture of notched bars. *Philosophical Transactions of the Royal Society A*, 311 (1516), 103-129.

Han, H.G., Shen, J.J., Xie, J.X. (2018). Effects of precipitates evolution on low stress creep properties in P92 heat-resistant steel. *Scientific Reports*, 8(1), 1-10.

Holmströma, S., Lib, Y., Dymacekc, P., Vacchierid, E., Jeffse, S.P., Lancastere, R.J., Omachtf, D., Kubonf, Z., Anellig, E., Rantalah, J., Tontii, A., Komazakij, S., Naveenaj, Bruchhausena, M., Hurste, R.C., Hähnera, P., Richardsonk, M., Andresl, D. (2018). Creep strength and minimum strain rate estimation from Small Punch creep tests. *Materials Science & Engineering A*, 713, 161-172.

Huang, Y.H., Xuan, F.Z. (2016). Creep behavior of P92 steel in the steam environment at 600 °C using miniature three-point bend test. *Materials Engineering and Performance*, 25(12), 5440-5449.

Hyde, T.H., Saber, M., Sun, W. (2010a). Testing and modelling of creep crack growth in compact tension specimens from a P91 weld at 650°C. *Engineering Fracture Mechanics*, 77(15), 2946-2957.

Hyde, T.H., Saber, M., Sun, W. (2010b). Creep crack growth data and prediction for a P91 weld at 650°C. *International Journal of Pressure Vessels and Piping*, 87(12), 721-729.

Hyde, T.H., Sun, W. (2006). Creep failure behaviour of a circumferential P91 pipe weldment with an anisotropic weld metal subjected to internal pressure and end load. *Proceedings of the Institution of Mechanical Engineers, Part L: Journal of Materials Design and Applications*, 220(3), 147-162.

Hyde, T.H., Sun, W., Becker, A.A., Williams, J.A. (2004). Creep properties and failure assessment of new and fully repaired P91 pipe welds at 923 K. *Proceedings of the Institution of Mechanical Engineers, Part L: Journal of Materials Design and Applications*, 218(3), 211-222.

Jazaeri, H., Bouchard, P.J., Hutchings, M.T., Spindler, M.W., Mamum, A.A., Heenan, R.K. (2019). An investigation into creep cavity development in 316H stainless steel. *Metals*, 9, 318.

Kalck, C., Fournier, B., Barcelo, F., Forest, L., Dalle, F., Giroux, P.F., Gourgues, L.A.F. (2010). High temperature creep properties and microstructural examinations of P92 welds. *Materials for Advanced Power Engineering*, 424-434.

Kassner, M.E., Hayes, T.A. (2003). Creep cavitation in metals. *International Journal of Plasticity*, 19(10), 1715–1748.

Kassner, M.E. (2015). Fundamentals of creep in metals and alloys. *Elsevier Ltd*.

Khayatzadeh, S., Tanner, D.W.J., Truman, C.E., Flewitt, P.E.J., Smith, D.J. (2017a). Creep deformation and stress relaxation of a martensitic P92 steel at 650°C. *Engineering Fracture Mechanics*, 175, 57-71.

Khayatzadeh, S., Tanner, D.W.J., Truman, C.E., Flewitt, P.E.J., Smith, D.J. (2017b). Influence of thermal ageing on the creep behaviour of a P92 martensitic steel. *Materials Science & Engineering A*, 708, 544-555.

Kim, W.G., Kim, S.H., Lee, C.B. (2011). Long-term creep characterization of Gr. 91 steel by modified creep constitutive equations. *Metals and Materials International*, 17(3), 497-504.

Kim, S.C., Shim, J.H., Jung, W.S., Choi, Y.S. (2019). Short-term creep data based long-term creep life predictability for Grade 92 steels and its microstructural basis. *Metals and Materials International,* 25(3), 713–722.

Kimura, K., Toda, Y., Kushima, H., Sawada, K. (2010a). Creep strength of high chromium steel with ferrite matrix. *International Journal of Pressure Vessels and Piping*, 87, 282-288.

Kimura, K., Sawada, K., Kushima, H. (2010b). Long-term creep strength property of advanced ferritic creep resistant steels. Advances in Materials Technology for Fossil Power Plants, Proceedings from the Sixth International Conference August 31–September 3, 2010, Santa Fe, New Mexico, USA.

Kobayashia, M., Kawamuraa, Y., Uenoa, S., Todab, H., Miura, H. (2014). Measurement of local plastic deformation in aluminum alloy by means of X-ray 3D imaging technique. *Procedia Engineering*, 81, 1408–1413.

Kral, P., Dvorak, J., Sklenicka, V., Masuda, T., Horita, Z.J., Kucharova, K., Kvapilova,

M., Svobodova, M. (2018). The effect of ultrafine-grained microstructure on creep behaviour of 9% Cr steel. *Materials*, 11(787).

Kvapilova, M., Dvorak, J., Kral, P., Svoboda, M. (2013). Application of the Monkman-Grant relationship for Ultrafine-Grained metallic materials. *Key Engineering Materials*, 577-578, 137-140.

Landes, J.D., Schwalbe, K.H. (2004). An analysis of creep deformation parameters. Part 1: Background. *Engineering Fracture Mechanics*, 71, 2449-2461.

Larson, F.R., Miller, J. (1952). A time-temperature relationship for rupture and creep stresses, *Transactions of ASME*, 74, 765-771.

Lee, J.S., Armaki, H.G., Maruyama, K., Muraki, T., Asahi, H. (2006). Causes of breakdown of creep strength in 9Cr–1.8W–0.5Mo–VNb steel. *Materials Science and Engineering A*, 428, 270–275.

Lin, J., Liu, Y., Dean, T.A. (2005). A review on damage mechanisms, models and calibration methods under various deformation conditions. *International Journal of Damage Mechanics*, 14 (4), 299-319.

Maruyama, K., Sawada, K., Koike, J.I. (2001). Strengthening mechanisms of creep resistant tempered martensitic steel. *ISIJ International*, 41(6), 641–653.

Masuyama, F. (2001). Review: History of power plants and progress in heat resistant steels. *ISIJ International*, 41(6), 612-625.

Masuyama, F. (2007). Creep rupture life and design factors for high-strength ferritic steels. *International Journal of Pressure Vessels and Piping*, 84, 53–61.

Masuyama, F. (2010). Effect of specimen size and shape on creep rupture behavior of creep strength enhanced ferritic steel welds. *International Journal of Pressure Vessels and Piping*, 87, 617-623.

Masuyama, F. (2013a). Advances in creep damage/life assessment technology for creep strength enhanced ferritic steels. *Procedia Engineering*, 55, 591-598.

Masuyama, F., Shingledecker, J.P. (2013b). Recent status of ASME code on creep strength enhanced ferritic steels. *Procedia Engineering*, 55, 314-325.

Main, I.G. (2000). A damage mechanics model for power-law creep and earthquake aftershock and foreshock sequences. *Geophysical Journal International*, 142(1), 151–161.

Meng, Q.H., Wang, Z.Q. (2019). Creep damage models and their applications for crack growth analysis in pipes: A review. *Engineering Fracture Mechanics*, 205, 547-576.

Monkman, F.C., Grant, N.J. (1956). An empirical relationship between rupture life and minimum creep rate in creep-rupture tests. *ASTM International*, 56, 593–620.

Nagode, A., Kosec, L., Ule, B., Kosec, G. (2011). Review of creep resistant alloys for power plant applications. *METALURGIJA*, 50(1), 45-48.

National Institute for Materials Science (NIMS), Japan. (2014). Data Sheets on the Elevated-temperature Properties of 9Cr-1Mo-V-Nb Steel Tubes for Boilers and Heat Exchangers (ASME SA-213/SA-213M Grade T91), 9Cr-1Mo-V-Nb Steel Plates for Boilers and Pressure Vessels (ASME SA-387/SA-387M Grade 91) and 9Cr-1Mo-V-Nb Steel Seamless Pipe for High Temperature Service (ASME SA-335/SA-335M Grade P91). No.43A.

National Institute for Materials Science (NIMS), Japan. (2018). Date Sheet on the Elevated-temperature Properties of 9Cr-0.5Mo-1.8W-V-Nb Steel Tubes for Power Boilers (ASME SA-213/SA-213M Grade T92) and 9Cr-0.5Mo-1.8W-V-Nb Steel Pipe for High Temperature Service (ASME SA-335/SA-335M Grade P92). No.48B.

Naumenko, K., Altenbach, H. (2007). Modelling of creep for structural analysis. Berlin.

Naumenko, K., Altenbach, H., Gorash, Y. (2009a). Creep analysis with a stress range dependent constitutive model. *Arch Appl Mech*, 79, 619–630.

Naumenko, K., Kostenko, Y. (2009b). Structural analysis of a power plant component using a stress-range-dependent creep-damage constitutive model. *Materials Science and Engineering A*, 510-511, 169-174.

Nurbanasari, M., Suratman, R. (2015). Creep damage assessment of a 50 MW steam turbine shaft. MATEC Web of Conferences, 34.

Nikbin, K.M. (2009). Predicting creep and creep/fatigue crack initiation and growth for virtual testing and life assessment of components, *Virtual Testing and Predictive Modeling.*

Norton, F.H. (1929). The creep of steel at high temperatures. McGraw-Hill book, New York.

Panait, C.G. (2010a). Metallurgical evolution and creep strength of 9–12% Cr heat resistant steels at 600°C and 650°C [Doctoral Thesis]. Paris Tech Institut Des Sciences Et Technologies Paris Institute of Technology.

Panait, C.G., Bendick, W., Fuchsmann, A., Gourgues-Lorenzon, A.F., Besson, J. (2010b). Study of the microstructure of the Grade 91 steel after more than 100,000 h of creep exposure at 600℃. *International Journal of Pressure Vessels and Piping*, 87(6), 326-335.

Panait, C.G., Zielińska, L.A., Koziel, T., Czyrska, F.A., Gourgues, L.A.F., Bendick, W. (2010c). Evolution of dislocation density, size of subgrains and MX-type precipitates in a P91 steel during creep and during thermal ageing at 600℃ for more than 100,000h. *Materials Science and Engineering A*, 527(16-17), 4062-4069.

Parker, J. (2013). In-service behavior of creep strength enhanced ferritic steels Grade 91 and Grade 92 – Part 1 parent metal. *International Journal of Pressure Vessels and Piping*, 101, 30-36.

Perrin, I.J., Fishburn, J.D. (2008). A perspective on the design of high-temperature boiler components. *International Journal of Pressure Vessels and Piping*, 85(1), 14–21.

Perrin, I.J., Hayhurst, D.R. (1996a). A method for the transformation of creep constitutive equations. *International Journal of Pressure Vessels and Piping*, 68(3), 299-309.

Perrin, I., Hayhurst, D. (1996b). Creep constitutive equations for a 0.5 Cr–0.5 Mo–0.25 V ferritic steel in the temperature range 600–675℃. *The Journal of Strain Analysis for Engineering Design*, 31(4), 299-314.

Petry, C., Lindet, G. (2009). Modelling creep behaviour and failure of 9Cr–0.5Mo–1.8W–VNb steel. *International Journal of Pressure Vessels and Piping*, 86(8), 486-494.

Prager, M. (1995). Development of the MPC project omega method for life assessment in the creep range. *Journal of Pressure Vessel Technology*, 117(2), 95-103.

Raj, R., Ashby, M.F. (1975). Intergranular fracture at elevated temperature. *Acta Metallurgica*, 23(6), 653-666.

Renversade, L., Ruoff, H., Maile, K., Sket, F., Borbely, A. (2014). Microtomographic assessment of damage in P91 and E911 steels after long-term creep. *International Journal of Materials Research*, 105 (7), 621-627.

Riedel, H. (1987). Fracture at High Temperatures (1st Ed.). Berlin.

Rouse, J.P., Sun, W., Hyde, T.H., Morris, A. (2013). Comparative assessment of several creep damage models for use in life prediction. *International Journal of Pressure Vessels and Piping*, 108-109, 81-87.

Rubin, E.S., Chen, C., Rao, A.B. (2007). Cost and performance of fossil fuel power plants with CO_2 capture and storage. *Energy Policy*, 35, 4444–4454.

Saad, A.A., Hyde, T.H., Sun, W., Hyde, C.J., Tanner, D.W.J. (2013). Characterization of viscoplasticity behaviour of P91 and P92 power plant steels. *International Journal of Pressure Vessels and Piping*, 111-112, 246-252.

Saber, M., Tanner, D.W.J., Sun, W., Hyde, T.H. (2011a). Determination of creep and damage properties for P92 at 675 °C. *Strain Analysis for Engineering Design*, 46, 842-851.

Saber, M. (2011b). Experimental and finite element studies of creep and creep crack growth in P91 and P92 weldments [Doctoral Thesis]. The University of Nottingham.

Sawada, K., Kushima, H., Tabuchi, M., Kimura, K. (2011). Microstructural degradation of Gr.91 steel during creep under low stress. *Materials Science and Engineering A*, 528(16-17), 5511-5518.

Sawada, K., Bauer, M., Kauffmann, F., Mayr, P., Klenk, A. (2010). Microstructural change of 9% Cr-welded joints after long-term creep. *Materials Science and Engineering A*, 527(6), 1417-1426.

Sawada, K., Kubo, K., Abe, F. (2001). Creep behavior and stability of MX precipitates at high temperature in 9Cr–0.5Mo–1.8W–VNb steel. *Materials Science and Engineering A*, 319–321, 784–787.

Sakthivel, T., Panneer Selvi, S., Laha, K. (2015). An assessment of creep deformation and rupture behaviour of 9Cr–1.8W–0.5Mo–VNb (ASME grade 92) steel. *Materials Science & Engineering A*, 640, 61–71.

Samuel, E.I., Choudhary, B.K., Palapariti, D.P.R., Mathew, M.D. (2013). Creep deformation and rupture behaviour of P92 steel at 923K. *Procedia Engineering*, 55, 64-69.

Schlacher, C., Pelzmann, T., Beal, C., Sommitsch, C., Gupta, C., Toda, H., Mayr, P. (2015). Investigation of creep damage in advanced martensitic chromium steel weldments using synchrotron X-ray micro-tomography and EBSD. *Materials Science and Technology*, 31 (5), 516–521.

Schlacher, C., Sommitsch, C., Mayr, P., Gupta, C., Toda, H., Usegi, K., Suzuki, Y. (2012). Creep and damage investigation of improved 9%Cr steel welded joints. Proceedings of the 9th International Conference: Trends in Welding Research, June 4–8, 2012, Chicago, Illinois, USA.

Seo, D., Toda, H., Kobayashi, M., Uesugi, K., Takeuchi, A., Suzuki, Y. (2015) In situ observation of void nucleation and growth in a steel using X-ray tomography. *ISIJ International*, 55 (7), 1474–1482.

Sheridan, N. (Producer). (2010, 25/03). Writing a methodology chapter.

Shinya, N., Kyono, J., Kushima, H. (2006). Creep fracture mechanism map and creep damage of Cr–Mo–V turbine rotor steel. *ISIJ International*, 46(10), 1516–1522.

Sket, F., Dzieciol, K., Borbely, A., Kaysser-Pyzalla, A.R., Maile, K., Scheck, R. (2010). Microtomographic investigation of damage in E911 steel after long term creep. *Materials Science and Engineering A*, 528 (1), 103-111.

Sklenicka, V., Kucharova, K., Kvapilova, M., Kloc, L., Dvorak, J., Kral, P. (2018). Interrelationship between creep deformation and damage for advanced creep-resistant steels. *Engineering Materials*, 774, 119-124.

Sklenicka, V., Kucharova, K., Kral, P., Kvapilova, M., Svoboda, M., Cmakal, J. (2015). The effect of hot bending and thermal ageing on creep and microstructure evolution in thick-walled P92 steel pipe. *Materials Science & Engineering A*, 644, 297-309.

Sklenicka, V., Kucharova, K., Svoboda, M., Kroupa, A. (2010). Creep behaviour of advanced power plant steels after long-term isothermal ageing. Advances in Materials Technology for Fossil Power Plants, Proceedings from the Sixth International Conference, August 31–September 3, Santa Fe, New Mexico, USA.

Sklenicka, V. (2003). Long-term creep behavior of 9–12%Cr power plant steels. *Materials Characterization*, 51(1), 35-48.

Stracey, M.G., Continuum Damage Mechanics (CDM) modelling of dislocation creep in 9-12% Cr creep resistant steels [Master Thesis]. The University of Cape Town.

Stock, S.R. (2013). Recent advances in X-ray microtomography applied to materials. *International Materials Reviews*, 53(3), 129-181.

Sundararajan, G. (1989). The Monkman-Grant relationship. *Materials Science & Engineering*, 112, 205-214.

Tabuchi, M., Yokobori, J.A.T., Sugiura, R., Yatomi, M., Fu, J.A., Kobayashi, K. (2010), Results of a Japanese round robin program for creep crack growth using Gr.92 steel welds. *Engineering Fracture Mechanics*, 77, 3066–3076.

Toda, H., Shamsudin, Z.A.B., Shimizu, K., Uesugi, K., Takeuchi, A., Suzuki, Y.,

Nakazawa, M., Aoki, Y., Kobayashi, M. (2013). Cavitation during high-temperature deformation in Al-Mg alloys. *Acta Materials*, 61, 2403-2413.

Vangkilde, P.T., Anthonsen, K., Smith, N., Kirk, K., Neele, F., Meer, V.B., Le, G.Y., Bossie, C.D., Wojcicki, A., Le, N.Y.M., Hendriks, C., Dalhoff, F., & Christensen, N. P. (2009). Assessing of European capacity for geological storage of carbon dioxide-the EU GeoCapacity project. *Energy Procedia*, 1, 2663–2670.

Vivier, F., Gourgues-Lorenzon, A.F., Besson, J. (2010). Creep rupture of a 9Cr1MoNbV steel at 500°C: Base metal and welded joint. *Nuclear Engineering and Design*, 240(10), 2704-2709.

World Energy Balances. (July 2020). IEA. Retrieved from https://www.iea.org/reports/world-energy-balances-overview.

Wu, R., Sandström, R. (1995). Creep cavity nucleation and growth in 12Cr–Mo–V steel. *Materials Science and Technology*, 11(6), 579-588.

Xu, X., Siefert, J.A., Parker, J.D., Thomson, R.C. (2020). Localised creep cavitation on boron nitride in the heat affected zone of 9%Cr tempered martensitic steel welds. *Materials and Design*, 196, 109046.

Xu, Q., Yang, X., Lu, Z.Y. (2017a). On the development of creep damage constitutive equations: modified hyperbolic sine law for minimum creep strain rate and stress and creep fracture criterion based on cavity area fraction along grain boundaries. *Materials at High Temperatures*, 34 (5-6), 323–332.

Xu, Q., Lu, Z.Y., Wang, X. (2017b). Damage modelling: the current state and the latest progress on the development of creep damage constitutive equations for high Cr steels. *Materials at High Temperatures*, 34 (3), 229-237.

Xu, Q. (2004). The development of validation methodology of multi-axial creep damage constitutive equations and its application to 0.5Cr0.5Mo0.25V ferritic steel at 590 °C. *Nuclear Engineering and Design*, 228 (1-3), 97-106.

Xu, Q. Barrans, S. (2003). The development of multi-axial creep damage constitutive equations for 0.5Cr0.5Mo0.25V ferritic steel at 590°C. *International Journal Series A Solid Mechanics and Material Engineering*, 46 (1), 51-59.

Xu, Q. (2001). Creep damage constitutive equations for multi-axial states of stress for 0.5Cr0.5Mo0.25V ferritic steel at 590°C. *Theoretical and Applied Fracture Mechanics*, 36 (2), 99-107.

Xu, Q., Wang, X. (2013). Critical review the development of creep damage constitutive

equations for high Cr steels. 9th New High Temperature Materials Seminar, 23-24 May 2013, London.

Xu, Q., Lu, Z.Y. (2018a). Modelling of creep deformation and creep rupture criterion. 3-day International Conference on Power Plant Operation & Flexibility, Institute of Materials (IOM3), July 4–6, 2018, London.

Xu, Q., Zheng, X.M., Okpa, M., Lu, Z.Y., and Vishnyakov, V. (2018b). Poster, The development of creep damage constitution equations for high Cr alloys. 3-day International Conference on Power Plant Operation & Flexibility, Institute of Materials (IOM3), July 4–6, 2018, London.

Xu, Q., Lu, Z.Y. (2019). Chapter: Modeling of creep deformation and creep fracture. *Strength of Materials*, IntechOpen.

Xu, Q.H. (2016) Development of advanced creep damage constitutive equations for low CR alloy under long-term service [Doctoral Thesis]. The University of Huddersfield.

Yadav, S.D., Sonderegger, B., Stracey, M., Poletti, C. (2016). Modelling the creep behaviour of tempered martensitic steel based on a hybrid approach. *Materials Science & Engineering A*, 662, 330-341.

Yamasaki, S., Mitsuhara, M., Nakashima, H. (2018). Development of high-chromium ferritic heat-resistant steels with high nitrogen content. *ISIJ International*, 58(6), 1146–1154.

Yang, X. (2018). The development of creep damage constitutive equations for high chromium steel based on the mechanism of cavitation damage [Doctoral Thesis]. The University of Huddersfield.

Yang, X., Xu, Q., Lu, Z.Y. (2013a) The development and validation of the creep damage constitutive equations for P91 alloy. In: Proceedings of the 2013 World Congress in Computer Science and Computer Engineering and Application. 121-127.

Yao, H.P., Zhao, Y.R., Song, X.L., Jia, J., Xiang, Z.D. (2019). On the applicability of boundary condition based tensile creep model in predicting long-term creep strengths and lifetimes of engineering alloys. *European Journal of Mechanics / A Solids*, 73, 57–66.

Yin, Y.F. Faulkner, R.G. (2006). Continuum damage mechanics modelling based on simulations of microstructural evolution kinetics. *Materials Science and Technology*, 22 (8), 929-936.

Yin, Y., Faulkner, R. G., Morris, P., and Clarke, P. (2008). Modelling and experimental studies of alternative heat treatments in Steel 92 to optimize long term stress rupture properties. *Energy Materials*, 3(4), 232-242.

Zhao, P., Xuan, F.Z. (2012). Ratchetting behavior of advanced 9–12% chromium ferrite steel under creep-fatigue loadings: Fracture modes and dislocation patterns. *Materials Science and Engineering A*, 539, 301-307.

Zhao, P., Xuan, F.Z. (2011a). Ratchetting behavior of advanced 9–12% chromium ferrite steel under creep-fatigue loadings. *Mechanics of Materials*, 43, 299-312.

Zhao, P., Xuan, F.Z. (2011b). Ratchetting behavior of advanced 9–12% chromium ferrite steel under creep-fatigue loadings: Fracture modes and dislocation patterns. *Materials Science and Engineering A*, 539, 301–307.

Zheng, X.M., Xu, Q., Lu, Z.Y., Wang, X. Feng, X.Q. (2020). The development of creep damage constitutive equations for high Cr steel. *Materials at High Temperatures*, 37(2), 129-138.

Zhou, Y. (2011). Study on creep behavoir of semi-solid A356 alloy produced by the GISS process [Master Thesis]. Prince of Songkla University.

Zrnik, J., Strunz, P., Vrchovinsky, V., Muransky, O., Novy, Z., Wiedenmann, A. (2004). Degradation of creep properties in a long-term thermally exposed nickel base superalloy. *Materials Science and Engineering A*, 387-389, 728-733.

Appendix A - Tables of selecting creep experimental data

Table 1 Experimental data of minimum creep strain rate under different stresses at 600℃ for P91 (9Cr–1Mo–V–Nb) steel (NIMS, 2014).

Temperature (°C)	Stress (MPa)	Minimum creep rate (1/h)
600	70	9.6×10^{-8}
	80	1.3×10^{-7}
	100	4×10^{-7}
	110	8.1×10^{-7}
	120	1.5×10^{-6}
	140	7.7×10^{-6}
	160	4.2×10^{-5}
	200	1.4×10^{-3}

Table 2 Experimental data of minimum creep strain rate under different stresses at 600℃ for P92 (9Cr–1.8W–0.5Mo–V-Nb) steel (NIMS, 2018).

Temperature (°C)	Stress (MPa)	Minimum creep rate (1/h)
600	120	1.81×10^{-5}
	130	2.57×10^{-5}
	140	6.12×10^{-5}
	160	2.25×10^{-4}
	180	1.81×10^{-3}
	190	6.54×10^{-3}
	210	4.4×10^{-2}
	230	2.67×10^{-1}
	250	9.96×10^{-1}

Table 3 Experimental data of minimum creep strain rate under different stresses at 650℃ for P92 (9Cr–1.8W–0.5Mo–V-Nb) steel (NIMS, 2018).

Temperature (°C)	Stress (MPa)	Minimum creep rate (1/h)
650	50	1.5×10^{-5}
	60	2.93×10^{-5}
	70	6×10^{-5}
	80	1.32×10^{-4}
	90	3.17×10^{-4}
	100	7.73×10^{-4}
	110	2.01×10^{-3}
	130	2.33×10^{-2}
	140	8×10^{-2}
	160	5.6×10^{-1}

Table 4 Experimental data of rupture time under different stress at 600℃ for P91 steel (NIMS, 2014).

Temperature (°C)	Stress (MPa)	Rupture time (h)
600	70	80736.8
	100	34141
	110	21206.3
	120	12858.6
	140	3414.7
	160	971.2

Table 5 Experimental data of rupture time under different stress at 625℃ for P91 steel (NIMS, 2014).

Temperature (°C)	Stress (MPa)	Rupture time (h)
625	90	21372.4
	100	9895.4
	120	1657.9
	140	399

Table 6 Experimental data of rupture time under different stress at 600℃ for P92 steel (NIMS, 2018).

Temperature (°C)	Stress (MPa)	Rupture time (h)
600	120	65363.4
	130	39539.9
	140	25944.6
	160	8219.9
	180	1740.7
	190	613.4
	210	112.6
	230	19.9
	250	5.1

Table 7 Experimental data of rupture time under different stress at 625℃ for P92 steel (NIMS, 2018).

Temperature (°C)	Stress (MPa)	Rupture time (h)
625	100	33518.5
	110	17530
	130	3886.1
	140	1458.2
	160	213.4

Table 8 Experimental data of rupture time under different stress at 650℃ for P92 steel (NIMS, 2018).

Temperature (°C)	Stress (MPa)	Rupture time (h)
650	60	92845.2
	70	50871.2
	80	21717.1
	90	10001.9
	100	3738.7
	110	1689.1
	130	194
	140	66
	160	10.5

Table 9 Creep specimens tested at 600°C for P92 steel (Panait, 2010a).

Temperature (°C)	Stress (MPa)	Minimum creep rate (1/h)
600	120	3.7×10^{-7}
	140	8.37×10^{-7}
	160	2.05×10^{-6}
	180	1.22×10^{-5}

Table 10 Creep specimens tested at 650°C for P92 steel (Panait, 2010a).

Temperature (°C)	Stress (MPa)	Minimum creep rate (1/h)
650	70	7.9×10^{-7}
	90	3.97×10^{-6}
	110	1.28×10^{-5}
	140	1.44×10^{-4}